Effects of Clinically Relevant Superparamagnetic Iron Oxide Nanoparticles on Murine Primary Brain Cells

Dissertation to obtain the academic degree
Doctor rerum naturalium (Dr. rer. nat.)

submitted to the Department of Biology, Chemistry and Pharmacy
of the Freie Universität Berlin

by

Jenni Neubert

Berlin, 2018

The present thesis was conducted at the Institute for Cell Biology and Neurobiology, Center for Anatomy, Charité-Universitätsmedizin Berlin.

1st reviewer: Dr. med. Jana Glumm

2nd reviewer: Prof. Dr. Ursula Koch

Date of Disputation: 20.11.2018

Table of Contents

List of Figures

List of Tables

List of Acronyms

ANOVA	Analysis of variance
ATP	Adenosine triphosphate
BBB	Blood-brain barrier
BDNF	Brain-derived neurotrophic factor
CD11b-FITC	Cluster of differentiation molecule 11b-fluorescein isothiocyanate
CDK	Chronic kidney disease
cDNA	Complementary deoxyribonucleic acid
cm	Centimetres
CNS	Central nervous system
COOH	Hydroxyl
DIV	Days *in vitro*
DMEM	Dulbecco's Modified Eagle Medium
DMSA	Dimercaptosuccinate
DMT1	Divalent metal transporter 1
DNA	Deoxyribonucleic acid
dpi	Dots per inch
E	Embryonic day
EAE	Experimental autoimmune encephalomyelitis
EDTA	Ethylenediaminetetraacetic acid
eGFP	Enhanced green fluorescent protein
FCS	Fetal calf serum
Fe	Elemental iron
FITC	Fluorescein isothiocyanate
GAGs	Glycosaminoglycans
GAPDH	Glyceraldehyde 3-phosphate dehydrogenase

GBCAs	Gadolinium-based contrast agents
Gd-DTPA	Gadolinium-diethylene triamine pentaacetic acid
GDNF	Glial cell line-derived neurotrophic factor
GFAP	Glial fibrillary acidic protein
GFP	Green fluorescent protein
h	Hour(s)
HBSS	Hank's buffered salt solution
ICC	Immunocytochemistry
Iba1	Ionized calcium-binding adaptor molecule 1
IL (-1β, 6, 12)	Interleukin (-1β, 6, 12)
i.v.	Intravenous injection
kD	Kilo-Dalton
kg	Kilogram
LDH	Lactate dehydrogenase
LPS	Lipopolysaccharide
M	Molar
MEM	Minimal Essential Medium
mg	Milligrams
Milli-Q®	Millipore Corporation, ultrapure water of Type 1
min	Minute(s)
MTS	3-(4,5-dimethylthiazol-2-yl)-5-(3-carboxymethoxyphenyl)-2-(4-sulfophenyl)-2H-tetrazolium
MTT	3-(4,5-dimethylthiazol-2-yl)-2,5-diphenyltetrazolium bromide
µmol	Micromole
mmol	Millimole
MRI	Magnetic resonance imaging
n	Sample size
NGF	Nerve growth factor
nm	Nanometer
NO	Nitrogen oxide

P	Postnatal day
PB	Phosphate buffer
PBS	Phosphate buffered saline
PC12	Pheochromocytoma cells
PEG	Polyethylene glycol
Pen/Strep	Penicillin/streptomycin
PFA	Paraformaldehyde
pH	Potential of hydrogen
PI	Propidium iodide
qRT-PCR	Real time quantitative polymerase chain reaction
RES	Reticuloendothelial system
RNA	Ribonucleic acid
ROS	Reactive oxygen species
RT	Room temperature
SEM	Standard error of the mean
SPIO(s)	Superparamagnetic iron oxide nanoparticle(s)
T	Tesla
Tf	Transferrin
TIFF	Tagged Image File Format
TNF- α	Tumour necrosis factor α
Tuj1	Neuron-specific class III β-tubulin antibody
VSOP(s)	Very small superparamagnetic iron oxide nanoparticle(s)

Abstract

Superparamagnetic iron oxide nanoparticles (SPIOs) as contrast agents in magnetic resonance imaging (MRI) have been the subject of extensive research over the past decades. SPIOs are of characteristic sizes ranging from 1 to 100 nm in at least one dimension and are composed of iron oxide cores that are coated with different biodegradable materials. Due to their unique magnetic and physicochemical properties, the list of experimental and clinical research applications of SPIOs has further expanded. However, crucial information regarding interactions of clinically applied SPIOs with cells of the central nervous system (CNS) and potential toxic effects is still lacking. This is of particular importance because SPIOs are capable of penetrating biological barriers, such as the blood-brain barrier and blood-placenta barrier.

The aim of this study was to investigate the morphology and viability as well as the cytokine and chemokine secretion profile of murine primary brain cells that were exposed to clinically relevant SPIOs of different sizes and compositions. For this purpose, I used primary cell cultures of microglia and hippocampal neurons cultured in monocultures and neuron-glia co-cultures. I exposed these primary cells to varying concentrations of two novel very small iron oxide particles (VSOPs) that have already passed clinical phase II trials, or the clinically approved SPIOs ferucarbotran or ferumoxytol for 6 and/or 24 hours, respectively. I show that SPIO accumulation by primary brain cells strongly depends on the cell type, exposure condition as well as particle type. Primary microglia strongly accumulated the smallest, citrate-coated VSOPs and the largest, carboxydextran-coated ferucarbotran but not the medium-sized, carboxymethyldextran-coated ferumoxytol verified by intense Prussian blue staining. Using immunocytochemistry, I show that SPIO accumulation causes morphological alterations from a ramified to an amoeboid shape, indicating microglial activation. Propidium iodide staining revealed that microglial viability was severely compromised, especially, when cells were exposed to high SPIO concentrations of 1.5 and 3.0 mM and incubated for 24 hours. While ferumoxytol was only moderately accumulated by microglia without significantly affecting viability, it still induced morphological alterations. Just as detected for microglia, only VSOPs and ferucarbotran, but not ferumoxytol, are accumulated by primary neurons, especially, after exposure to the highest iron concentration of 3.0 mM. However, all SPIOs, independent of the particle size, composition and the applied iron concentration severely affected the morphology of primary neurons from monocultures after 24 hours of exposure, which is revealed using Sholl analysis. Neurons cultured without glial cells show reduced number of neurites and increased numbers of degenerated cells in comparison to untreated neurons. In contrast, SPIO exposure of neurons in neuron–glia co-cultures seems to have a stimulatory effect on neurites. However, the analyses of secreted cytokines and chemokines secretion does not show any tendencies of SPIO-mediated effects. From the represented data I conclude that the effect of SPIOs on brain cells not only strongly depends on the respective nanoparticle type and concentration but also on the physiological microenvironment they are applied to.

German Abstract

Die Verwendung von superparamagnetischen Eisenoxid-Nanopartikeln (SPIOs) als Kontrastmittel in der Magnetresonanztomographie (MRT) ist seit Jahrzehnten Gegenstand intensiver Forschung. SPIOs bewegen sich in einer charakteristischen Größenordnung, die in mindestens einer Dimension zwischen 1 bis 100 nm liegt. Sie bestehen aus Eisenoxidkernen, die mit unterschiedlichen, biologisch abbaubaren Materialien beschichtet sind. Aufgrund der einzigartigen magnetischen und physikochemischen Eigenschaften von SPIOs nimmt die Liste der potentiellen Anwendungsmöglichkeiten in der experimentellen und klinischen Forschung stetig zu. Jedoch fehlen bislang grundlegende Informationen hinsichtlich der Wechselwirkung von SPIOs mit Zellen des zentralen Nervensystems (ZNS) und der potentiell toxischen Auswirkungen. Dies ist von außerordentlicher Relevanz, denn SPIOs können entsprechend ihrer Komposition biologische Barrieren, wie z.B. die Blut-Hirn-Schranke und Blut-Plazenta-Schranke überwinden. Aus diesem Grund war es Ziel meiner Untersuchungen sowohl die Morphologie und Vitalität von primären Hirnzellen als auch den Einfluss auf die Sekretion von Zytokinen und Chemokinen nach Inkubation mit klinisch relevanten SPIOs unterschiedlicher Größe und Zusammensetzung zu erforschen. Zu diesem Zweck verwendete ich primäre Zellkulturen von Mikroglia und hippocampalen Neuronen, die in als Monokultur oder Neuron-Glia Co-Kultur gezüchtet wurden. Die primären Zellkulturen wurden jeweils für 6 und/oder 24 Stunden, zum einen, mit neuartigen ‚Very Small Iron Oxide Nanoparticles' (VSOPs), welche die klinische Prüfungsphase II durchlaufen haben und, zum anderen, mit den klinisch geprüften SPIOs Ferucarbotran und Ferumoxytol inkubiert. Ich zeige, dass die Akkumulation von SPIOs durch primäre Hirnzellen vom jeweiligen Zelltyp, der Expositonsbedingung und dem Partikeltyp abhängen. Anhand der Berliner Blau Färbung wird deutlich, dass die kleinsten, Zitrat-beschichteten VSOPs und das größte, Carboxydextran-beschichtete Ferucarbotran, jedoch nicht das Carboxymethyldextran-beschichtete Ferumoxytol mittlerer Größe, verstärkt von Mikroglia akkumuliert werden. Mithilfe der Immunzytochemie weiße ich nach, dass SPIO-Akkumulationen morphologische Veränderungen primärer Mikroglia, von einem ramifizierten zu einem amöboiden Phänotyp bewirken. Die Propidiumiodid-Färbung beweist, dass die Vitalität von Mikroglia insbesondere durch hohe Partikelkonzentrationen von 1.5 und 3.0 mM und einer Inkubationsdauer von 24 Stunden stark beeinträchtigt wird. Obwohl Ferumoxytol kaum aufgenommen und die Vitalität von Mikroglia nicht gravierend beeinflusst wird, zeigen sich morphologische Veränderungen. Inkubation von primären Neuronen mit VSOPs und Ferucarbotran, nicht jedoch Ferumoxytol, weist vor allem bei hohen Eisenkonzentration von 3.0 mM Partikelablagerungen auf. Die Sholl-Analyse von Neuronen aus Monokulturen zeigt, dass die neuronale Morphologie nach 24-stündiger SPIO-Inkubation unabhängig von der Partikelgröße, Komposition und eingesetzter Eisenkonzentration gravierend beschädigt ist. Dies spiegelt sich anhand einer verringerten Anzahl von Neuriten und einer erhöhten Zahl degenerierter Zellen im Vergleich zu unbehandelten Neuronen wieder. Im Gegensatz dazu ist bei Neuronen aus Co-Kulturen nach SPIO-Exposition ein stimulierender Effekt auf Neuriten zu beobachten. Jedoch zeigt die Zytokin- und Chemokin-Analyse keine Tendenzen bezüglich SPIO-vermittelter Effekte. Die vorliegenden Ergebnisse lassen darauf schließen, dass der Einfluss von SPIOs auf Hirnzellen nicht nur vom jeweiligen Partikeltyp und Eisenkonzentration, sondern auch vom physiologischen System abhängt.

1 Introduction

1.1 Nanoparticles

A broad range of products in daily use include materials that are produced with the assistance of nanotechnology (Buzea et al. 2007; Kessler 2011; Contado 2015). These engineered materials exhibit sizes on a nanoscale level measuring between 1 to 100 nm in at least one dimension (Oberdorster et al. 2005; Pettitt and Lead 2013). By virtue of their small size and resulting high surface-to-volume ratio, nanomaterials exert exceptional biological properties that differ substantially from larger scale particles of the same composition (Nel et al. 2006; Buzea et al. 2007; Contado 2015). These include increased chemical reactivity and bioavailability compared to their macroscopic counterparts. Since manufacturing began in the 1980s, nanomaterials have been exploited in a broad spectrum of applications, ranging from material engineering via agriculture and consumer products to applications in medicine and healthcare (Buzea et al. 2007; Laux et al. 2018). In commercially available products, nanoscale materials as ingredients are predominantly used in the form of nanoparticles, such as silicon dioxide, titanium dioxide, zinc oxide, nanosilver and iron oxide to improve product quality of food, pharmaceutics and cosmetics (Buzea et al. 2007; Kessler 2011; Contado 2015). Despite great progress in nanoparticle characterization, which has benefitted various applications, oral and dermal uptake of nanoscale ingredients in consumer products as well as nanoparticle incorporation through inhalation has resulted in a growing concern about their potential toxicity and environmental impact (Oberdorster et al. 2005; Buzea et al. 2007; Laux et al. 2018). For instance, inhalation of diesel exhaust nanoparticles has been shown to cause neuronal damage (Block et al. 2004; Levesque et al. 2011). Through systemic circulation, nanoparticles are distributed to various organs, including the brain, where their small size allows for microvascular penetration facilitating direct cell contact. Due to their ability to interact and cross biological barriers, such as the blood-brain barrier (BBB) and blood-placenta barrier (Lockman et al. 2004; Nel et al. 2006; Hu and Gao 2010; Wang et al. 2010; Yang et al. 2010; Cartwright et al. 2012; Muller et al. 2018) , nanoparticle incorporation poses serious risks and unforeseen side effects to human health that are difficult to predict in advance. Concerns are attributed to their size and enhanced, surface-to-volume ratio-dependent adsorption, when considering dimensions of biological components (Figure 1). Cells of living organisms are between 10 to 200 µm in size and are composed of much smaller molecules, such as proteins measuring 5 to 50 nm or DNA measuring 2 nm in diameter (Figure 1). In comparison, nanoparticles are in the size domain of viruses emphasising their potential to also affect subcellular processes (Figure 1) (Buzea et al. 2007).

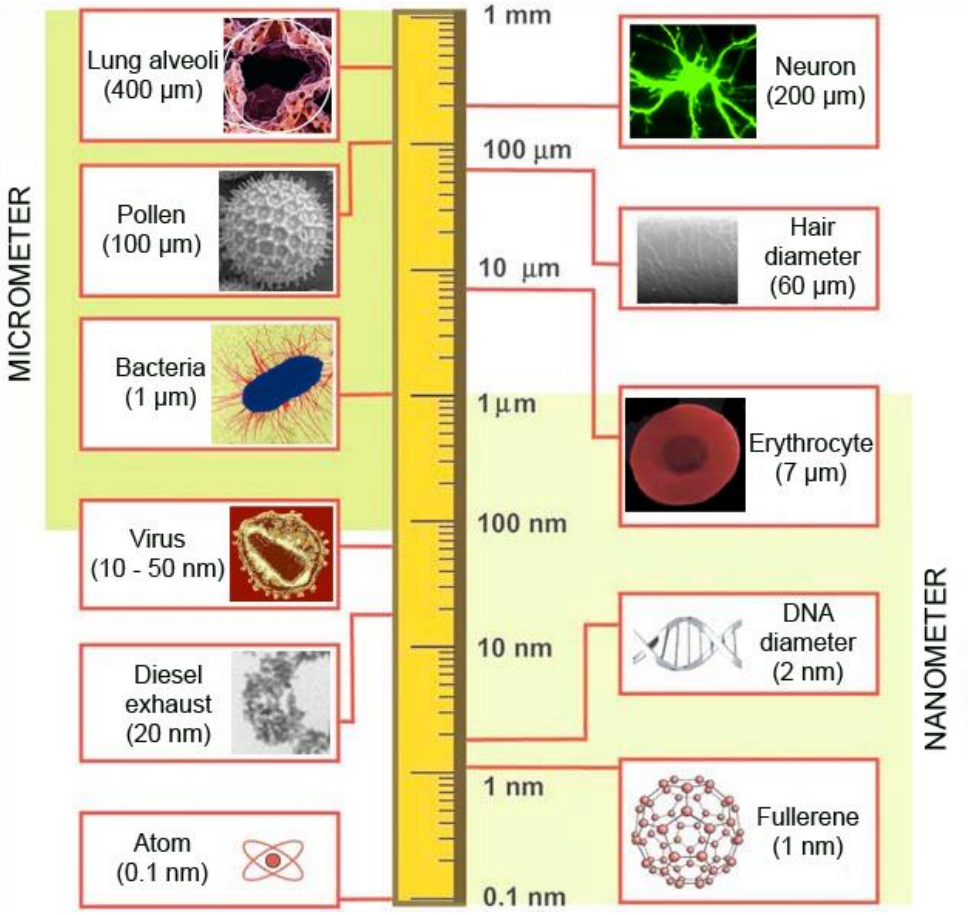

Figure 1: Illustration of biological components compared in sizes ranging from nano- to micrometer on a logarithmic scale. Adapted from (Buzea et al. 2007)

These size differences, however, made it possible to use nanoparticles as very small probes to directly observe and manipulate cellular components, which became of special interest in the field of biomedical research (Salata 2004; Gupta and Gupta 2005; Rumenapp et al. 2012; Ali et al. 2016). Here, nanoparticles consisting of iron oxide cores with attractive qualities, such as specific magnetization and beneficial physical and chemical properties were exploited (Wang et al. 2001; Gupta and Gupta 2005; Ali et al. 2016). Originally, iron oxide nanoparticles were intravenously administered for the treatment of iron deficiency anaemia (Cameron et al. 1951; Spinowitz et al. 2008; Lu et al. 2010). Rapid development in nanotechnology in combination with tailored surface engineering made it possible to utilize these particles in a broad range of experimental and clinical applications (Lin et al. 2008a; Ali et al. 2016).

The fundamental reasons for the increased focus on iron oxide as compared to other metal oxide nanoparticles, such as cobalt, nickel and manganese, is due to their biocompatibility (Gupta and Gupta 2005; Shubayev et al. 2009; Ittrich et al. 2013). Iron is the second most abundant transition metal on earth and is predominantly found as iron (III) oxide in the form of rust as brown coloured pigment because it readily combines with oxygen (Sadrzadeh and Saffari 2004; Ali et al. 2016). In the human body, iron is found bound to the heme protein in the form of haemoglobin of blood, myoglobin of muscles, and in iron-containing enzymes, such as catalase and cytochromes, or it is found as a non-heme iron in blood plasma, bound to its transport glycoprotein transferrin or is deposited in the iron storage proteins ferritin and

hemosiderin (Lieu et al. 2001; Sadrzadeh and Saffari 2004). Additionally, iron participates in a wide range of highly regulated metabolic processes, including oxygen transport, hemoglobin and DNA synthesis, myelin formation and dendrite development (Lieu et al. 2001; Sadrzadeh and Saffari 2004). Its biological importance is due to its capability to obtain multiple redox states as ferrous (Fe^{2+}) and ferric (Fe^{3+}) iron via the Fenton reaction, which can also cause oxidative cell damage by generating reactive oxygen species (ROS), such as hydroxyl and superoxide radicals (Lieu et al. 2001; Sadrzadeh and Saffari 2004). Nevertheless, the physicochemical and magnetic properties of iron have diverted its potential as an iron oxide nanoparticle for biomedical applications. Progress in nanotechnology and science led to the fabrication of iron oxide nanoparticles of defined sizes and coated with different biocompatible materials in order to prevent their reaction with oxidizing agents and to specifically interact with tissues and cells (Gupta and Gupta 2005; Wu et al. 2015a; Ali et al. 2016). The most commonly found forms of iron oxide are hematite (α-Fe_2O_3), magnetite (Fe_3O_4) and its oxidized form maghemite (γ-Fe_2O_3) (Gupta and Gupta 2005; Laurent et al. 2008; Wu et al. 2015a; Ali et al. 2016). Only the latter two iron oxides have attracted attention in biomedical applications due to their specific magnetic properties at nanoscale size (Rumenapp et al. 2012; Wu et al. 2015a). Iron oxide nanoparticles with cores in sizes below 20 nm exhibit a unique form of ferromagnetism, called superparamagnetism (Wang et al. 2001; Gupta and Gupta 2005; Rumenapp et al. 2012; Ali et al. 2016).

1.1.1 Superparamagnetic iron oxide nanoparticles (SPIOs)

Superparamagnetic iron oxide nanoparticles (SPIOs) are a class of contrast agents in magnetic resonance imaging (MRI) that significantly improve tissue discrimination by influencing proton relaxation times and, thereby, increase MRI sensitivity (Wang et al. 2001; Weinstein et al. 2010; Ittrich et al. 2013; Shokrollahi 2013). SPIOs are comprised of crystalline ferri- (Fe^{3+}) and ferro- (Fe^{2+}) magnetic cores in the form of Fe_3O_4 and γ-Fe_2O_3 (Wang et al. 2001; Gupta and Gupta 2005). By virtue of their small size, these ferromagnetic particles lose their permanent magnetism. Instead, they exhibit superparamagnetism, which refers to the special ability of the iron oxide cores to be magnetized in the presence of an external magnetic field and to completely lose magnetization once the magnetic field has been removed (Hendrick and Haacke 1993; Di Marco et al. 2007). The superparamagnetism-based large magnetic susceptibility of SPIOs strongly affects the relaxivity of surrounding tissue in MRI, which results in a strong tissue contrast (Wang et al. 2001; Taupitz et al. 2003; Wang 2011; Ittrich et al. 2013). Using SPIO-based contrast agents, a higher spatial resolution and diagnostics accuracy can be achieved compared to similar concentrations of conventional used paramagnetic gadolinium-based contrast agents (GBCAs) in clinical practice (Ittrich et al. 2013; Shokrollahi 2013; Pierre et al. 2014).

At present, GBCAs, for instance Magnevist® (Bayer Schering Pharma AG), are predominantly used for clinical MRI (Shokrollahi 2013; Pierre et al. 2014). GBCAs consist of the rare earth element gadolinium, which is complexed with chelates, such as gadolinium-diethylene triamine pentaacetic acid (Gd-DTPA) because bare gadolinium ions are highly toxic. Although GBCAs provide an excellent tissue contrast, they are rapidly eliminated by the kidneys after intravenous administration and they do not allow for specific imaging of organ or tissue pathologies (Shokrollahi 2013). Furthermore, GBCAs bear the risk of causing

nephrotic systemic fibrosis in patients with impaired kidney function or renal insufficiency (High et al. 2007; Neuwelt et al. 2009; Ittrich et al. 2013). Moreover, findings about deposition of GBCAs within the brain and induced neurotoxicity raised concerns about their administration (Feng et al. 2010; Kanda et al. 2016; Gulani et al. 2017; Pasquini et al. 2018). For this reason, SPIOs appeared to be an attractive alternative with a better safety profile (Neuwelt et al. 2009; Chen et al. 2015; Iv et al. 2015; Wei et al. 2017). SPIOs have also been used in combination with GBCAs for pre-therapeutic evaluation in order to achieve higher accuracy with MRI (Weinstein et al. 2010; Shokrollahi 2013; Mao et al. 2016).

Apart from their unique magnetic properties, the use of SPIOs as contrast agents in MRI further necessitate a biocompatible surface coating, which isolates the bioactive iron to prevent interaction with blood plasma components and prolongs blood circulation time for target-specific imaging. Therefore, SPIOs are coated with polymers, such as dextran, carbohydrate derivatives, polyethylene glycol (PEG), albumin and starch, or monomers, such as citrate and dimercaptosuccinate (DMSA) (Wang et al. 2001; Taupitz et al. 2003; Gupta and Gupta 2005; Laurent et al. 2008). The coating material decisively determines the overall particle size because in aqueous solution a hydration layer that increases the effective particle diameter instantly surrounds surface-coated SPIOs. Thus, SPIO size is usually defined by its hydrodynamic diameter (Wang et al. 2001; Wu et al. 2015a). Most commercially available SPIOs are coated by biodegradable polymers that have a high affinity to iron and relatively large hydrodynamic diameters. In comparison, electrostatically stabilized SPIOs coated with monomers exhibit a much smaller surface area and, therefore, much smaller hydrodynamic diameters then polymer-coated SPIOs (Taupitz et al. 2004; Laurent et al. 2008; Ittrich et al. 2013). According to their hydrodynamic diameter, SPIOs are categorized into different subgroups. Standard SPIO sizes in experimental and clinical applications range from 40 to 150 nm, whereas SPIOs in sizes around 20 to 40 nm are referred to as ultrasmall superparamagnetic iron oxide nanoparticles. The smallest group of SPIOs, called very small superparamagnetic iron oxide nanoparticles (VSOPs) exhibit hydrodynamic sizes below 10 nm (Wang et al. 2001; Taupitz et al. 2004; Wagner et al. 2011; Ittrich et al. 2013). Size, surface coating and charge of SPIOs decisively determine their pharmacokinetics and organ distribution. Following intravenous injection, larger SPIOs with diameters above 100 nm are eliminated within minutes from circulation by resident, tissue-specific macrophages of the reticuloendothelial system (RES), which is comprised of the liver, spleen, lymph nodes and bone marrow (Taupitz et al. 2003; Saito et al. 2012; Ittrich et al. 2013; Ali et al. 2016). The RES is responsible for removing and degrading foreign elements, including pathogens and non-biological particles. As the total phagocytic capacity is predominantly implemented by resident macrophages in the liver, 80 – 90 % of intravenously injected SPIOs accumulate in this organ, and to a lesser degree in the spleen (5 – 8 %) and bone marrow (1 – 2 %) (Ittrich et al. 2013). In contrast, SPIOs smaller than 50 nm transiently escape recognition by macrophages and show a prolonged blood half-life of up to several hours (Roohi et al. 2012; Saito et al. 2012).

With respect to the passive targeting of RES organs after intravenous injection, SPIOs with deliberately engineered physicochemical features have been explored as MRI contrast agents for visualizing pathological tissue alterations of liver and spleen for more than two decades (Taupitz et al. 2003; Weinstein et al. 2010; Ittrich et al. 2013). Through systematic modification in size and surface coating as well as surface functionalization with targeting ligands, such as antibodies, other fields of experimental and clinical SPIO applications have emerged. For example, SPIOs are of interest for cell-based therapies, where *in*

vitro labelling of stem or immune cells and *in vivo* tracking is investigated for MR imaging of inflammatory diseases (Ittrich et al. 2013). Here, VSOPs have been shown to yield superior labelling efficiency and visualization of mesenchymal stem cells, neuronal precursor cells, macrophages and T cells (Stroh et al. 2006; Wuerfel et al. 2011; Poller et al. 2016a). By virtue of their superior uptake by phagocytic macrophages, SPIOs have been investigated as contrast agents to image inflammatory lesions in experimental autoimmune encephalomyelitis (EAE), a mouse model for multiple sclerosis (Petry et al. 2007; Ittrich et al. 2013; Millward et al. 2013). Especially, the diagnosis and treatment of CNS pathologies with the help of SPIOs is one main focus due to the significant challenge of delivering contrast agents for imaging into the brain (Silva 2010; Gendelman et al. 2015; Silva Adaya et al. 2017). Recently, SPIOs conjugated with appropriate antibodies have been shown to target amyloid beta plaques in an animal model for Alzheimer's disease, where the blood-brain barrier is impaired (Yang et al. 2011b; Wadghiri et al. 2013; Zhang et al. 2015). Biomedical studies are also exploring SPIOs as drug carriers to bypass the blood-brain barrier, for specific tumour targeting and subsequent treatment using magnetic hyperthermia (Barbu et al. 2009; Silva 2010; Chatterjee et al. 2011; Wahajuddin and Arora 2012; Iv et al. 2015). Furthermore, the feasibility of SPIO-based contrast agents are being tested for diagnosing cerebral ischemia, arteriosclerotic plaques, vascular thrombi and neurodegenerative as well as neuroinflammatory diseases (Weinstein et al. 2010; Wagner et al. 2011; Ittrich et al. 2013).

1.1.2 Clinically relevant SPIOs

Currently, a small number of SPIOs differing in surface coating and charge are approved by the United States Food and Drug Administration (FDA) or the European Medicines Agency (EMA) as contrast agents for diagnostics with MRI (Ittrich et al. 2013; Gendelman et al. 2015; Iv et al. 2015; Anselmo and Mitragotri 2016). These include the commercially available ferucarbotran (Resovist®, Meito Sangyo, Japan) and ferumoxytol (Feraheme®, AMAG Pharmaceuticals Inc., USA) (Reimer and Balzer 2003; Balakrishnan et al. 2009), which are used for preclinical and clinical applications (Taupitz et al. 2003; Weinstein et al. 2010; Ittrich et al. 2013; Toth et al. 2017).

The EMA-approved carboxydextran-coated ferucarbotran, also known under the trade name Resovist®, with a hydrodynamic diameter of 60 nm has successfully been applied as a liver-specific contrast agent in clinical MRI to detect tissue pathologies (Table 1) (Reimer and Balzer 2003; Taupitz et al. 2003; Weinstein et al. 2010; Ittrich et al. 2013). Due to weak demand and marketing strategy, manufacturing of ferucarbotran has been discontinued in 2009 in Europe but it is still internationally available in pharmaceutical quality from Meito Sangyo in Japan (Yang et al. 2011a; Ittrich et al. 2013). Therefore, ferucarbotran is still under investigation for potential fields of application, including biomedical research (Yang et al. 2011a; Araya et al. 2013; Burkhart et al. 2016).

Due to limitations in using GBCAs as mentioned in the previous section, ferumoxytol as one of the few clinically approved SPIO-based contrast agents represents a reliable alternative (Weinstein et al. 2010; Ittrich et al. 2013; Iv et al. 2015). The carboxymethyldextran-coated ferumoxytol, also known under the trade name Feraheme®, with a hydrodynamic diameter of 30 nm was originally developed as contrast agent for MRI but only holds FDA-approval for iron replacement therapy for treating iron-deficiency anaemia

in patients with chronic kidney disease (CKD) (Prince et al. 2003; Lu et al. 2010; Kowalczyk et al. 2011; Toth et al. 2017). For human MRI, vials of 17 ml containing ferumoxytol in isotonic formulation and 510 mg of elemental iron are diluted using saline to a total volume of 24 – 60 ml prior intravenous administration over 15 min (Vasanawala et al. 2016). Ferumoxytol is investigated for various clinical imaging applications. Off-label clinical use includes imaging of central nervous system (CNS) pathologies, where ferumoxytol is used as a blood pool-contrast agent to visualize vascular malformations and to create cerebral blood-volume maps with MRI (Table 1) (Weinstein et al. 2010; Anselmo and Mitragotri 2016; Toth et al. 2017). Moreover, ferumoxytol is investigated for MRI of inflammatory CNS lesions to evaluate macrophage-rich brain regions (Weinstein et al. 2010; McConnell et al. 2016; Toth et al. 2017). Under pathological conditions with dysfunctional blood-brain barrier, ferumoxytol can be taken up by monocytes that infiltrate the brain or by brain resident microglia and astrocytes (McConnell et al. 2016). However, potential toxic effects of ferumoxytol after accumulating in the brain parenchyma have not been thoroughly investigated. The fact that ferumoxytol is being used beyond its approval for MRI of the CNS, including imaging of brain tumours in children and for cardiac MRI of neonates and young infants (Thompson et al. 2012; Ruangwattanapaisarn et al. 2015; Lai et al. 2017) emphasises the need for detailed studies concerning the impact on cells of the CNS.

Apart from commercially available nanoparticles, preclinical studies are currently investigating the utility of substantially smaller VSOPs for advanced imaging approaches, such early stage clinical diagnostics and molecular imaging (Table 1) (Tysiak et al. 2009; Ittrich et al. 2013; Poller et al. 2016b). VSOPs are electrostatically stabilized particles and exhibit sizes of approximately 7 nm, which is achieved by monomer-coating with citrate (Taupitz et al. 2004; Wagner et al. 2011). Citrate as a coating material is beneficial not only because of its influence on the effective particle size but also because it is an endogenous substance naturally occurring in mammals and is, thus, well tolerated and metabolized (Taupitz et al. 2000). The small size of VSOPs prolongs their blood circulation time and offers the advantage of an increased contact time with target tissues, which improves sensitivity of MRI and can be exemplified by VSOP-C184 (Ferropharm GmbH). Therefore, VSOPs were found to be suitable for vascular diagnostics with MR angiography (Taupitz et al. 2000; Taupitz et al. 2004; Weinstein et al. 2010; Wagner et al. 2011; Ittrich et al. 2013; Millward et al. 2013). Moreover, VSOPs have been shown to target atherosclerotic lesion, enabling visualization of atherosclerotic plaques in MRI, which helps to assess the pathological mechanisms in atherogenesis (Ludwig et al. 2013; Wagner et al. 2013; Poller et al. 2016b). Another advantage of VSOPs is that their cellular incorporation is significantly increased compared to larger particles coated with polymers, such as ferucarbotran or ferumoxytol (Saito et al. 2012; Schweiger et al. 2012). Several studies have shown that VSOPs yield superior labelling efficiency and visualization of mesenchymal stem cells, neuronal precursor cells, macrophages and T cells (Stroh et al. 2006; Wuerfel et al. 2011; Poller et al. 2016a). Currently, different versions of VSOPs are under intensive investigation for cellular and molecular imaging, including VSOP-R1 and VSOP-R2 that were developed at the Institute for Radiology, Charité-Universitaetsmedizin Berlin (Taupitz et al. 2003; Wagner et al. 2011; Ittrich et al. 2013; Ludwig et al. 2013; Neubert et al. 2015; Poller et al. 2016a; Pohland et al. 2017).

These VSOPs are of special interest as MRI probes to detect various pathologies of the CNS and have been used to detect BBB breakdown and neuroinflammation in EAE (Tysiak et al. 2009; Millward et al. 2013; Millward et al. 2017). Furthermore, VSOPs conjugated with targeting ligands, such as annexin A5 allowed for visualization of apoptotic cells with MRI (Figge et al. 2014). Thus, the unique properties of VSOPs combine the advantages of prolonged blood circulation time needed to detect arteriosclerotic plagues (Ludwig et al. 2013; Wagner et al. 2013), improved detection of impaired BBB (Tysiak et al. 2009; Millward et al. 2013) and visualization of VSOP-labelled macrophages (Stroh et al. 2006; Wuerfel et al. 2011) that migrate to inflammatory lesions. These examples illustrate the potential use of VSOPs for very new approaches to visualize different pathological events related to CNS inflammation.

Table 1: Clinically relevant SPIOs.

Generic name Trade name (synonym)	**Clinical dose (µmol Fe/kg)**	**Blood half-life**	**Indication/ MRI**	**Manufacturer**	**References**
Ferucarbotran Resovist® Cliavist® (SHU 555A)	8 – 12	10 min	Liver lesions, spleen, bone marrow	Meito Sangyo	(Reimer and Balzer 2003; Taupitz et al. 2003; Weinstein et al. 2010; Anselmo and Mitragotri 2016)
Ferumoxytol Feraheme® Rienso® (Code 7228)	160 - 320	10 – 14 h	Iron deficiency anaemia, Imaging: brain & lymph node metastases, neuroinflammation in epilepsy, head/ neck cancer, myocardial infarction, multiple sclerosis	AMAG Pharmaceuticals Inc. Takeda Pharmaceutical Company Limited	(Weinstein et al. 2010; Anselmo and Mitragotri 2016; Vasanawala et al. 2016; Toth et al. 2017)
VSOP-C184	15 – 75 45 (bolus)	30 – 60 min	MR-angiography	Ferropharm GmbH	(2004; Taupitz et al. 2004; Weinstein et al. 2010; Ittrich et al. 2013)
VSOP-R1 (batch 080610)	75	30 min	MR-angiography Atherosclerotic plaque MRI Detection of early CNS inflammation	Charité Institute of Radiology	(Wagner et al. 2011; Millward et al. 2013)

Generic name Trade name (synonym)	**Clinical dose (µmol Fe/kg)**	**Blood half-life**	**Indication/ MRI**	**Manufacturer**	**References**
VSOP-C200	20 – 70	40 – 60 min	Cell labelling and tracking	Ferropharm GmbH	(Stroh et al. 2006; Wuerfel et al. 2011)
VSOP-R2 (batch 050701)	75	30 min	MR-angiography Cell labelling and tracking	Charité, Institute of Radiology	(Tysiak et al. 2009; Ludwig et al. 2013; Poller et al. 2016a)

1.2 Brain cells and primary cultures

The brain consists of two main cell types, neurons and glia that vary in ratio across brain structures (Herculano-Houzel 2014; Peters and Connor 2014). In the CNS, the number of glial cells range from 40 to 130 billion and the number of neurons reaches approximately 86 billion (Herculano-Houzel 2014; von Bartheld et al. 2016). The interconnected glial cells can be further divided into oligodendrocytes, astrocytes and microglia, supporting neurons metabolically and functionally (Kettenmann and Verkhratsky 2008). Primary cultures of brain cells obtained from rodent brains are convenient model systems to study influences on cellular morphology and viability as well as cell-cell communication under controlled conditions. In addition, primary cell cultures allow for direct investigation of distinct responses of individual cells, which is certainly more challenging within the complex cellular network of the brain. In order to more closely relate to the *in vivo* brain environment, co-cultures of primary neurons and glial cells provide a practical alternative, which also prevents the necessity for animal experiments (Gordon et al. 2013). Importantly, interactions of neurons and glial cells are crucial for maintaining neuronal vitality (Schmalenbach and Muller 1993; Park et al. 2001). The use of primary brain cell cultures, either cultivated individually or in co-culture with other cell types has made major contribution to understand their functions within the brain.

In the following sections, the focus will be on the main characteristics, including morphology, physiology and partly pathology of neurons and microglia.

1.2.1 Neurons

Neurons are highly polarized cells in the CNS with the ability to communicate specifically and rapidly with each other and other brain cells through their unique excitability (Craig and Banker 1994; Peters and Connor 2014). In the course of neuronal development, neurons sprout and elongate two types of

morphologically and functionally distinguishable processes. Each neuron comprises several widely ramified dendrites that constitute the receptive field and one long tubular axon that propagates electrical signals (Barnes and Polleux 2009; Peters and Connor 2014). After neuronal development is complete, synapses at branched terminals of an axon and spines on dendritic branches are formed, establishing a complex network of interconnected neurons (Barnes and Polleux 2009; Biffi et al. 2013). Impulse propagation throughout the neuronal network depends partly on the capacity of incoming signals to depolarize the neuronal membrane, whereas the neuronal soma acts as an interface for signal integration and generation of action potentials (reference). Upon depolarization of the neuronal membrane and subsequent action potential generation at the axon hillock, the electrical signal is propagated towards the synapse. This results in an increase of intracellular calcium levels in the synapse and regulatory exocytosis of secretory vesicles containing neurotransmitters or neuromodulators (Scalettar 2006). Released neurotransmitters bind to their receptors of the postsynaptic neuron causing an excitatory or inhibitory response that subsequently affects further signal transmission.

In vitro cell culture models of neurons have been frequently applied to study effects of a diverse range of stimuli, including nanoparticles on neuronal morphology and functionality (Oberdorster et al. 2005)

1.2.1.1 Primary neuronal cultures

Cultures of primary neurons can be prepared from different brain regions (Hansson et al. 1984). Primary cultures allow direct access for observation and manipulation of living neurons across days and weeks (Beaudoin et al. 2012). Furthermore, the physiological setting of neurons in culture is far less complex than *in vivo* (Beaudoin et al. 2012). A well-established model system to study neuronal differentiation and morphology are primary hippocampal neurons (Bradke and Dotti 2000; Kaech and Banker 2006; Biffi et al. 2013). The hippocampus plays major roles in cognition, learning and memory and is significantly affected in a variety of neurological disorders, such as Alzheimer's disease, epilepsy, schizophrenia, depression and stroke (Small et al. 2011; Anand and Dhikav 2012). The principle cell type in the hippocampus is the glutamatergic pyramidal neuron with its characteristic pyramidal-shaped morphology (Beaudoin et al. 2012). They are some of the largest neurons in the brain and make up the vast majority of cells in the preparation (Kaech and Banker 2006). Morphologically, pyramidal neurons possess a long axon and a long apical dendrite originating from the apex as well as short basal dendrites emerging from the base of the cell body. Therefore, pyramidal neurons can easily be distinguished from smaller inhibitory interneurons (Kaech and Banker 2006; Beaudoin et al. 2012). Compared with most other regions of the CNS, the hippocampus in a late embryonic stage contains fewer glial cells than, for instance, the cortex and its cell population is relatively simple to differentiate (Fletcher and Banker 1989; Kaech and Banker 2006). Therefore, hippocampal neurons are predominantly isolated from embryonic mice (Kaech and Banker 2006). Maintained in culture, embryonic neurons follow a common sequence of five developmental stages to acquire their polarity and form well-established synapses (Dotti et al. 1988; Fletcher and Banker 1989), allowing synaptic transmission and plasticity after 7 days *in vitro* (DIV7) (Ichikawa et al. 1993). The maintenance of hippocampal neurons in culture can be supported by glial cells providing trophic factors (Schmalenbach and Muller 1993; Kaech and Banker 2006). Therefore, culturing neurons together with

astrocytes and microglia as neuron-glia co-cultures improves viability and survival (Dotti et al. 1988; Park et al. 2001; Kaech and Banker 2006; Jones et al. 2012). In a classic co-culture model, an astroglial feeder layer is grown in cell culture plates. Hippocampal neurons grown on the underside of glass cover slips are then transferred into the culture (Kaech and Banker 2006; Jones et al. 2012). This neuron-glia co-culture system is a convenient approach to include the contribution of astrocytes to growing neurons (Jones et al. 2012).

1.2.2 Glial cells

Glial cells of the CNS fulfil crucial functions in brain metabolism, development, immune surveillance, synapse formation, influencing of neuronal activity as well as the pathogenesis of neurological diseases (Kettenmann and Verkhratsky 2008; Herculano-Houzel 2014). Within the brain, there are four major populations of glia cell types, microglia, astrocytes, oligodendroglia and their progenitors, NG2-glia (Jakel and Dimou 2017). Only glial cells relevant in this thesis will be described in detail.

1.2.2.1 Astrocytes

In the brain, astrocytes are the most abundant cell type (Sofroniew and Vinters 2010; Oberheim et al. 2012; Gonzalez-Perez et al. 2015). Due to their spatial proximity to each other, neurons and the vasculature, astrocytes modulate a variety of functions (Oberheim et al. 2012; Gonzalez-Perez et al. 2015; Liu et al. 2017). For example, astrocytes maintain and influence the integrity of the BBB with their perivascular end feet (Abbott 2002). They also provide neuroprotection, for instance, through uptake and release of neurotransmitters (Liu et al. 2017). Similar to microglia, astrocytes become functionally activated in a gradated continuum of progressive cellular and molecular alterations as a response to all forms of CNS pathologies, including infection, trauma and neurodegenerative diseases (Sofroniew and Vinters 2010; Pekny et al. 2016; Liu et al. 2017). Astrocytes rapidly change their morphology and molecular expression in a process called reactive astrogliosis that can have beneficial roles or cause detrimental effects (Sofroniew 2014; Pekny et al. 2016; Liu et al. 2017). Reactive astrogliosis is also induced through damage of the BBB as a consequence of pathological processes, such as cerebral ischemia, multiple sclerosis and Alzheimer's disease and can be used as a reliable marker of damaged tissue (Sofroniew and Vinters 2010; Sofroniew 2014; Liu et al. 2017). Morphologically, reactive astrocytes are characterized by variable degrees of hypertrophy of the cell body and processes, which is accompanied by limited proliferation and increased GFAP expression (Sofroniew and Vinters 2010; Oberheim et al. 2012; Liu et al. 2017). As a response to extreme levels of activation along borders of severe damage or inflammation, reactive astrogliosis leads to scar formation. To protect healthy tissue, the glial scars function not only as barriers for axon regeneration but also prevents invasion of inflammatory cells (Oberheim et al. 2012; Sofroniew 2014).

Other important functions of astrocytes are the regulation of metal homeostasis in the brain and protection of neurons from metal-induced toxicity and oxidative stress (Tiffany-Castiglion and Qian 2001; Dringen et al. 2007; Macco et al. 2013; Pelizzoni et al. 2013; Migliore et al. 2015; Liu et al. 2017). Consequently, the interaction of metal-based nanoparticles with astrocytes has already been extensively investigated (Au et

al. 2007; Geppert et al. 2009; Ding et al. 2010; Geppert et al. 2011; Lamkowsky et al. 2011; Geppert et al. 2012; Hohnholt and Dringen 2013; Hohnholt et al. 2013; Sun et al. 2013; Schaub et al. 2014; Migliore et al. 2015; Petters et al. 2016). Therefore, a central focus of this thesis is on microglial cells and detailed information about their function in the brain presented is in the following section.

1.2.2.2 Microglia

Microglia are the immunocompetent cells in the CNS with unique functions under physiological and pathological conditions (Hanisch and Kettenmann 2007; Kettenmann et al. 2011; Walker et al. 2014; Sousa et al. 2017). Despite functional similarities, microglia represent a specialized cell population compared to non-parenchymal CNS macrophages, namely perivascular, meningeal and choroid plexus macrophages (Katsumoto et al. 2014; Goldmann et al. 2016). They are the only myeloid cells originating from erythromyeloid progenitors in the yolk sac (Ginhoux et al. 2010; Gomez Perdiguero et al. 2015). Microglia migrate into the CNS during early embryogenesis until the blood-brain barrier is formed and remain throughout adulthood via constant self-renewal (Ajami et al. 2007; Goldmann et al. 2016).
Under physiological conditions, microglia fulfil a number of immunological and non-immunological functions crucial for brain development, adult neuroplasticity and neuroprotection (Town et al. 2005; Tay et al. 2017). During brain development, microglia are involved in the establishment of neuronal connectivity through synaptic pruning and refinement (Paolicelli et al. 2011). In the mature CNS, microglia can modulate activity-dependent synaptic transmission, thereby influencing long-term synaptic plasticity that is essential for learning and memory processes (Parkhurst et al. 2013; Wu et al. 2015b). As active phagocytes, microglia are capable of eliminating apoptotic cells, cellular debris and invading pathogens (Rock et al. 2004; Walker et al. 2014; Casano and Peri 2015). Furthermore, microglia are the central communicators between the CNS and immune system. Through upregulation class-II major histocompatibility proteins (MHC-II) on their surface, microglia function as antigen presenting cells to T-cells and can also recruit macrophages from the periphery in response to infections and tissue damage in order to limit inflammation (Rock et al. 2004; Prinz et al. 2011). This diverse engagement of microglia is regulated by extracellular signals that activate microglial receptors and influence their release of trophic factors as well as pro- or anti-inflammatory mediators (von Zahn et al. 1997; Napoli and Neumann 2009; Kettenmann et al. 2011; Sousa et al. 2017). The disruption of physiological functions of microglia is critical for the onset and progression of neurological disorders, such as traumatic brain injury, ischemia and Alzheimer's and Parkinson's disease (Minghetti et al. 2005; Salter and Stevens 2017). Importantly, the prerequisite for specialized microglial functioning is the structural remodelling of their morphology (Walker et al. 2014).

1.2.2.2.1 Microglial morphology and activation

Microglia have a highly dynamic morphology and are not permanently connected to surrounding cells, which enables their rapid structural and functional response to changes in their extracellular milieu (Walker et al. 2014). Under physiological conditions, microglial morphology is characterized by small cell somata with little perinuclear cytoplasm and fine protrusions with extensively ramified processes. In this so-called 'resting' state, microglia are actively surveying their parenchymal microenvironment by extending and

retracting their highly motile processes without disturbing neuronal circuity (Nimmerjahn et al. 2005). In this way, microglia are in intimate contact with nearby neurons, other glial cells and blood vessels and produce various neurotrophic factors, such as brain-derived neurotrophic factor (BDNF), transforming growth factor-β (TGF-β) and nerve growth factor (NGF) to maintain homeostatic balance (Hanisch and Kettenmann 2007; Ransohoff and Perry 2009; Kettenmann et al. 2011). Furthermore, the ramified and anti-inflammatory phenotype of microglia is partially maintained through endogenous signals, such as transcription factors like Runx1 or Irf1 and exogenous signals that include a number of neuron-derived signalling molecules, such as the chemokine fractalkine and the surface molecule CD200 (Biber et al. 2007; Eyo and Wu 2013; Kierdorf and Prinz 2013). These signals constitutively maintain microglia in their resting state and mainly suppress pro-inflammatory activity, but when absent alert microglia for potential danger that can lead to protective or detrimental microglial responses (Biber et al. 2007). Consequently, microglia directly react through reorganization of their morphological structure by sending their processes to the site of interest or by complete relocation (Hanisch and Kettenmann 2007; Walker et al. 2014). Microglia can shift structurally and functionally from a resting to an executive state of activation. This highly regulated and gradual process of microglial activation also involves complex genetic and functional changes and is dependent on the stimulus (Hanisch and Kettenmann 2007; Kettenmann et al. 2011). In the course of the activation process, microglia rapidly reduce and shorten their numerous processes, which is accompanied by an enlargement of their soma. Hence, microglia transform their morphology from a ramified to a rather amoeboid shape, which is required for motility, directed migration and proliferation as well as an increased secretory and phagocytic activity (Town et al. 2005; Hanisch and Kettenmann 2007; Walker et al. 2014). Activated, amoeboid microglia become efficient mobile effector cells that primarily serve host defence and neuroprotection through phagocytosis as well as the release of stimulus-specific signalling molecules. Furthermore, they can rearrange and increase the expression of cell surface receptors (Kettenmann et al. 2011). For example, extracellular adenosine triphosphate (ATP) released upon cell damage is sensed by microglial purinergic receptors and induces microglial chemotaxis and eventually phagocytosis of apoptotic cells (Davalos et al. 2005). Microglia further recognize phosphatidylserine, an aminophospholipid that is externalized to the outer membrane of apoptotic cells assisting their clearance while promoting microglial release of anti-inflammatory cytokines, such as TGF-β (Minghetti et al. 2005; Sierra et al. 2013). Microglia also support neuroprotection by eliminating invading microorganisms via pattern recognition receptors, such as toll-like receptors, which induces phagocytosis and the release of pro-inflammatory mediators like tumour necrosis factor α (TNF-α), reactive oxygen species (ROS) and nitric oxide synthase-2 (Minghetti et al. 2005; Sierra et al. 2013). Although these factors are released to enhance microglial phagocytic activity and to prevent further damage, they may also exert neurotoxic effects. Elevated levels of pro-inflammatory cytokines TNF-α, IL-1β, IL-6 and IL-12 and neurotoxins including the pro-oxidant molecules nitrogen oxide (NO) and ROS have been implicated in the onset and progression of neurodegenerative disorders, such as Alzheimer's disease, Huntington's disease, Parkinson's disease and amyotrophic lateral sclerosis (Minghetti et al. 2005; Lull and Block 2010; Smith et al. 2012; Walker et al. 2014). Here, increased or prolonged microglial activation accompanied by elevated levels of pro-inflammatory molecules proceeds to neuronal degeneration and further leads to progressive neuronal damage and propagation of disease. Microglial response to neuronal damage is termed reactive microgliosis, where microglia remain chronically

activated perpetuating microglial activation and neurotoxicity (Block et al. 2007; Lull and Block 2010). There is a critical balance between defence-orientated functions of activated microglia for neuroprotection and their deleterious contribution in neurodegeneration (Minghetti et al. 2005; Biber et al. 2007; Walter and Neumann 2009; Smith et al. 2012; Salter and Stevens 2017).

1.2.2.3 Primary microglial cell cultures

Cultures of murine or rat primary microglia are predominantly obtained from mixed glial cultures containing both, astrocytes and microglia (Saura et al. 2003; Floden and Combs 2007; Ni and Aschner 2010). Microglia are separated from primary astrocytes by mild agitation or trypsinization. Using the mild agitation method, microglia visible as small round cells are detached from a confluent primary astrocytic layer by shaking and are, subsequently, dispersed in the medium. The microglia-containing medium is then removed and cells can be seeded in separate cell culture plates (Ni and Aschner 2010; Tamashiro et al. 2012). When confluence is reached, primary microglia do not proliferate any longer and show ramified morphologies typical for resting microglia (Ni and Aschner 2010). Using mild trypsinization, astrocytes are detached and removed from confluent microglia (Saura et al. 2003). Both isolation procedures yield high purity of microglial cultures and large amounts of cells that are economical, fast and easy to reproduce (Saura et al. 2003; Ni and Aschner 2010; Tamashiro et al. 2012). Microglial cultures obtained from postnatal animals of the same litter can be investigated under desired treatment conditions and compared with cell preparation replicates (Deierborg 2013). Cultured microglia can be analyzed, for instance, in terms of morphological alteration, including the state of activation and their pro- and anti-inflammatory cytokine secretion profile. In general, primary microglial cultures have been extensively used in pharmacological and biochemical studies to gain insights into their physiology and pathology (de Vellis and Cole 2012).

1.3 Brain cells encountering SPIOs

The ionic microenvironment within the CNS, essential for proper neural signalling, is protected from ions and molecules of the circulating blood by three barriers. These include the BBB formed by specialized endothelial cells, the blood-cerebrospinal fluid barrier formed by epithelial cells of the choroid plexus and the avascular arachnoid barrier formed by the arachnoid epithelium (Abbott et al. 2010). The BBB extents along the brain microvasculature, exhibiting the largest surface area for metabolic exchange. It consists of cerebrovascular endothelial cells connected through tight junctions as well as adherence junctions that restrict paracellular permeability across adjacent cells (Keaney and Campbell 2015). Together with astrocytic end-feet on the abluminal endothelial surface, pericytes and microglia, the BBB forms a dynamic neurovascular unit (Abbott et al. 2010; da Fonseca et al. 2014; Serlin et al. 2015). This unit prevents passive diffusion of hydrophilic molecules and ions from the blood but allows for free diffusion of lipophilic molecules, such as oxygen and carbon dioxide. For regulated entry and exit of metabolites, including glucose and amino acids, the BBB contains specific transcellular transport systems mediated through receptor protein carriers. For a selective uptake of macromolecules, such as hormones and enzymes, receptor-mediated

and adsorptive-mediated endocytosis occurs (Abbott 2002). Hence, the BBB constitutes a highly regulated boundary preserving homeostasis that is essential for a healthy CNS.

Several reports in the literature have shown that nanoparticles can enter the CNS via different routes of exposure, including inhalation, dermal uptake and ingestion (Buzea et al. 2007; Oberdorster et al. 2009; Laux et al. 2018). For instance, intranasally inhaled nanoparticles were found to be transported into the brain by olfactory nerves after being deposited in the olfactory bulb (Wang et al. 2011; Wu et al. 2013b). In case of dermal penetration, incorporation and certainly injection, nanoparticles end up in the blood circulation and are distributed to various organs, such as the liver, spleen and brain (Oberdorster et al. 2005; Buzea et al. 2007; Oberdorster et al. 2009). However, information about interferences with brain function or cytotoxic effects on neural cells associated with nanoparticle exposure has not been comprehensively explored. The reason for concern when using SPIO-based contrast agents is attributable to the fact that intravenously injected SPIOs are capable of easily, however, non-specifically pass cell- and tissue barriers, such as the BBB or blood-placenta barrier (Lockman et al. 2004; Wang et al. 2010; Cartwright et al. 2012; Kong et al. 2012; Hoff et al. 2013; Thomsen et al. 2013; Muller et al. 2018). By virtue of their size and surface chemistry, SPIOs have been shown to decisively influence their passage through the intact BBB (Lockman et al. 2004; Kim et al. 2006; Wang et al. 2010). As the brain endothelium represents an electrostatic barrier through its expression of negatively charged glycocalyx residues, anionic molecules are repelled if they do not target anionic transporters or receptors (Lockman et al. 2004). However, low doses of anionic nanoparticles smaller than 100 nm and cationic molecules, like positively-charged nanoparticles are capable of interacting and locally disrupting the BBB, which was shown using an *in situ* rat brain perfusion model (Lockman et al. 2004). As the endothelium of BBB is almost completely covered by astrocytic end-feet, these cells likely encounter SPIOs first (Geppert et al. 2011; Lamkowsky et al. 2011; Thomsen et al. 2013). Nonetheless, microglia are also frequently found in close proximity to endothelial cells of the brain microvasculature, where their processes wrap and extend along vessels (Walker et al. 2014; Keaney and Campbell 2015). Thus, neurons and glial cells potentially encounter SPIOs following intravenous injection.

SPIO penetration might also be a secondary result of the externally applied magnetic field through which those particles are unintentionally drawn across barriers or cell membranes. That certainly makes it much more difficult to predict consequences of diagnostically and therapeutically applied SPIOs on brain cells and the subsequent effects in the long term. Several publications using cell culture models of the BBB showed that 30 to 40 % of the applied SPIOs can overcome this barrier depending on the external magnetic force or/and surface coating (Dan et al. 2013; Hoff et al. 2013; Thomsen et al. 2013; Sun et al. 2014). Even *in vivo* studies on rodents have shown that 17 to 30 % of intravenously injected SPIOs can cross the intact BBB, whereas a magnetic field significantly increased SPIO penetration (Kong et al. 2012; Dan et al. 2013). Due to subsequent localization of SPIOs within endothelial cells, the mechanism for entry of SPIOs has been postulated to occur via transcellular trafficking (Ragnaill et al. 2011; Kong et al. 2012; Thomsen et al. 2013).

Consequently, penetrating or barrier-disrupting properties of SPIOs as well as their passive diffusion into the brain parenchyma must be investigated thoroughly for individual SPIO types to prevent potential

neurotoxic influences, for instance, by detrimental microglial activation. Available information about SPIO interactions with brain cells is still incomplete and serious concerns about potential toxic effects have been raised (Oberdorster et al. 2009; Hu and Gao 2010; Yang et al. 2010; Cupaioli et al. 2014). Decisive prerequisites have to be fulfilled in order to use SPIO-based contrast agents in clinical practice, which include research strategies with suitable *in vitro* models. An advantageous approach is utilizing primary brain cell cultures instead of immortalized cell lines because many important *in vivo* characteristics are preserved and, therefore, the actual impact of SPIOs on such cells is of greater biological relevance.

1.4 Aim of the thesis

Today, there is still a lack of information concerning the cellular and molecular effects of SPIOs that are applied for clinical diagnostics or those that passed the first clinical trial phases. It is imperative to assess and link specific SPIO properties to potentially adverse particle interactions with brain cells. Therefore, this thesis explores the effects of novel VSOPs in comparison to commercially available ferucarbotran and ferumoxytol on the morphology and vitality of primary cell cultures of microglia and hippocampal neurons. In addition, neuron-glia co-cultures were used to test the impact of SPIOs under conditions that more closely reflect the environment within the brain. The first aim was to explore whether primary microglia and neurons in mono- and co-cultures accumulate SPIOs of varying composition when exposed to doses corresponding to those that are applied in clinical practice. Secondly, cellular morphology was investigated following SPIO exposure for 6 and/or 24 hours because morphological alterations can be used as indicators for adverse consequences. In addition, influences of SPIOs on cell viability and survival was investigated. Finally, cytokine and chemokine secretion profiles of all cell cultures, including astrocyte cultures, were examined to test whether certain types of SPIOs induce the release of pro- or anti-inflammatory mediators and, thereby, affect the communication between glial cells and neurons.

2 Materials and Methods

2.1 Materials

2.1.1 Chemicals and media

Product description	Manufacturer	Article number
2-Mercaptoethanol	Sigma	M7522
B27 Supplement	Life technologies, Gibco	17504-044
Chloroform	Merck Millipore	CAS 67-66-3
DNase I	Roche	11284932001
Dulbecco's Modified Eagle Medium (DMEM)	Life technologies, Gibco	11995065
Effectene transfection reagent	Qiagen	301425
Ethanol (99.8 %)	Carl Roth	K928.4
Fetal calf serum (FCS)	Pan Biotech	3302-P291205
Glucose	Sigma	G7021
High-Capacity cDNA Archive Kit	Applied Biosystems, Carlsbad, CA, USA	4374966
Hank’s buffered salt solution (HBSS-/-: without calcium/ magnesium/ phenol red)	Life technologies, Gibco	14170-088
Hank’s buffered salt solution (HBSS +/+: with calcium/ magnesium/ phenol red)	Life technologies, Gibco	14025-050
Hoechst 10mg/ml	Sigma	94403
Immu-Mount™	Thermo Scientific	9990402
Isopropanol	Sigma	190764
L-Glutamine	Invitrogen	25030-024
Lipopolysaccharide (LPS)	Sigma	L3024
Milk powder	Carl Roth	T145.2
Minimal Essential Medium (MEM)	Life technologies, Gibco	11095-080
Nuclear fast red	Carl Roth	N069.1
Sodium citrate	Carl Roth	3580.1

Sodium dihydrogen phosphate	Merck Millipore	1.06346.1000
Sodium hydroxide	Carl Roth	6771.3
Trypan blue dye	Biochrom	L6323
Neurobasal Medium	Life technologies, Gibco	21103-049
Paraformaldehyde (PFA)	Carl Roth	0335.3
Penicillin/Streptomycin (Pen/Strep), 100 U/ml	Pan-Biotech	P06-07100
Proteome Profiler Mouse Cytokine Array Kit, Panel A	R&D Systems	ARY006
Prussian blue	Sigma	03899
Horse serum	Pan-Biotech	P30-0702
Poly-$_L$-Lysin (PLL, 10 mg/ml)	Sigma	P6407
Propidium iodide	Carl Roth	CN74.2
Triton X-100	Sigma	T8787-100ML
TRIzol™ reagent	Gibco	15596026
Trypsin (2.5 %)	Gibco	15090-046
Trypsin-EDTA (0.25 %)	Gibco	25200056
Xylene	Roth	9713.3

2.1.2 Cell culture media

Cell culture medium	**Composition**
Plating media for primary neurons (MEM+)	430 ml MEM 15 ml Glucose solution, 20 % 50 ml Horse serum 5 ml Pen/Strep, 100x
Growth medium for primary neurons	483,75 ml Neurobasal medium 10 ml B27 Supplement, 50x 1.25 ml L-Glutamine, 200 mM 5 ml Pen/Strep, 100x
Cell culture medium for primary microglia (DMEM+)	444.5 ml DMEM 50 ml FCS, 10 %

	5 ml Pen/Strep, 100x 0.5 ml 2-Mercaptoethanol, 50mM

2.1.3 Buffers and solutions

Solution	**Composition**
Borate buffer	6.18 g Boric acid 1000 ml Millipore type II water
Blocking solution	10 % FCS 0.1 M PBS
Fixative	4 % PFA 15 % Sucrose 0.2 M PB
Permeabilization solution	0.1 % Triton X-100 0.1 % Sodium citrate solution 0.1 M PBS
Phosphate buffer (PB), 0,2 M	28,4 g Sodium dihydrogen phosphate (Na_2HPO_4) 1000 ml Millipore type II water
Phosphate buffered saline (PBS), 0,1 M	268.03 g/mol Sodium dihydrogen phosphate ($Na_2HPO_4*7H_2O$) 137.99 g/mol Sodium dihydrogen phosphate ($Na_2HPO_4*H_2O$) pH 7.4
Poly-L-lysine (PLL), 200 mg/ml	200 µg PLL, 10 mg/ml stock 20 ml 0.1 M borate buffer/ 0.1 M PBS
Propidium Iodide (PI), 5 µg/ml	5 mg PI, 500 µg/ml stock solution 10 ml 0.1 M PBS
Lipopolysaccharide (LPS), 0.1 µg/ml	10 mg/ml LPS stock solution 1 µl in 1 ml DMEM+

2.1.4 List of antibodies

2.1.4.1 Primary antibodies

Antigen	Host	Manufacturer	Article number	Dilution
GFAP	Rabbit	Dako	ASB-OAGA03280	1:1000
SMI-32R	Mouse	Enzo Life Sciences, Inc.	ABS219-0100	1:1000
Tuj1	Mouse	Covance	MMS-435P	1:1000

2.1.4.2 Secondary antibodies

Antigen	Host	Manufacturer	Article number	Dilution
CD11b-FITC	Rat	Miltenyi Biotec	130-081-201	1:200
Alexa Fluor 488	Goat	Life Technologies	A-11029	1:1500
Alexa Fluor 568	Goat	Life Technologies	A-11011	1:1500

2.1.5 Hardware and software

Product description	Manufacturer
ABI PRISM™ 7700 Sequence Detection System	Applied Biosystems
ABI PRISM software	Applied Biosystems
Adobe Photoshop CS3 extended, version 10.0	Adobe Systems
Binocular	Leica
CellSens Dimension Software, version 1.4.1 XV 3.4, build 8624)	Olympus
Digital camera fluorescence microscope Olympus IX81: F-View II Olympus BX51: MagnaFire	Olympus
Fluorescence microscope	Olympus

Olympus IX81	
Olympus BX51	
ECOSYS M3540idn multifunction printer	Kyocera
GraphPad Prism 5.0 software	GraphPad Software, Inc.
ImageJ 1.47v software	Wayne Rasband, National Institutes of Health
Incubators (cell culture)	Binder
MagnaFire software, version 2.1B	Olympus
Microsoft office	Microsoft Corporation
Spectrophotometer Thermo Scientific* Biomate 3	Fisher Scientific
Thermo cycler	Biorad
Thermo shaker	Eppendorf, Thermomixxer
Centrifuge	Eppendorf

2.1.6 Equipment

Product description	**Manufacturer**
Cell culture flasks, 75 cm^2	Corning
Dissecting set	Fine Science Tools
Falcon™ Conical Centrifuge Tubes	Fisher Scientific
Glass coverslips	Menzel-Gläser
Glass Pasteur pipettes	Hirschmann Laborgeräte
Microscope slides	Corning
Neubauer counting chamber	Sigma
Petri dishes	Eppendorf
Pipettes	Eppendorf

Pipette tips	Eppendorf
Platform shaker	Heidolph Polymax 2040
Vortex shaker	Janke & Kunkel, AL.16.P.0.10942
Falcon™ Polystyrene Microplates (well plates)	Fisher Scientific

2.1.7 Iron oxide nanoparticles

Very small superparamagnetic iron oxide particles (VSOPs) were synthesized by the Charité Institute of Radiology, and consist of monocrystalline iron oxide cores of magnetite (Fe_3O_4) and maghemite (γ-Fe_2O_3) coated with a monomeric citrate layer. Two types of VSOPs were applied: VSOP-R1, with a diameter of 6.5 nm to 7.5 nm, comparable to commercially available VSOP-C184, and VSOP-R2, with a diameter of 7.5 nm to 8.7 nm, comparable to commercially available VSOP-C200 (Stroh et al. 2006; Tysiak et al. 2009; Wagner et al. 2011; Wuerfel et al. 2011; Millward et al. 2013). These VSOPs have already been tested in human clinical trials up to Phase II (Taupitz et al. 2004; Wagner et al. 2011). For synthesis, 14 g ferrous chloride tetrahydrate and 28 g ferric chloride hexahydrate were dissolved in 0.4 M hydrochloric acid and then mixed with 310 ml 1.5 M sodium hydroxide. This mixture was stirred for 30 minutes, and then 22 g (for VSOP-R1) or 18 g (for VSOP-R2) citric acid monohydrate was added. After a further 30 minutes stirring at 75°C, the mixture was cooled to RT and magnetically separated. Supernatant was withdrawn and sediment resuspended in Milli-Q® water, acidified with monosodium citrate (< pH 5), and then ultrafiltrated (30 kD). Iron concentration was adjusted to 0.5 M, and the final batch was heat-sterilized for 10 minutes at 100°C, resulting in a stable dispersion containing 60 g/L mannitol (Neubert et al. 2015). The VSOPs were about three times smaller than the ultrasmall particles described in the following.

The ultrasmall SPIOs used were ferucarbotran (Resovist®; Bayer Schering Pharma, Germany) and ferumoxytol (Feraheme®; AMAG Pharmaceuticals, USA). Detailed information regarding the synthesis and characterization of ferucarbotran is described by Reimer and Balzer (Reimer and Balzer 2003) and of ferumoxytol by Balakrishnan et al (Balakrishnan et al. 2009). Briefly, ferucarbotran is a carboxydextran-coated SPIO (27–35 mg/ml with an iron-to-carboxydextran ratio of 1:1) composed of approximately 0.5 mol Fe/l, including 40 mg/ml mannitol and 2 mg/ml lactic acid, adjusted to a pH of 6.5. The overall hydrodynamic diameter of ferucarbotran is around 60 nm. Iron oxide cores of ferumoxytol are coated with carboxymethyldextran (polyglucose sorbitol carboxymethyl ether), exhibiting an overall hydrodynamic diameter of 30 nm (Neubert et al. 2015). An overview of the physicochemical properties of SPIOs used in this study given in Table 2.

Table 2: Physicochemical properties of applied SPIOs.

Physicochemical properties	VSOP-R1	VSOP-R2	Ferucarbotran	Ferumoxytol
Surface coating	Citrate	Citrate	Carboxydextran	Carboxymethyl-dextran
Surface charge	Anionic	Anionic	Anionic	Neutral
Iron (Fe) content	26.4 g Fe/l (0.473 M)	27.2 g Fe/l (0.487 M)	25.5 g Fe/L (0.457 M)	29.99 g Fe/L (0.537 M)
Iron oxide core size	4 nm	4 – 5 nm	4.2 nm	6 – 7 nm
Hydrodynamic diameter	6.5 – 7.5 nm	7.5 – 8.7 nm	62 nm	28 – 32 nm

2.1.8 Laboratory animals

All mouse experimental procedures were carried out in accordance with the German Animal Welfare Act and European guidelines (2010/63/EU) for the use of laboratory animals, and were approved by the local regulatory authority of Berlin (Landesamt für Gesundheit und Soziales, LAGeSo: T0095/11). Pregnant and postnatal C57BL/6 mice were obtained from our central animal facility and kept under standard laboratory conditions (12 hour light/dark cycle, 55 % ± 15 % humidity, 22°C ± 1.5°C room temperature, and water *ad libitum*; enriched and grouped).

2.2 Methods

2.2.1 Primary glial cell cultures

Prior to all cell preparations, glass coverslips for facilitating cellular adhesion were washed twice in distilled water and for one hour in 70 % ethanol. Coverslips were stored in 100 % ethanol and breamed. Culture flasks in sizes of 75 cm^2 as well as 12-well plates and glass coverslips were coated with 200 µg/ml poly-L-lysine (PLL; Sigma) overnight at 37°C and washed twice with sterile distilled water on the following day.

Primary microglia were isolated from C57BL/6 mice at P0 - P2. After decapitation, brains were removed and collected in cold HBSS+/+ (Gibco). The medulla oblongata, the pia mater and arachnoid meninges were thoroughly removed; hemispheres were separated from each other and the cerebellum and collected in 15 ml cell culture tubes to numbers of maximum 10 brain pieces per tube. HBSS+/+ was carefully removed, brain tissue was washed once with cold HBSS-/- (Gibco) and incubated with 1 ml of 0.25 % trypsin-EDTA (Gibco) at 37°C for 12 min. Trypsinization was stopped by adding pre-heated DMEM+ (4.5 g/l glucose, 200 mM L-glutamine, pyruvate) containing 10 % FCS, 1 % Pen/Strep und 0.1 % of 50 mM 2-Mercaptoethanol. After the tissue settled down to the tube bottom, 4 ml DMEM+ and 20 µl DNase I (10 mg/ml; Roche) was added, respectively. Subsequent to careful homogenization using a 10 ml pipette, 10 ml DMEM+ was added and the cell suspension was centrifuged for 1 min at 20 *x* g to eliminate non-

dissociated tissue. Supernatants were transferred to new tubes and centrifuged for 5 min at 300 *x* g. The cell pellet was resuspended in 2 ml DMEM+ and further diluted to be plated in PLL pre-coated 75 cm^2 cell culture flasks in densities of 1 x 10^6 cells in 8 ml, respectively. After 24 hours culture media was completely replaced by pre-heated DMEM+. The plated cell population consisting of microglia and astrocytes was kept in culture at 37°C and 5 % CO_2 in culture for 8 to 10 DIV until microglia detached from the feeder layer of confluent astrocytes.

Primary microglia were harvested by gentle agitation of the culture flasks. Cell suspension containing free-floating microglia was removed, centrifuged for 5 min at 300 *x* g and the cell pellet was resuspended in pre-heated DMEM+. Cell numbers were determined in a Neubauer counting chamber (Sigma) using trypan blue (Biochrom) exclusion staining to control microglial vitality. Primary microglia were seeded at densities of 2 × 10^5 cells per well in 1 ml DMEM+ in PLL-coated 12-well plates containing coverslips and maintained at 37°C and 5 % CO_2 for 24 hours prior to the start of experiments.

Primary astrocytes for neuron-glia co-cultures were prepared from C57BL/6 mice at P0 - P2 as described above. For trypsinization, 2 ml of 2.5 % trypsin (Gibco) and 200 µl DNase (10 mg/ml) was used and the tissue was incubated for 5 min at 37°C. Cells were dissociated with a 10 ml pipette, incubated for 10 min at 37°C and once again dissociated using a 5 ml pipette. Cells were resuspended in MEM+ plating medium and centrifuged for 5 min at 300 *x* g. The cell pellet was resuspended with a 2 ml pipette in MEM+ and the number of cells was determined using trypan blue dye in a Neubauer counting chamber (Sigma). Primary astrocytes were seeded in densities of 5 × 10^4 cells per well in PLL-coated six-well plates and maintained for 11 DIV until primary hippocampal neurons on PLL-coated coverslips were transferred to establish neuron-glia co-cultures.

2.2.2 Primary hippocampal neuronal cultures and neuron-glia co-cultures

Primary hippocampal neurons for monocultures and neuron-glia co-cultures were prepared from C57BL/6 mice at E18. Pregnant females were sacrificed by cervical dislocation and uteri were transferred to petri dishes containing cold HBSS+/+. Embryonic brains were collected in cold HBSS+/+; the hippocampi of both hemispheres were carefully isolated and meninges thoroughly removed. Hippocampi were washed two times with HBSS-/- and enzymatically digested using 2.5 % trypsin in HBSS-/- at 37°C for 15 min. Trypsinization was blocked with 3 ml plating medium (MEM+). After adding 10 µl DNase I (10 mg/ml), the tissue was mechanically homogenized with a fire-polished Pasteur pipette. Following dissociation, the supernatant was transferred to a new tube and cells numbers were determined using a Neubauer counting chamber. Primary hippocampal neurons were plated in plating medium onto PLL-coated glass coverslips in 12-well plates with densities of 8 × 10^4 cells per well. After three hours of plating at 37°C and 5 % CO_2, neurons were washed twice with sterile 0.1 M PBS and cultivated in 1 ml Neurobasal medium supplemented with 2 % B27, 0.5 mM L-glutamine and 100 U/ml penicillin, 100 µg/ml streptomycin at 37°C and 5 % CO_2, respectively. Neurons were maintained at 37°C and 5 % CO_2 for 10 DIV prior the start of experiments.
For neuron–glia co-cultures, primary neurons on glass coverslips were transferred to astrocyte cultures on the day of preparation by placing them upside down on the plated astrocytes. After 7 DIV, one third of the media was replaced and neurons were maintained in co-culture for 10 DIV.

2.2.3 Transfection of primary neurons

For ease of morphological analysis, primary neurons in mono- and co-cultures were transfected with enhanced green fluorescent protein (eGFP) (Invitrogen, Germany) 24 hour prior to SPIO exposure at 8 DIV. To introduce eGFP plasmid DNA into neuronal DNA, I applied Effectene Transfection Reagent (Qiagen) in conjunction with a special enhancer. The enhancer condensates the DNA, which is then coated with cationic lipids by the Effectene Reagent and subsequently incorporated by neurons. After incubation for 1 hour at 37°C in 5 % CO_2, the reagent was removed, cells were washed with sterile 0.1 M PBS, and 1 ml fresh growth medium was added to each well. Neurons were kept at 37°C in 5 % CO_2 for 24 hours prior the start of SPIO exposure.

2.2.4 Quantitative real-time PCR of neuron-glia co-cultures

Identity and purity of primary cells in co-cultures were analysed by quantitative real-time (qRT-) polymerase chain reaction (PCR) that allows for quantitative analysis of relative gene expression levels (Jozefczuk and Adjaye 2011). In qRT-PCR, neuron-specific class III β-tubulin (Tuj1) determining neuronal origin, glial fibrillary acidic protein (GFAP) as a marker for astrocytes, and the ionized calcium-binding adaptor molecule 1 (Iba1) as a marker for microglial cells were used. For RNA isolation, 3 ml of TRIzol™ reagent (Gibco) was added to neuron-glia co-cultures and incubated on a rocking platform shaker (Heidolph Polymax 2040) for 5 min at RT. Primary cells were scraped in 1 M PBS and transferred into Falcon™ Conical Centrifuge Tubes (Fisher Scientific). After adding 0.2 ml chloroform per 1 ml TRIzol™ reagent, the homogenate was incubated for 2 to 3 min at RT and centrifuged at 12000 *x* g for 15 min at 4°C. After centrifugation, three layers form, whereby the upper aqueous solution containing RNA was transferred to a new Falcon™ tube. For RNA precipitation, 0.5 ml isopropanol per 1 ml TRIzol™ reagent was added, incubated for 10 min at RT and centrifuged at 12000 *x* g for 10 min at 4°C. The supernatant was discarded, the pellet washed with 1 ml of 75 % ethanol per 1 ml TRIzol™ reagent for lysis. Subsequently, the pellet was vortexed briefly and centrifuged at 7500 *x* g for 5 min at 4°C. The resulting pellet was dried for 5 to 10 min, resuspended in 100 µl of Millipore type II water to solubilize the RNA and immediately put on ice. Concentration and purity measurement of the total RNA isolated was determined by spectrophotometric analysis (Thermo Scientific* Biomate 3 spectrophotometer, Fisher Scientific). For cDNA synthesis, the High-Capacity cDNA Archive Kit (Applied Biosystems) was used, containing components for reverse transcription of total RNA to single-stranded cDNA. A master mix was prepared, containing 5 µg total RNA, 10X Reverse Transcription Buffer, 25X deoxynucleotides, 10X primers and adjusted with Millipore type II water to a final volume of 50 µl. Subsequently, the mix was pipetted into a 96-well plate. As control condition, the reaction was performed without MultiScribe Reverse Transcriptase (50 U/µl). The thermal cycler was programmed for the first step 10 min at 25°C and a second step for 120 min at 37°C. The quality of the amplified cDNA (with and without MultiScribe reverse transcriptase) was controlled by β-actin PCR. cDNA was diluted 1:5 with RNase, DNase-free water and stored at −20°C. Reverse transcriptase qRT-PCR was performed with the following gene expression assays: Tuj1 (assay ID Mm00727586_s1), Iba1 (assay ID Mm00479862_g1), GFAP (assay ID Mm00546086_m1), glycerinaldehyd-3-phosphat-Dehydrogenase (GAPDH) (assay ID 4352932E) and β-actin (assay ID 4352933E) (Applied Biosystems). For HPRT, separate primer and probe

were used (Primer Mix for 5′-ATCATTATGCCGAGGATTTGGAA-3′; rev 5′-TTGAGCACACAGAGGGCCA-3′ and probe 5′-TGGACAGGACTGAAAGACTTGCTCGAGATG-3′). The PCR was run on the ABI PRISM™ 7700 Sequence Detection System (Applied Biosystems) and data obtained were processed by ABI PRISM software. Standard curves were created by serial dilutions of cDNA from P10 mouse cortex with amplification efficiency between 90 % and 100 %. Data were normalized to two different house-keeping genes (β-actin and HTPR), producing similar results. Each result is the average of three separate experiments (Neubert et al. 2015).

2.2.5 Conditions of SPIO exposure in cell cultures

VSOP-R1, VSOP-R2, ferucarbotran, or ferumoxytol were added to 12 well plates of primary microglia, primary hippocampal neurons, and neuron-glia co-cultures in 1 ml culture medium per well, yielding final iron concentrations of 0.5 mM, 1.5 mM, or 3.0 mM, respectively. Accordingly, primary cells were exposed to SPIO concentrations as listed in Table 3.

Table 3: Iron concentration of applied SPIOs.

	VSOP-R1	**VSOP-R2**	**Ferucarbotran**	**Ferumoxytol**
Iron (Fe) content	26.4 g Fe/l (0.473 M)	27.2 g Fe/l (0.487 M)	25.5 g Fe/L (0.457 M)	29.99 g Fe/L (0.537 M)
0.5 mM	27.91 mg Fe/mL	27.93 mg Fe/mL	27.9 mg Fe/mL	27.92 mg Fe/mL
1.5 mM	83.73 mg Fe/mL	83.79 mg Fe/mL	83.67 mg Fe/mL	83.77 mg Fe/mL
3.0 mM	167.46 mg Fe/mL	167.58 mg Fe/mL	167.34 mg Fe/mL	167.54 mg Fe/mL

Microglial cells were incubated with SPIOs at 8 to 9 DIV for 6 hours or 24 hours, respectively. Primary neurons and neuron–glia co-cultures were incubated for 24 hours at 9 DIV. Well plates of all cell culture models included wells with respective numbers of cells that were not treated with SPIOs serving as control condition (indicated in figures and tables as control). In primary microglial cultures, well plates additionally contained wells of cells that were stimulated with 0.1 µg/ml lipopolysaccharide (LPS, Sigma) and served as control condition for the activation state of microglia.

2.2.6 Determination of microglial viability using propidium iodide

The viability of primary microglia was assessed using propidium iodide (PI) staining (Carl Roth, Germany). Following SPIO exposure, primary microglia in densities of 2×10^5 cells per well were incubated with 500 µg/ml PI for 15 min at 37°C. An inverted fluorescence microscope (objective UPLFLN 10×/0.30 PH1; Olympus IX81) was used to capture the fluorescent emission of PI at 630 nm with an F-View II digital camera using CellSens Dimension software (version 1.4.1 XV 3.4, build 8624; Olympus, Germany). Four images per exposure condition, including positive and negative controls, were acquired from four different

regions of the respective wells. The number of PI-positive microglia was quantified using the Image-Based Tool for Counting Nuclei plug-in in ImageJ 1.47v software (National Institutes of Health, USA). From four corresponding images, PI values were averaged, values of negative controls were subtracted, and results were normalized to PI values of positive controls. In total, 1630 images of PI-positive microglia were analysed. PI-staining and fluorescence measurements for the 6-hour exposure condition were performed on five independently prepared primary microglial cultures and for the 24-hour condition on seven independently prepared microglial cultures (Table 4).

2.2.7 Prussian blue staining and nuclear fast red counterstain

To cytochemically detect iron accumulation by microglia and neurons from monocultures following SPIO exposure, Prussian blue staining using the colorimetric ferrozine Perl's stain method (Perl and Good 1992) was performed. Microglia were stained with Prussian blue reagent following the previously described PI measurements. Supernatants of microglial cultures and neuronal monocultures were removed, cells were washed twice with PBS and immediately fixed with 4% PFA (Carl Roth) in 15 % sucrose for 15 min at 4°C. After removing fixation solution, cells were hydrated in distilled water for 5 min and incubated with equal amounts of 1 % potassium ferrocyanide and 1 % hydrochloric acid for 30 min. To visualize cell nuclei, cells were washed with distilled water and incubated for 10 min with 0.1 % nuclear fast red counterstaining solution that produces an intense pink nuclear stain and slight pink colouring of the cytoplasm. Subsequently, cells were dehydrated with increasing alcohol concentrations ranging from 70 to 100 % before mounting coverslips on glass slides using xylene.

2.2.8 Iron quantification of microglia

For each exposure condition, images from six different regions of Prussian blue and nuclear fast red stained coverslips of primary microglia were captured with 40x magnification (LUCPLFLN 40x/0.60 PH2) using light microscopy (Olympus IX81) and saved in TIFF format. In order to eliminate colour-biased values, images were acquired with 256 colours in grey scale. The presence of iron in respective greyscale images was quantified using ImageJ 1.47v software. The mean grey-value intensities of four cells from six corresponding images were measured by defining regions of interest. Additionally, mean grey-value intensities of the image background in corresponding images, as well as values of negative controls, were averaged and subtracted from the averaged values of cells. Prussian blue staining and subsequent quantification of cellular iron content for the 6- and 24-hour exposure conditions were performed on six independently prepared primary microglial cultures (Table 4). In total, 24 microglial cells per SPIO-exposure condition were quantified and mean grey-value intensities of corresponding cells were averaged. In total, 1752 images of Prussian blue stained microglia were analysed.

2.2.9 Immunostaining and microscopy

2.2.9.1 Immunocytochemistry of microglia

Following SPIO incubation, supernatants were removed and cells were washed twice with 0.1 M PBS. After fixation with 4% PFA in 15 % sucrose for 15 min at 4°C, microglia were washed twice with 0.1 M PBS, permeabilized using 0.1 % Triton X-100, 0.1 % sodium citrate in PBS for 3 min at 4°C, and washed again three times with 0.1 M PBS. Cells were blocked over night with 5 % FCS and 0.1 M PBS at 4°C. On the following day, microglia were immunocytochemically stained using cell-specific CD11b-fluorescein isothiocyanate (CD11b-FITC)-conjugated antibody (Miltenyi Biotec, Germany) in 5 % FCS and 0.1 M PBS for 90 min in the dark at RT. After removing the antibody solution, cells were washed three times with PBS. Cell nuclei were counterstained using the blue fluorescence nucleic acid stain Hoechst 33258 (Sigma-Aldrich) and cell-containing coverslips were mounted using Immu-Mount™ (Thermo Scientific, Germany).

2.2.9.1.1 Immunofluorescence image acquisition and processing

Immunofluorescence images of microglia were captured with an Olympus BX 51 microscope with narrow-band filters (Olympus) using a MagnaFire digital camera and MagnaFire 2.1B software (Intas, Germany). Additionally, light microscopy was used to capture images of cell-associated SPIOs due to unfeasible combination of Prussian blue with immunocytochemical staining (Frank et al. 2007). As the iron oxide cores of SPIOs consist of ferric (Fe^{3+}) iron, particles appear in brown colour (Sadrzadeh and Saffari 2004). Light microscope photographs were processed using Adobe Photoshop (CS3 extended, version 10.0; Adobe Systems) in order to create merged images of cell-associated SPIOs with corresponding immunofluorescence images of primary microglia. Therefore, bright field images of SPIOs were first inverted and pseudo-coloured in red by using the channel mixer tool, setting all colours to zero percent and only red to 100 %. To generate overlay images of microglia depicted in green with nuclei depicted in blue and SPIOs depicted in red, I created a triple layer image and excluded either the green, blue or red channel in each layer, depending on the respective layer order. For example, the background layer is the one showing blue nuclei, one level above, hence, superior ranked is the image of green microglia and the upper level is the image of red SPIOs. In each layer, the colour channel of the antecedent image was excluded making all images with respective colours visible at once.

2.2.9.2 Immunocytochemistry of neuronal cultures

Following SPIO exposure of transfected primary neurons from mono- and co-cultures, supernatants were collected, centrifuged at 16000 *x* g and stored for cytokine/chemokine measurements at -20°C. Coverslips of co-culture neurons were transferred to new 12-well plates. Cells were washed twice with 0.1 M PBS and immediately fixed with 4 % PFA in 15 % sucrose for 15 min at 4°C. After removing the fixation solution, neurons were washed twice with 0.1 M PBS and permeabilized with 0.1 % Triton X-100 and 0.1 % sodium citrate in 0.1 M PBS for 3 min at 4°C. Neurons were washed with 0.1 M PBS three times, blocked with 10 % FCS for 1 hour at RT and incubated with neuron-specific class III β-tubulin antibody Tuj1 (Covance) in 10 % FCS in 0.1 M PBS overnight at RT. Neurons from monocultures were also immunocytochemically stained using SMI-32R antibody (Enzo Life Sciences, Inc.) in a dilution of 1:1000 in 5 % FCS and 0.1 M PBS and

incubated overnight at RT. Secondary antibody Alexa Fluor 488 goat anti-mouse (Life Technologies) was diluted 1:1500 in 5 % FCS and 0.1 M PBS. Neurons cells were incubated for 90 min at RT and washed three times with 0.1 M PBS prior mounting coverslips with Immu-Mount™ (Thermo Scientific).

2.2.10 Image acquisition and Sholl analysis of primary hippocampal neurons

The number of neurites of primary neurons from mono- and co-cultures was determined by means of Sholl analysis (Sholl 1953). Images of double-positive, i.e., with enhanced green fluorescent protein (eGFP) and red fluorescent Tuj1 stained neurons were acquired with fluorescence microscopy equipped with CellSens Dimension software and a 10x objective (Olympus IX81). Using Adobe Photoshop C5, images displaying different image frames of individual neurons were matched to create an image of the entire cell. The composite images were used to quantify the number of neurites of per exposure condition on 24 20 µm-spaced concentric circles with maximal distances of 500 µm distal to the cell body. The innermost circle with a radius of 40 µm was placed onto each neuron, with its centre coinciding with the centre of the soma. The number of neurite intersections at each circle were counted blindly using ImageJ 1.47v software. The intersection curve was plotted by the average number of neurite intersections for each circle versus the circle radius using GraphPad Prism 5.0 software (GraphPad Software). Sholl analysis of neurons was performed via double determination of three independently prepared primary neuron monocultures and four independently prepared neuron-glia co-cultures for each exposure condition (Table 7 and 8, respectively). In total, 750 neurons from monocultures and 223 neurons from co-cultures were analysed using Sholl analysis. Neurons were excluded in the analysis in cases of undefined origin of neuronal processes or in cases of neurite overlapping.

2.2.11 Degeneration analysis of primary hippocampal neurons

To determine if SPIOs lead to neuronal degeneration and subsequent cell death, eGFP-transfected Tuj1-positive neurons of mono- and co-cultures were manually counted under a fluorescence microscope (Olympus IX81; objective 10x). Numbers of degenerated neurons were calculated as percentages of total numbers of neurons. Neurons were classified as degenerated according to standard morphological criteria, i.e., fragmentation of neuronal processes, cell shrinkage, and somatic swelling (Adamec et al. 2001). Quantification of neurons was performed via double determination of three independently prepared primary neuron monocultures and four independently prepared neuron–glia co-cultures for each exposure condition.

2.2.12 Cytokine and chemokine measurement

To investigate cytokines and chemokines secretion of primary cell cultures of microglia, astrocytes and neurons from mono- and co-cultures supernatants of cultures incubated for 24 hours with 0.5 mM of VSOPs, ferucarbotran and ferumoxytol were used. Supernatants of untreated cells from respective cultures served as control condition and were always included for each measurement. Following SPIO exposure, supernatants were collected and centrifuged at 4°C with 16000 *x* g for 20 min to remove cellular debris.

The resulting supernatants were transferred into Eppendorf tubes and analysed for 40 different cytokines and chemokines using the Proteome Profiler Mouse Array Kit, Panel A (R&D Systems). Each kit contains four nitrocellulose membranes, where respective capture antibodies are spotted in duplicate. Membranes were incubated with 2 ml of the supplied blocking buffer (Array Buffer 6) on a rocking platform shaker (Heidolph Polymax 2040) for 1 h at RT. Meanwhile, 1 ml of respective cell culture supernatants was mixed with 0.5 ml of Array Buffer 4 and adjusted to a final volume of 1.5 ml with blocking buffer as necessary. To each sample, 15 µl of Mouse Cytokine Array Panel A Detection Antibody Cocktail (biotinylated antibody cocktail) was added and incubated for 1 hour at RT. After removing Array Buffer 6, the prepared samples were added to nitrocellulose membranes, respectively, and incubated on a rocking platform shaker over night at 4°C, so that the detection antibody complex is bound by capture antibodies on the membranes. On the next day, membranes were placed into individual petri dishes and washed three times with 20 ml of 1x Wash Buffer on a rocking platform shaker. After washing, the supplied horseradish peroxidase-conjugated streptavidin was diluted in blocking buffer and each membrane was incubated with 2 ml for 30 min on a rocking platform shaker at RT. Subsequently, membranes were placed in individual containers, washed three times and transferred onto plastic sheets. Signal development was achieved by incubating each membrane with 1 ml of the provided chemiluminescence detection reagent for 1 min. Membranes were then covered by an additional plastic sheet and placed into an autoradiography film cassette. Autoradiography films were exposed for multiple times points for signal detection and subsequent quantification. In total, 16 kits containing 64 nitrocellulose membranes of the Proteome Profiler Mouse Array Kit, Panel A (R&D Systems) were used for analyses. Experiments were performed in triplicate with supernatants from all exposure conditions and cell cultures, respectively.

2.2.12.1 Cytokine and chemokine quantification

Nitrocellulose membranes were scanned in a resolution of 600 x 600 dpi and converted to TIFF format using the ECOSYS M3540idn multifunction printer (Kyocera) for each experimental condition, respectively. The mean grey-value intensities of respective duplicate spots in each image were quantified by defining regions of interest with ImageJ 1.47v software. Additionally, mean grey-value intensities of the image background and of the three reference spots in duplicate of corresponding images were quantified. Subsequently, averaged mean grey-value intensities of the image background were subtracted from the measured mean grey-value intensities of duplicate spots as well as reference points using Microsoft Excel (Microsoft Corporation). Values of averaged duplicate spots were normalized to averaged values of corresponding reference spots in the image and then normalized to averaged values of untreated controls, respectively. Statistical analysis was performed using GraphPad Prism 5 software.

2.2.13 Statistics

All data were collected using Microsoft Excel (Microsoft Corporation) following measurements. Statistical significance was evaluated with the assistance of GraphPad Prism 5.0 software using Kruskal–Wallis one-way analysis of variance (ANOVA) followed by Dunn's multiple comparison *post hoc* test, at indicated significance levels. Data are presented as means ± standard error of the mean (SEM).

3 Results

3.1 SPIOs affect the morphology and viability of primary microglia

3.1.1 Microglia accumulate SPIOs dependent on size and surface coating

The first question I addressed was whether novel VSOPs and commercially ferucarbotran and ferumoxytol are accumulated by primary microglia when applied in iron concentrations corresponding to clinical doses of 0.5 mM, 1.5 mM or 3.0 mM, respectively. For this purpose, I visualized microglia-associated SPIOs with very sensitive Prussian blue staining to cytochemically detect iron oxide; such staining is commonly used to identify SPIOs in cells and tissues (Cengelli et al. 2006; Tysiak et al. 2009; Andreas et al. 2012; Wagner et al. 2013; Jarockyte et al. 2016). During the reaction, even the smallest amounts of ferric iron chemically react with ferrocyanide to create a bright blue pigment, called ferric ferrocyanide or Prussian blue (Perl and Good 1992; Jarockyte et al. 2016). Subsequent to Prussian blue staining, I used nuclear fast red dye chromogenic counterstain in order to localize SPIO accumulation by microglial cells. The nuclear fast red dye visualized cell nuclei in intense pink and the cytoplasm in moderate pink colour (Cengelli et al. 2006; Pinkernelle et al. 2012). This allowed for visual examination of microglia-associated SPIOs using light microscopy. For reasons of comparison, representative images of microglia incubated for 24 hours with the lowest SPIO iron concentration of 0.5 mM and the highest concentration of 3.0 mM are shown (Figure 2).

In general, image evaluation revealed that microglia exposed to VSOP-R1, VSOP-R2, and ferucarbotran but not ferumoxytol consistently showed intense Prussian blue staining (Neubert et al. 2015). Compared with the lowest iron concentration of 0.5 mM VSOP-R1, VSOP-R2, and ferucarbotran, particularly incubation with the highest concentration of 3.0 mM of these SPIOs for 24 hours, resulted in intense Prussian blue-positive deposits indicating increased particle accumulation (Figure 2). In contrast, microglia exposed to ferumoxytol in concentrations of 0.5 and 3.0 mM for 24 hours showed less Prussian blue-detectable iron and, hence, a lower degree of particle accumulation (Figure 2) (Neubert et al. 2015). Upon SPIO accumulation, microglia were almost exclusively of amoeboid shape, compared to untreated microglia that showed ramified morphologies characteristic of the resting state (Figure 2). These morphological changes upon SPIO accumulation, from a ramified towards an amoeboid shape accompanied by expanded somata can be taken as a reliable indicator of microglial activation (Napoli and Neumann 2009; Ransohoff and Perry 2009; Walker et al. 2014). Consequently, citrate-coated VSOPs with hydrodynamic diameters of approximately 6 to 8 nm and the largest, carboxydextran-coated nanoparticle ferucarbotran of around 60 nm were not only strongly accumulated by microglia but also induced morphological alteration. Both types of nanoparticles possess negative surface charges. In contrast, carboxymethyldextran-coated ferumoxytol of 30 nm and neutral surface charge was only moderately accumulated by primary microglial cells. These results indicate, that SPIOs are differently accumulated by microglia, which is dependent on particle size, surface coating material and surface charge.

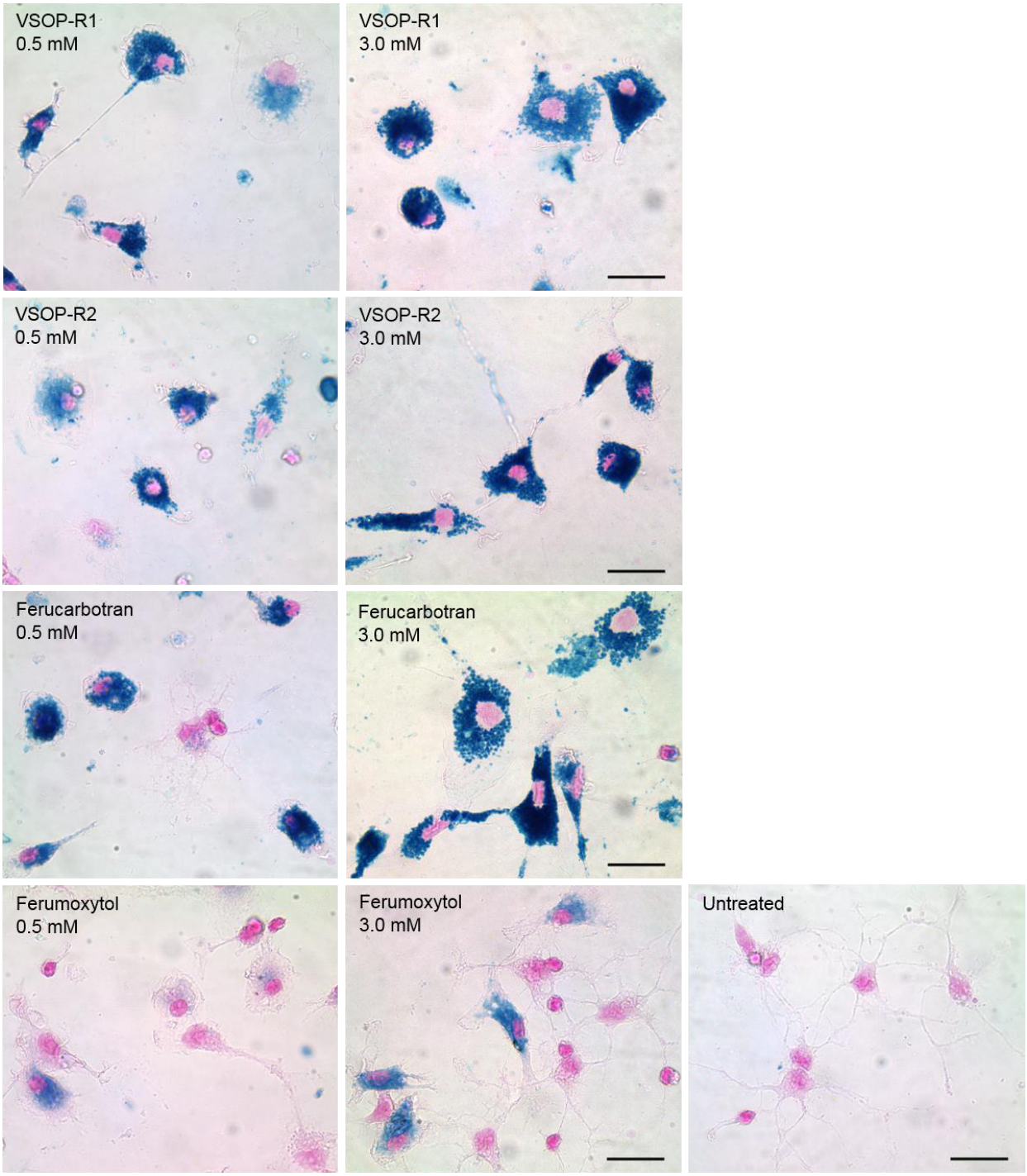

Figure 2: Microglial SPIO accumulation is dependent on the particle type. Prussian blue staining and nuclear fast red counterstain of microglia exposed to 0.5 mM or 3.0 mM of VSOP-R1, VSOP-R2, ferucarbotran or ferumoxytol for 24 hours, or untreated microglia, as indicated. Accumulation of VSOP-R1, VSOP-R2 and ferucarbotran are elevated at highest iron concentrations. In contrast, microglia exposed to ferumoxytol show less intense Prussian blue staining that only slightly increased after exposure to 3.0 mM of ferumoxytol. Upon SPIO accumulation, microglia show morphological transformation from ramified towards amoeboid-like phenotypes as well as expanded somata. In comparison, untreated cultured microglia show ramified morphologies. Scale 20 µm

3.1.2 SPIO accumulation induces alterations of microglial morphology

To further verify morphological transformation of microglia towards a deramified phenotype following SPIO accumulation, I performed immunocytochemical staining using CD11b-FITC-conjugated antibody followed by the nucleic acid counterstain Hoechst 33258 (Neubert et al. 2015). The surface marker CD11b (cluster of differentiation molecule 11b), also called Mac-1 (macrophage-1 antigen) in mice is a constitutively expressed on microglia and upregulated following microglial activation (Ladeby et al. 2005; Korzhevskii and Kirik 2016). For visual comparison of microglial morphology, cells received either no treatment or stimulation with 0.1 µg/ml LPS. The *Escherichia coli* endotoxin LPS is a well-known immunostimulant substance that induces microglial activation accompanied by cytoskeletal reorganisation and morphological transformation (Zielasek and Hartung 1996).

Unfortunately, Prussian blue staining for SPIO detection and immunocytochemistry of microglia could not be performed simultaneously due to the fluorescence absorption capacity of ferric ferrocyanide that leads to colour transformation of immunofluorescence (Frank et al. 2007). Consequently, I used light microscopy to capture images of cell-associated SPIOs with bright field microscopy of the same microscopic image frame. In bright field microscopy, SPIOs are visible in brown colour due to their composition of ferric (Fe^{3+}) iron oxide cores that are naturally pigmented in brown (Figure 3A.1) (Sadrzadeh and Saffari 2004). Therefore, I pseudo-coloured bright field images of brown appearing particles in red (Figure 3A.2) using Adobe Photoshop CS5 software and created overlay images of SPIOs and corresponding immunocytochemically stained microglia (Figure 3A.3). This approach of capturing, firstly, fluorescence images of CD11b-FITC stained microglia and, secondly, bright field images depicting SPIOs enabled colocalization of cells and particles (Neubert et al. 2015). For illustrative comparison, bright field images of SPIOs and the corresponding merged images of CD11b-FITC-positive microglia are only shown for cells incubated for 24 hours in Figure 4. Here, VSOP-R2 is shown as representative for the citrate-coated particle type.

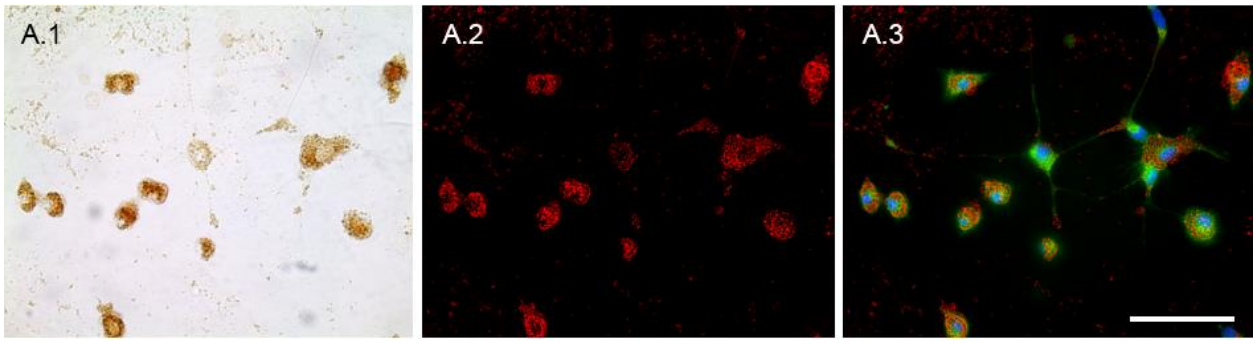

Figure 3: Representative illustration of the process creating merged images of SPIOs and primary microglia from one microscopic image frame. Primary microglia were exposed to 1.5 mM VSOP-R2 for 24 hours and immunocytochemically stained using CD11b-FITC conjugated antibody. (A.1) The bright field image shows VSOP-R2 visible in brown colour without additional staining. (A.2) The same image frame was processed using Adobe Photoshop CS3 extended (version 10.0) for pseudo-colouring nanoparticles in red and creating (A.3) a merged image of VSOP-R2 together with immunostained microglial cells. Scale 40 µm

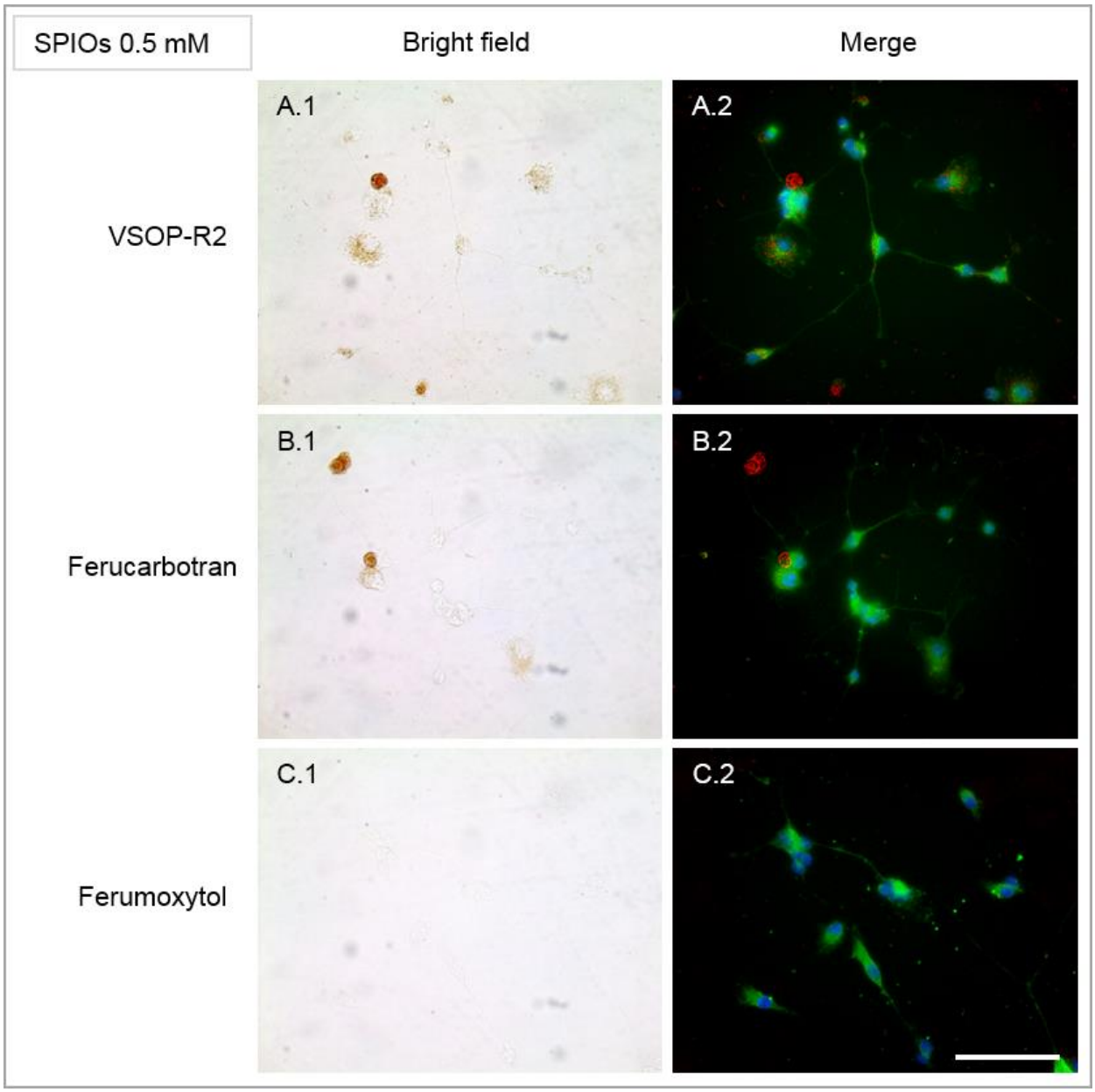
SPIOs 0.5 mM
Bright field
Merge
VSOP-R2
Ferucarbotran
Ferumoxytol
A.1
A.2
B.1
B.2
C.1
C.2

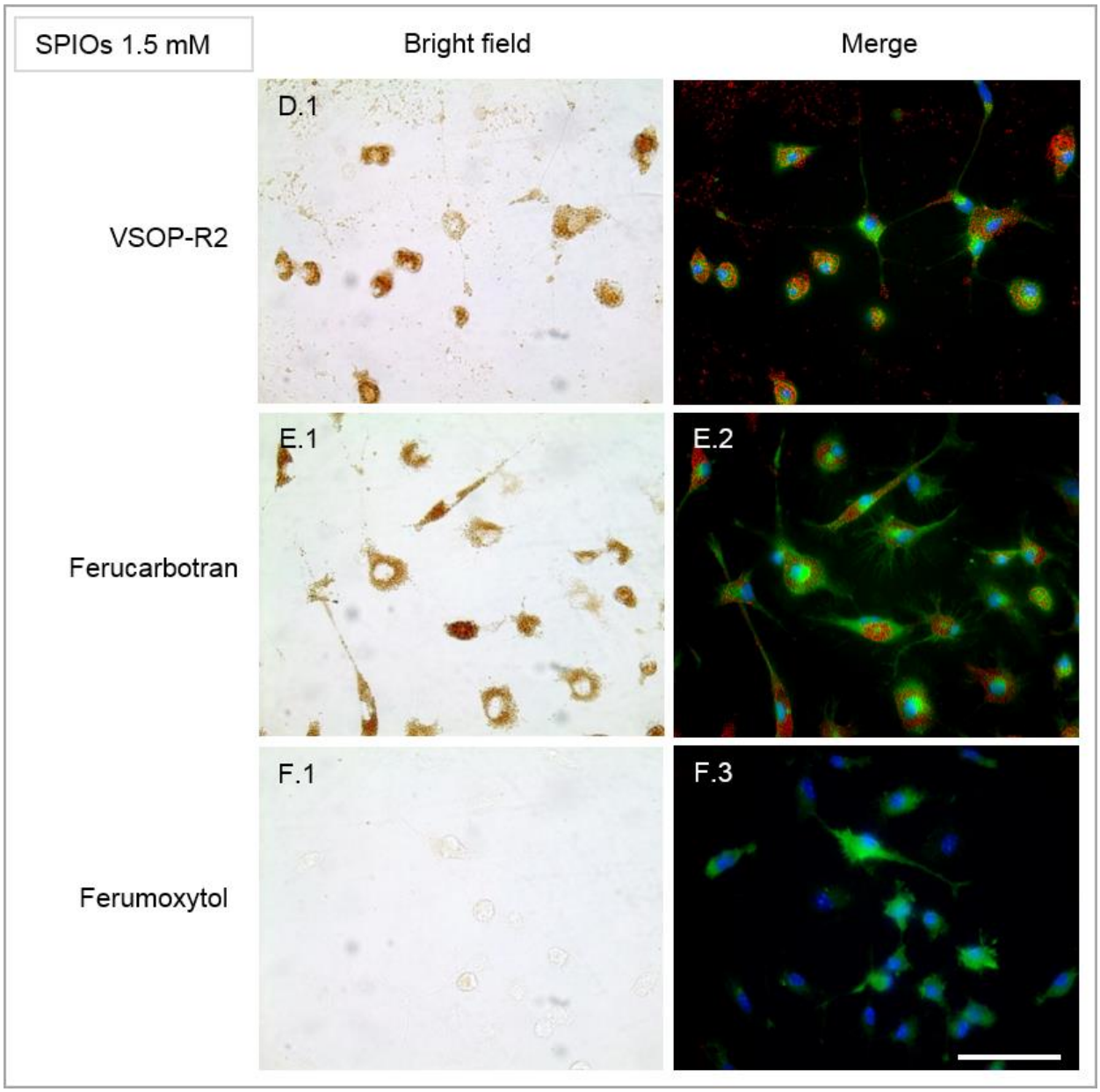
SPIOs 1.5 mM
Bright field
Merge
VSOP-R2
D.1
Ferucarbotran
E.1
E.2
Ferumoxytol
F.1
F.3

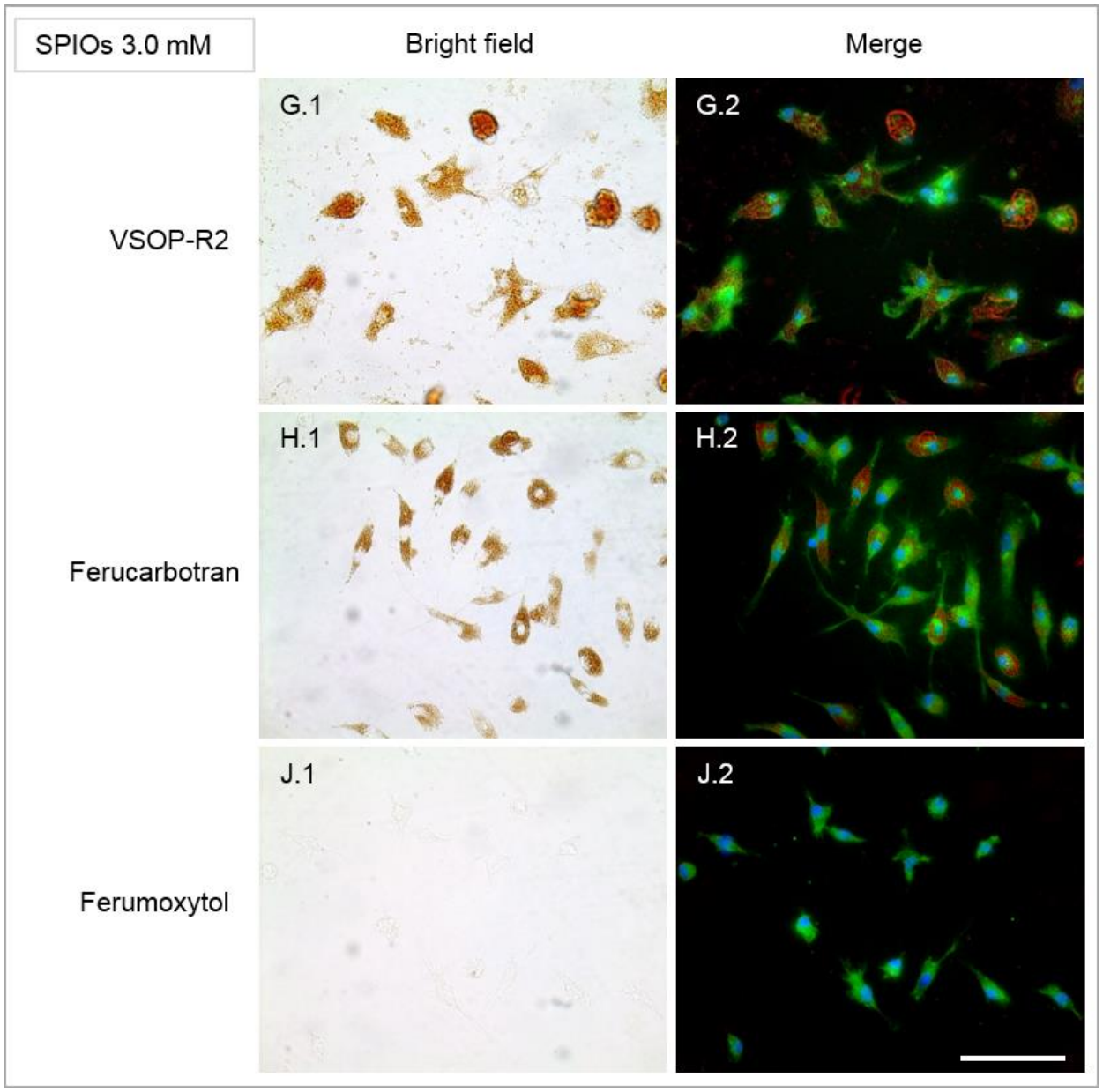
SPIOs 3.0 mM
Bright field
Merge
VSOP-R2
G.1
G.2
Ferucarbotran
H.1
H.2
Ferumoxytol
J.1
J.2

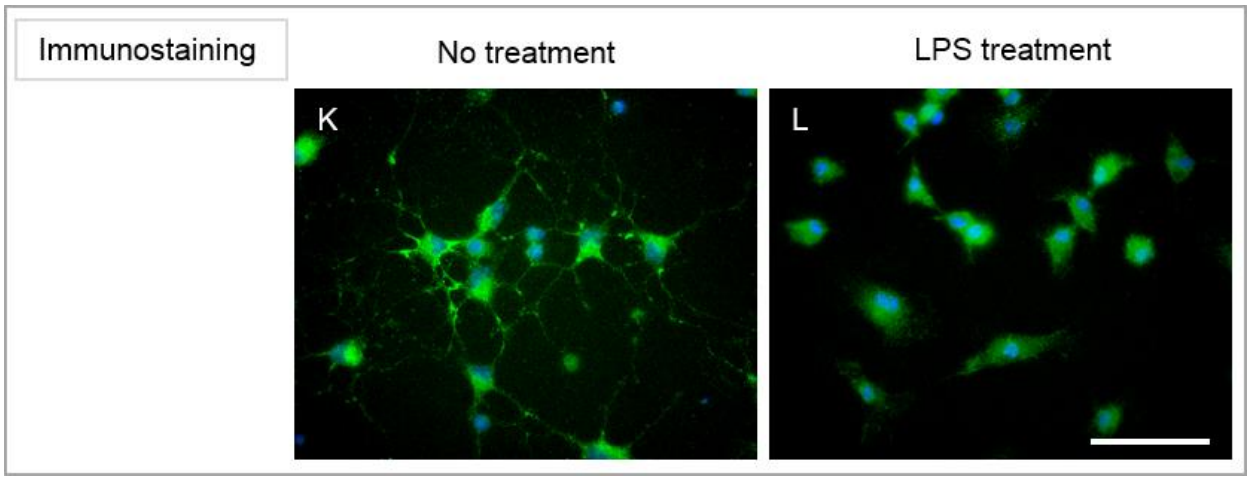

Figure 4: Morphology of primary microglia is altered following SPIO exposure. Primary microglia were incubated for 24 hours with (A, D, G) VSOP-R2, (B, E, H) ferucarbotran and (C, F, J) ferumoxytol in concentrations of (A, B, C) 0.5 mM, (D, E, F) 1.5 mM and (G, H, J) 3.0 mM, respectively, or were (K) untreated or (J) stimulated with 0.1 µg/ml LPS. Microglia cells were immunocytochemically stained using CD11b-FITC-conjugated antibody and Hoechst 33258 nuclear counterstain. (A.1–J.1) In bright field microscopy, SPIOs are visible in brown colour. (A.2–J.2) Merged images of red pseudo-coloured SPIOs and immunostained microglia of corresponding image frames were created using Adobe Photoshop CS5 software. Microglia reveal morphological transformation from a ramified towards an amoeboid phenotype upon accumulation of (A.2, D.2, and G.2) VSOP-R2 and (B.2, E.2, and H.2) ferucarbotran with increasing iron concentrations from (A, B) 0.5 mM to (G, H) 3.0 mM. (C.1, F.1, and J.1) In contrast, bright field images of microglia exposed to ferumoxytol in all concentrations do not show brown appearing particles but amoeboid morphologies in (C.2, F.2, and J.2) fluorescence images. (K) In comparison, untreated microglia show strongly ramified morphologies characteristic for resting microglia, whereas microglia exposed to (L) 0.1 µg/ml LPS show a typical amoeboid phenotype. Scale 20 µm

The bright field images of microglia exposed for 24 hours to all iron concentrations of VSOP-R2 (Figure 4A.1, D.1 and G.1) and ferucarbotran (Figure 4B.1, E.1, H.1) clearly depict brown coloured particles. In contrast, bright field images of microglia incubated with ferumoxytol in all concentrations hardly show any particles (Figure 4C.1, F.1, and J.1), which partially corresponds to Prussian blue staining (Figure 2D.1, D.2). Merged images of green fluorescent microglia and red pseudo-coloured VSOPs (Figure 4A.2, D.2, G.2) and ferucarbotran (Figure 4B.2, E.2, H.2) after exposure for 24 hours to concentrations of 0.5 mM (Figure 4A.2, B.2), 1.5 mM (Figure 4D.2, E.2) and 3.0 mM (Figure 4G.2, H.2), respectively, reveal morphological transformation from a ramified towards an amoeboid phenotype upon particle accumulation. These morphological changes indicate microglial activation (Napoli and Neumann 2009; Ransohoff and Perry 2009; Walker et al. 2014). In comparison, untreated microglia cultured under the same conditions showed ramified morphologies (Figure 4K) characteristic for resting microglia (Ransohoff and Perry 2009), whereas microglia exposed to 0.1 µg/ml LPS show a typical amoeboid phenotype (Figure 4L). Interestingly, merged images of microglia exposed to ferumoxytol in all concentration also reveal amoeboid morphologies without obvious particle accumulation (Figure 4C.2, F.2 and J.2).

SPIOs of anionic surface charge, namely the smallest citrate-coated VSOPs with sizes below 10 nm and the largest, carboxydextran-coated ferucarbotran of around 60 nm induced morphological alterations of microglia. Exposure of microglia to the carboxymethyldextran-coated ferumoxytol of 30 nm in size and neutral surface charge did also affect the morphology of microglial cells without obvious particle accumulation. Furthermore and in accordance with Prussian blue staining (Figure 3), images in Figure 4 show that increasing SPIO concentrations induce morphological transformation towards amoeboid phenotypes of microglia. These data verify that SPIO exposure affects microglial morphology dependent on the SPIO type and concentration (Neubert et al. 2015).

3.1.3 SPIOs influence viability of primary microglia

Based on results obtained previously, I investigated whether increased SPIO accumulation is associated with adverse effects on microglial viability following exposure to iron concentrations of 0.5 mM, 1.5 mM and 3.0 mM for 6 or 24 hours, respectively. Therefore, I performed propidium iodide (PI) staining to assess the viability of primary microglia following SPIO incubation. As PI only perforates cells upon impaired membrane integrity and intercalates into nucleic acids (Takano et al. 2003), the increase in numbers of PI-positive microglia reflects the loss of cell viability (Neubert et al. 2015). For each exposure condition, I acquired images displaying PI-positive microglia, whereas only microglia incubated with 0.5 mM (Figure 5 and 7) and 3.0 mM (Figure 6 and 8) for 6 or 24 hours, respectively, are shown for comparison. Subsequently, I quantified the number of PI-positive cells using ImageJ software and compared the effect of SPIOs on microglia concerning iron concentration and incubation time (Figure 9, black bars). In addition to PI staining, I assessed the amount of cell-associated particles for each exposure condition by quantifying the Prussian blue staining intensity of acquired images using ImageJ software. I used this approach in order to directly compare SPIO accumulation by microglia with numbers of PI-positive cells from the same cell culture after nanoparticle exposure for 6 or 24 hours (Figure 9). I normalized all numbers of PI-positive cells and values of Prussian blue staining intensity and to values of untreated microglia, respectively (Table 4). Thus, values per exposure condition are displayed as percentage in Figure 9.

Table 4: Data and sample size of primary microglia used for PI and Prussian blue quantification. Values refer to average numbers of microglial cells normalized to untreated control cells and are depicted as percentages (illustrated in Figure 9). Numbers of quantified cells (n) for each exposure condition of three independently prepared cultures are shown in brackets, respectively.

	6 h			**24 h**		
	0.5 mM	**1.5 mM**	**3.0 mM**	**0.5 mM**	**1.5 mM**	**3.0 mM**
Number of microglial cultures = 3	**PI-positive microglia (%)**					
VSOP-R1	11.1 (n = 13)	22.5 (n = 13)	45.5 (n = 13)	-2.28 (n = 15)	62.1 (n = 14)	82.6 (n = 14)
VSOP-R2	25.6 (n = 13)	35.2 (n = 13)	42.5 (n = 13)	11.3 (n = 13)	27.2 (n = 14)	63.0 (n = 14)
Ferucarbotran	5.8 (n = 9)	11.2 (n = 9)	32.2 (n = 9)	-6.8 (n = 10)	24.8 (n = 10)	56.6 (n = 10)
Ferumoxytol	-5.5 (n = 12)	-12.5 (n = 12)	-18.9 (n = 12)	-3.7 (n = 10)	-8.6 (n = 11)	-10.3 (n = 11)
Controls	(n = 15)			(n = 17)		
Number of microglial cultures = 4	**Prussian blue staining intensity of microglia (%)**					
VSOP-R1	6.2 (n = 10)	9.0 (n = 10)	14.0 (n = 10)	12.4 (n = 10)	13.3 (n = 10)	19.3 (n = 10)
VSOP-R2	6.7 (n = 10)	8.4 (n = 10)	9.7 (n = 10)	11.7 (n = 11)	16.4 (n = 11)	15.0 (n = 11)
Ferucarbotran	8.6 (n = 9)	10.2 (n = 9)	13.8 (n = 9)	14.4 (n = 9)	19.7 (n = 9)	23.6 (n = 9)
Ferumoxytol	1.1 (n = 8)	0.8 (n = 8)	1.6 (n = 8)	1.7 (n = 8)	5.4 (n = 8)	5.5 (n = 9)
Controls	(n = 18)			(n = 21)		

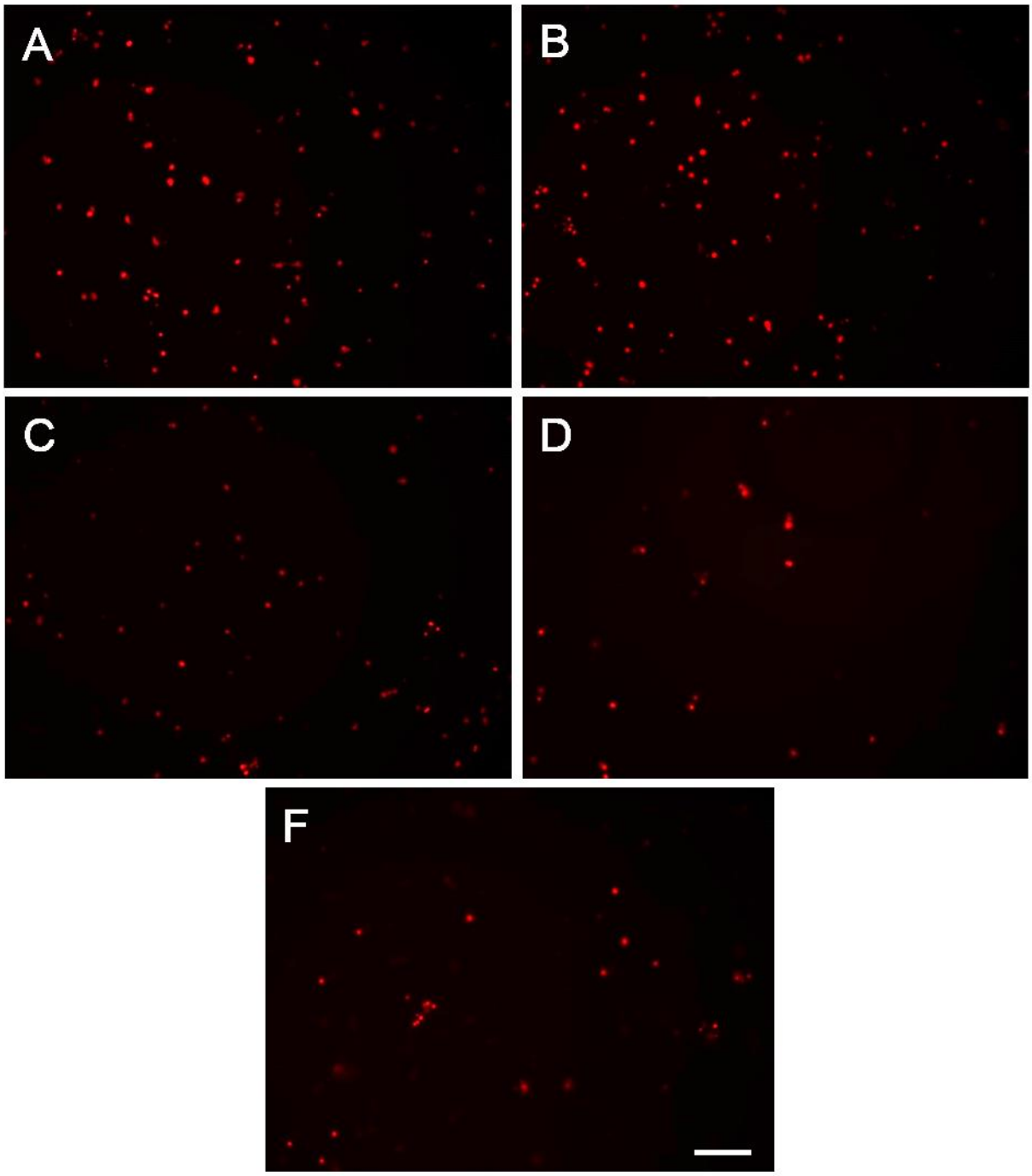

Figure 5: PI-positive primary microglia exposed to 0.5 mM of SPIOs for 6 hours. Primary microglia were exposed to 0.5 M of (A) VSOP-R1, (B) VSOP-R2, (C) ferucarbotran or (D) ferumoxytol for 6 hours or (F) untreated. After incubation with respective particles, microglia in densities of 2×10^5 cells per well were incubated with 500 µg/ml PI for 15 min. Images were acquired with an inverted fluorescence microscope (Olympus IX81). Increased numbers of PI-positive microglia were found after exposure to 0.5 mM of (B) VSOP-R2 compared to other SPIOs and (F) untreated microglia. Scale 100 µm.

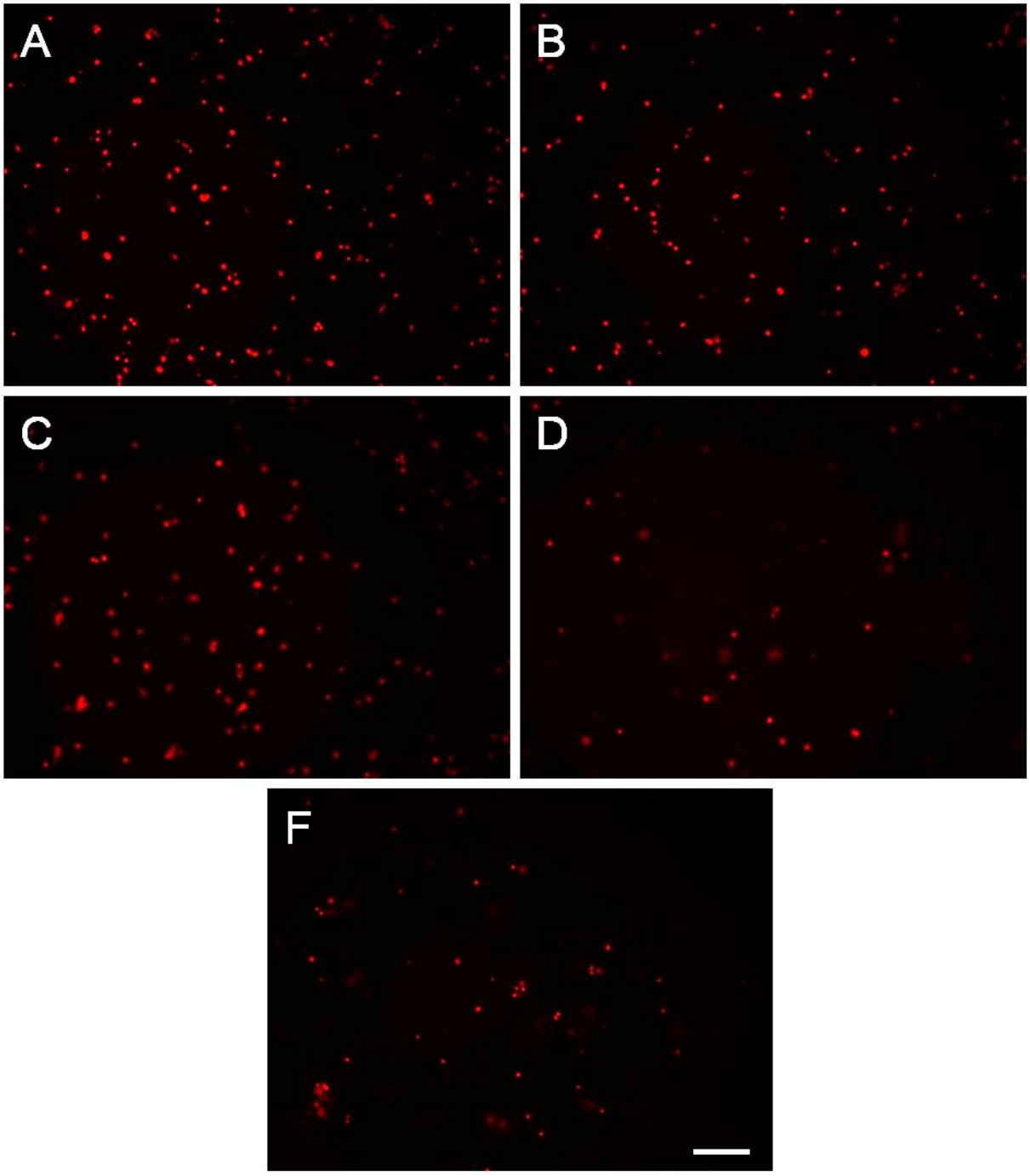

Figure 6: PI-positive primary microglia exposed to 3.0 mM of SPIOs for 6 hours. Primary microglia were exposed to 3.0 M of (A) VSOP-R1, (B) VSOP-R2, (C) ferucarbotran or (D) ferumoxytol for 6 hours or (F) untreated. After incubation with respective particles, microglia in densities of 2×10^5 cells per well were incubated with 500 µg/ml PI for 15 min. Images were acquired with an inverted fluorescence microscope (Olympus IX81). Increased numbers of PI-positive microglia were found after exposure to 0.5 mM of (B) VSOP-R2 and to a lower extend after exposure to 0.5 mM of (A) VSOP-R1 and (C) ferucarbotran compared to (D) ferumoxytol and (F) untreated microglia. Scale 100 µm. (D) Incubation with ferumoxytol showed reduced numbers of PI-positive microglia compared to (F) untreated cells. Scale 100 µm.

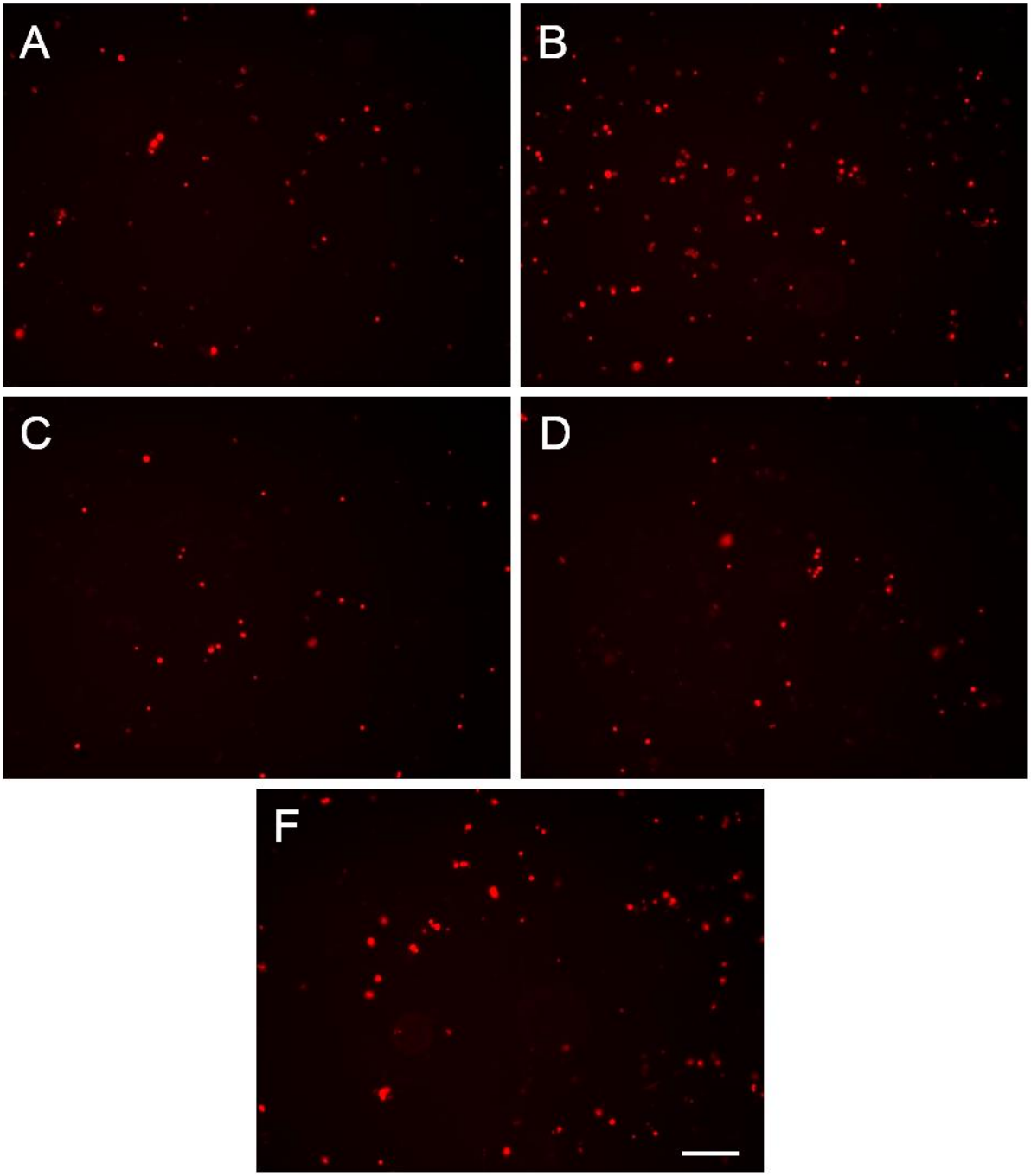

Figure 7: PI-positive primary microglia exposed to 0.5 mM of SPIOs for 24 hours. Primary microglia were exposed to 0.5 M of (A) VSOP-R1, (B) VSOP-R2, (C) ferucarbotran or (D) ferumoxytol for 24 hours or (F) untreated. After incubation with respective particles, microglia in densities of 2×10^5 cells per well were incubated with 500 µg/ml PI for 15 min. Images were acquired with an inverted fluorescence microscope (Olympus IX81). Increased numbers of PI-positive microglia were found after exposure to 0.5 mM of (B) VSOP-R2 and to a lower extend after exposure to 0.5 mM of (A) VSOP-R1 and (C) ferucarbotran compared to (D) ferumoxytol and (F) untreated microglia. Scale 100 µm. (D) Incubation with ferumoxytol showed reduced numbers of PI-positive microglia compared to (F) untreated cells. Scale 100 µm.

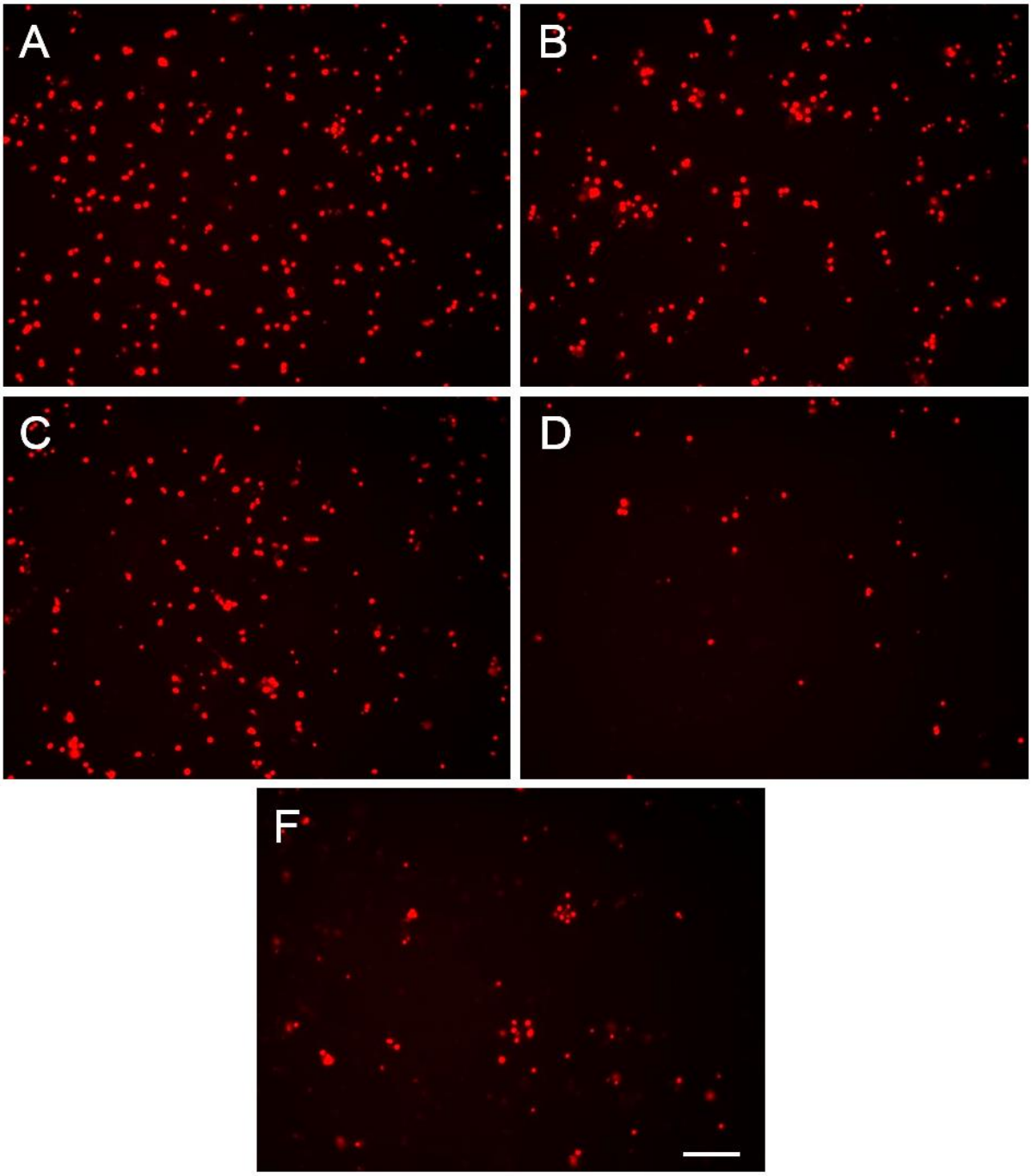

Figure 8: PI-positive primary microglia exposed to 3.0 mM of SPIOs for 24 hours. Primary microglia were exposed to 3.0 mM of (A) VSOP-R1, (B) VSOP-R2, (C) ferucarbotran or (D) ferumoxytol for 24 hours or (F) untreated. After incubation with respective particles, microglia in densities of 2×10^5 cells per well were incubated with 500 µg/ml PI for 15 min. Images were acquired with an inverted fluorescence microscope (Olympus IX81). High numbers of PI-positive microglia were found after exposure to 3.0 mM of (A) VSOP-R1, (B) VSOP-R2 and (C) ferucarbotran, whereas numbers of PI-positive microglia of the latter two appear to be increased to a similar extend. (D) Incubation with ferumoxytol showed reduced numbers of PI-positive microglia compared to (F) untreated cells. Scale 100 µm.

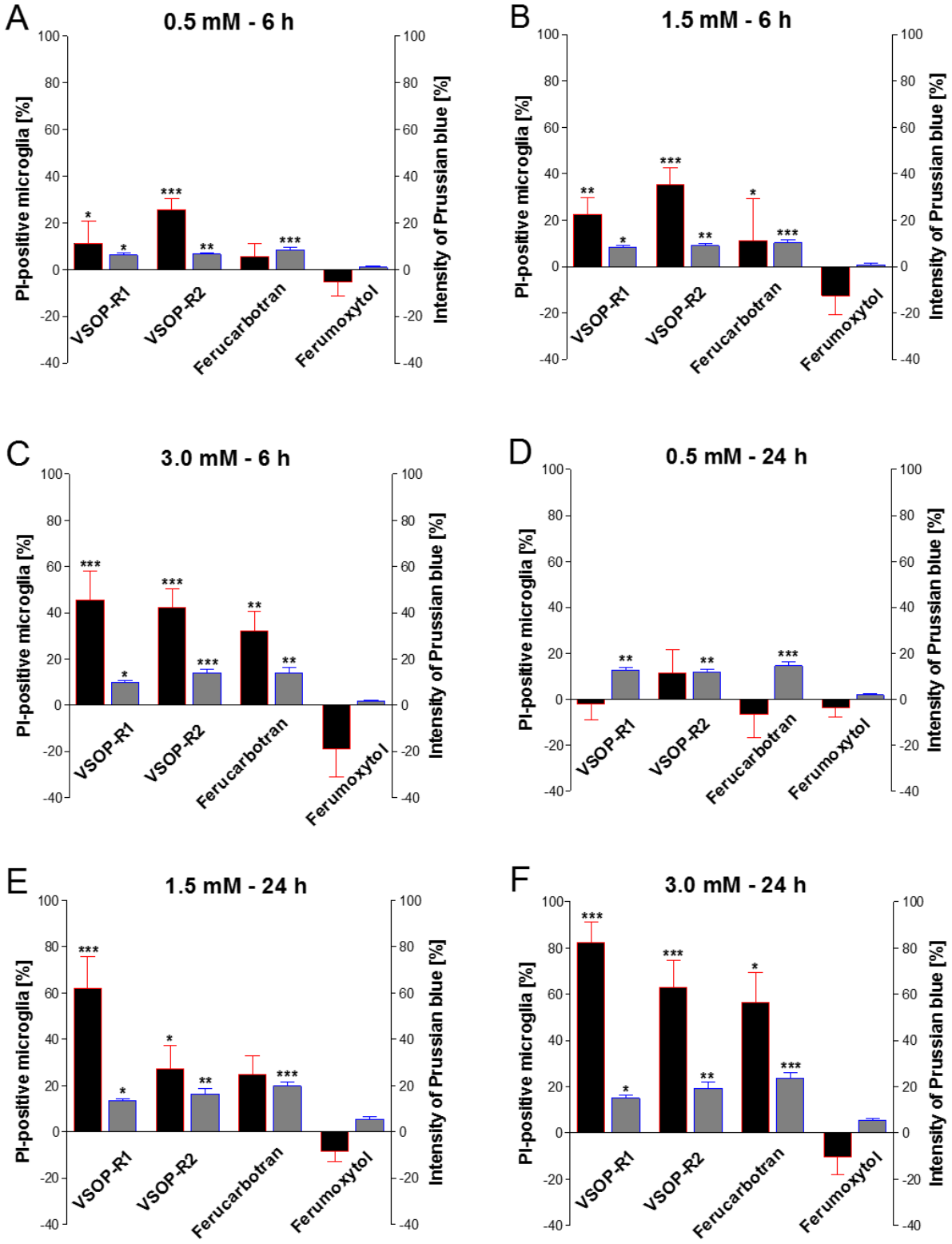

Figure 9: SPIO influence the viability of primary microglia. Microglia were incubated for either (A-C) 6 hours or (D-F) 24 hours with SPIOs of different iron concentration as indicated. Acquired images of PI- and Prussian blue-positive cells were quantified using ImageJ software and values were normalized to untreated microglia using GraphPad Prism 5 software. Black bars indicate the percentage of PI-positive microglia (left y-axis in each plot); grey bars indicate the

percentage of Prussian blue staining intensity, referring to microglial iron content (right y-axis). (A–F) Numbers of PI-positive cells increased by more than 20% after extended incubation from 6 to 24 hours with SPIOs except ferumoxytol. Microglial iron accumulation after incubation with VSOPs and ferucarbotran significantly increased compared to cells incubated with ferumoxytol for 6 or 24 hours. However, increases in microglial SPIO accumulation did not correspond with proportional increases in the numbers of PI-positive cells. Kruskal–Wallis one-way ANOVA and Dunn's multiple comparison post hoc test, expressed as mean ± SEM: ***p<0.0004; **p<0.01; *p<0.05.

The image evaluation of PI-positive cells following exposure to all SPIOs, except after incubation with ferumoxytol, revealed increased numbers of non-viable primary microglia with increasing iron concentration and incubation time (Figure 5-8). These observations are in line with the quantification of acquired PI images using ImageJ software (Figure 9). The obtained data clearly show decreased microglial viability, as indicated by the percentage of PI-positive cells, after incubation with high concentrations of 1.5 and 3.0 mM of VSOPs and ferucarbotran, but not ferumoxytol (Figure 9B, C, E and F). I observed a strong increase in numbers of PI-positive microglia with a maximum of more than 30 % (see Table 4 for data) for all SPIOs with iron concentration of 3.0 mM, except ferumoxytol when comparing data between 6 and 24 hours of exposure (Figure 9C and F). The largest increases in PI-positive microglia were found after exposure to 1.5 and 3.0 mM of VSOP-R1 (Figure 9E and F) and also after exposure to 3.0 mM of VSOP-R2 or ferucarbotran for 24 hours (Figure 9C and F).

Next, I compared microglial particle accumulation according to Prussian blue staining intensity following incubation with 0.5 mM, 1.5 mM and 3.0 mM for 6 and/ or 24 hours of respective SPIOs (Figure 9, grey bars). The quantification of iron detected by means of Prussian blue revealed significantly higher staining intensities of microglia exposed to VSOPs or ferucarbotran, respectively, than microglia exposed to ferumoxytol for 6 or 24 hours (Figure 9A–F). I also observed that particle accumulation increased with increasing concentration for all SPIOs (Figure 9A–F). Direct comparison between 6 (Figure 9A–C) and 24 hours (Figure 9D–F) of exposure showed only marginal increases in Prussian blue staining intensities of microglia after exposure to all particle concentrations, whereas incubation with 1.5 mM (Figure 9E) and 3.0 mM (Figure 9F) of ferucarbotran showed the highest increase of 9.5 and 9.8 % (see Table 4 for data), respectively. However, the observed increases in Prussian blue-staining intensity after exposure of microglia to VSOPs or ferucarbotran did not proportionally increase with concentrations three or six times higher than 0.5 mM (Neubert et al. 2015).

When comparing numbers of PI-positive microglia with respective Prussian blue staining intensities, I observed an association between microglial viability and iron accumulation. In the experimental conditions I observed that increased accumulation of SPIOs positively correlated with the PI-positive, nonviable cell bodies. However, this observation did not apply for exposure to nanoparticles in iron concentrations of 0.5 mM (Figure 9A and D), for all concentrations of ferumoxytol (Figure 9A–F) and for 1.5 mM of VSOP-R2 (Figure 9B and E) when comparing 6 and 24 hours of exposure. While overall Prussian blue-staining intensities were highest after exposure for 24 hours to ferucarbotran in all concentrations (Figure 9D–F), numbers of PI-positive microglia were higher after incubation with VSOP-R1 and VSOP-R2 for both the 1.5 mM and the 3.0 mM exposure conditions (Figure 9E and F). Interestingly, these data showed concentration-dependent decreases of microglial PI values after exposure to ferumoxytol for 6 or 24 hours (Figure 9A-F).

In turn, this revealed statistically significant differences when comparing ferumoxytol with VSOPs and ferucarbotran, but not after exposure to 0.5 mM of all SPIOs for 24 h (Figure 9D), or to 0.5 mM ferucarbotran for 6 hours (Figure 9A) and 1.5 mM ferucarbotran for 24 hours (Figure 9E).

In conclusion, prolonged exposure times and microglial accumulations of VSOPs or ferucarbotran negatively affect cell viability, whereas exposure to ferumoxytol did not cause decreased microglial viability although minimal amounts of iron were detected (Neubert et al. 2015). These data, concerning effects of VSOPs and ferucarbotran correspond to results I obtained for the affected microglial morphology (section 3.1.2)

3.2 SPIOs affect the morphology of primary neurons dependent on particle composition and cell culture model

3.2.1 SPIO-type dependent accumulation by primary hippocampal neurons

To address the question of whether SPIOs are also accumulated by primary neurons after 24 hours of incubation, I performed Prussian blue staining that is a commonly used method to detect cell-associated particles (Cengelli et al. 2006; Tysiak et al. 2009; Andreas et al. 2012; Wagner et al. 2013; Jarockyte et al. 2016). In addition, I applied nuclear fast red counterstain to visualize cell nuclei in intense pink and the cytoplasm in moderate pink colour (Cengelli et al. 2006; Pinkernelle et al. 2012). This allowed for visual examination of neuron-associated SPIOs with light microscopy as described above. The image evaluation revealed that only VSOPs and ferucarbotran accumulated in neuronal somata and neurites. An example is depicted in Figure 10, where VSOP-R2 are shown as representative for the very small nanoparticles. Especially, neurons exposed to the highest iron concentration of 3.0 mM of VSOP-R2 and ferucarbotran showed substantial Prussian blue-positive deposits (Figure 10 A and B) compared to the same concentration of ferumoxytol (Figure 10C) or untreated neurons (Figure 10D).

These results demonstrate that the smallest, citrate-coated VSOPs and the largest, carboxydextran-coated ferucarbotran, both of anionic surface charge are bound, presumably by extracellular matrix components of neuronal somata and neurites of primary neurons from monocultures (Ludwig et al. 2013; Neubert et al. 2015). In contrast, carboxymethyldextran-coated ferumoxytol exhibiting neutral charge and intermediate size of 30 nm was not accumulated by cell bodies or neuronal processes. Hence, SPIO composition, including charge and size influences the interaction with cell membranes of primary neurons.

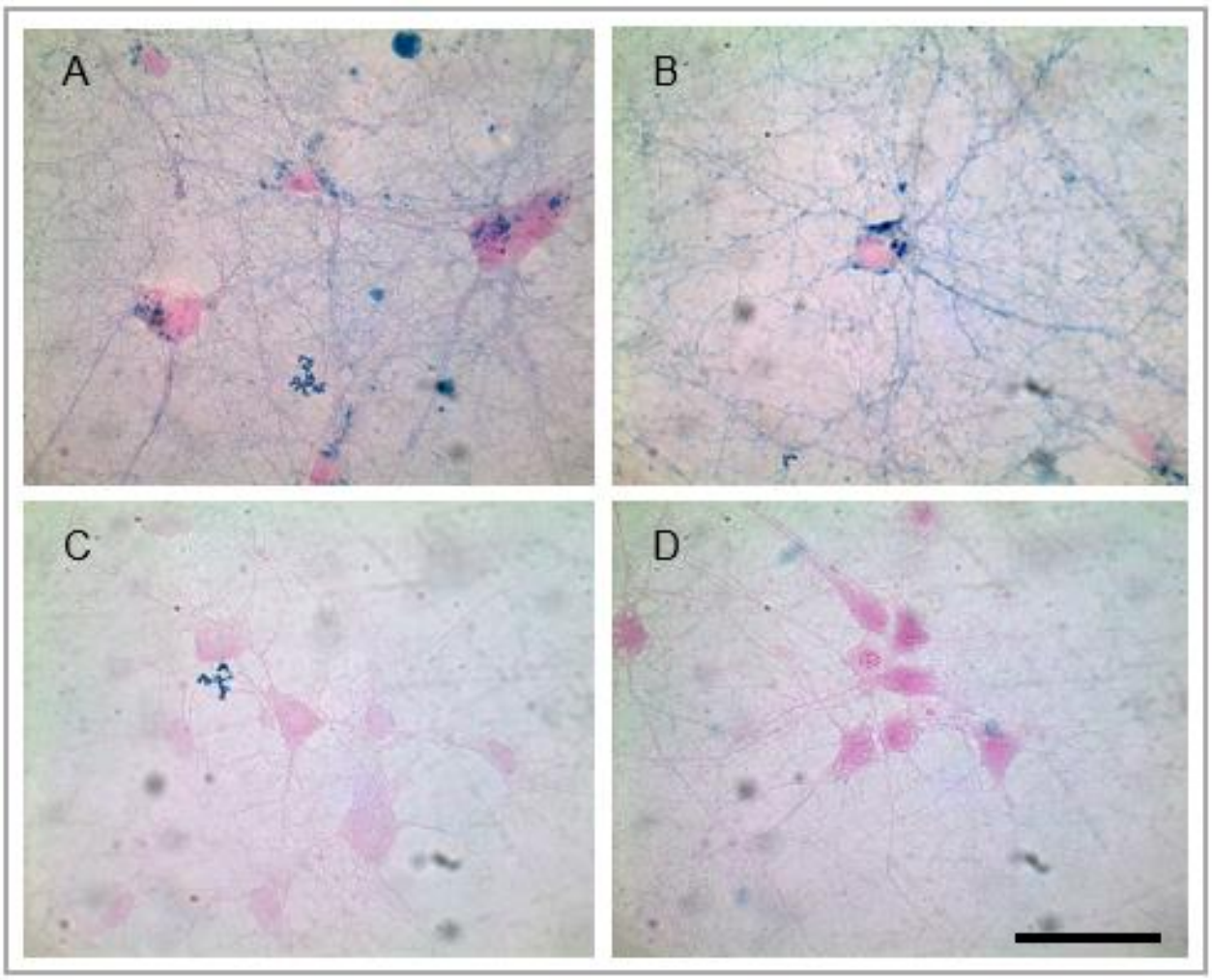

Figure 10: Accumulation of SPIOs by primary neurons in monoculture is dependent on the particle-type. To visualize cell-associated particles, primary neurons were stained with Prussian blue and nuclear fast red counterstain after exposure to 3.0 mM of (A) VSOP-R2, (B) ferucarbotran or (C) ferumoxytol for 24 hours, or (D) without treatment. VSOP-R2 is shown as representatives for the very small nanoparticles. Only (A) VSOPs and (B) ferucarbotran were accumulated by neurons. These SPIOs were found distributed along neurites and considerably accumulated at neuronal somata as depicted as large blue dots. (C) Neurons exposed to ferumoxytol did not show Prussian blue detectable iron. Scale 40 µm

In order to examine the morphology of primary hippocampal neurons after the exposure to three different concentrations of SPIOs for 24 hours, I initially performed immunocytochemical staining using the SMI-32 antibody followed by the nucleic acid counterstain Hoechst 33258. SMI-32 antibody stains non-phosphorylated neurofilament proteins and is a specific marker for differentiating neurons (Del Rio and DeFelipe 1994). Therefore, it is well suited to visualize neuronal morphology at 10 DIV. Just as in section 3.1.1, I captured bright field images to identify SPIOs appearing in brown colour, pseudo-coloured these in red using Adobe Photoshop CS5 software and merged them with immunofluorescence images to visualize neuron-associated particles. In Figure 11, VSOP-R2 serves as representative for the very small nanoparticles. In corresponding images, arrows heads point towards neuronal somata, respectively.

The bright field images of neurons exposed for 24 hours only show marginal deposits of VSOP-R2 (Figure 11A.1, D.1 and G.1) and ferucarbotran (Figure 11B.1, E.1 and H.1), which increase with increasing particle iron concentrations, respectively. I mainly observed SPIO accumulations proximal to neuronal somata and also distributed along neurites. Bright field images of primary neurons incubated with ferumoxytol in all iron concentrations did not reveal accumulated particles (Figure 11C.1, F.1 and J.1).

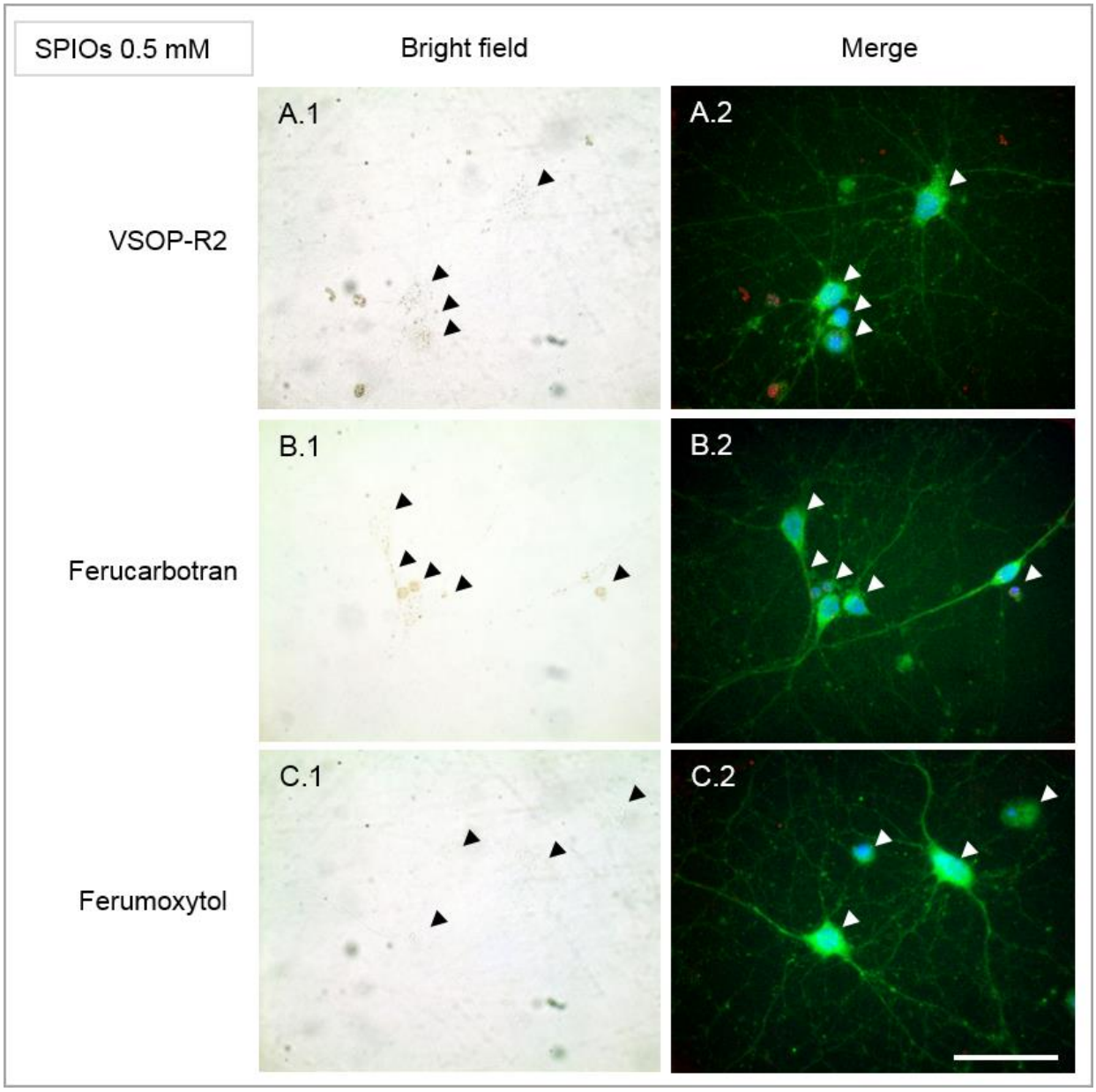
SPIOs 0.5 mM
Bright field
Merge
VSOP-R2
Ferucarbotran
Ferumoxytol
A.1
A.2
B.1
B.2
C.1
C.2

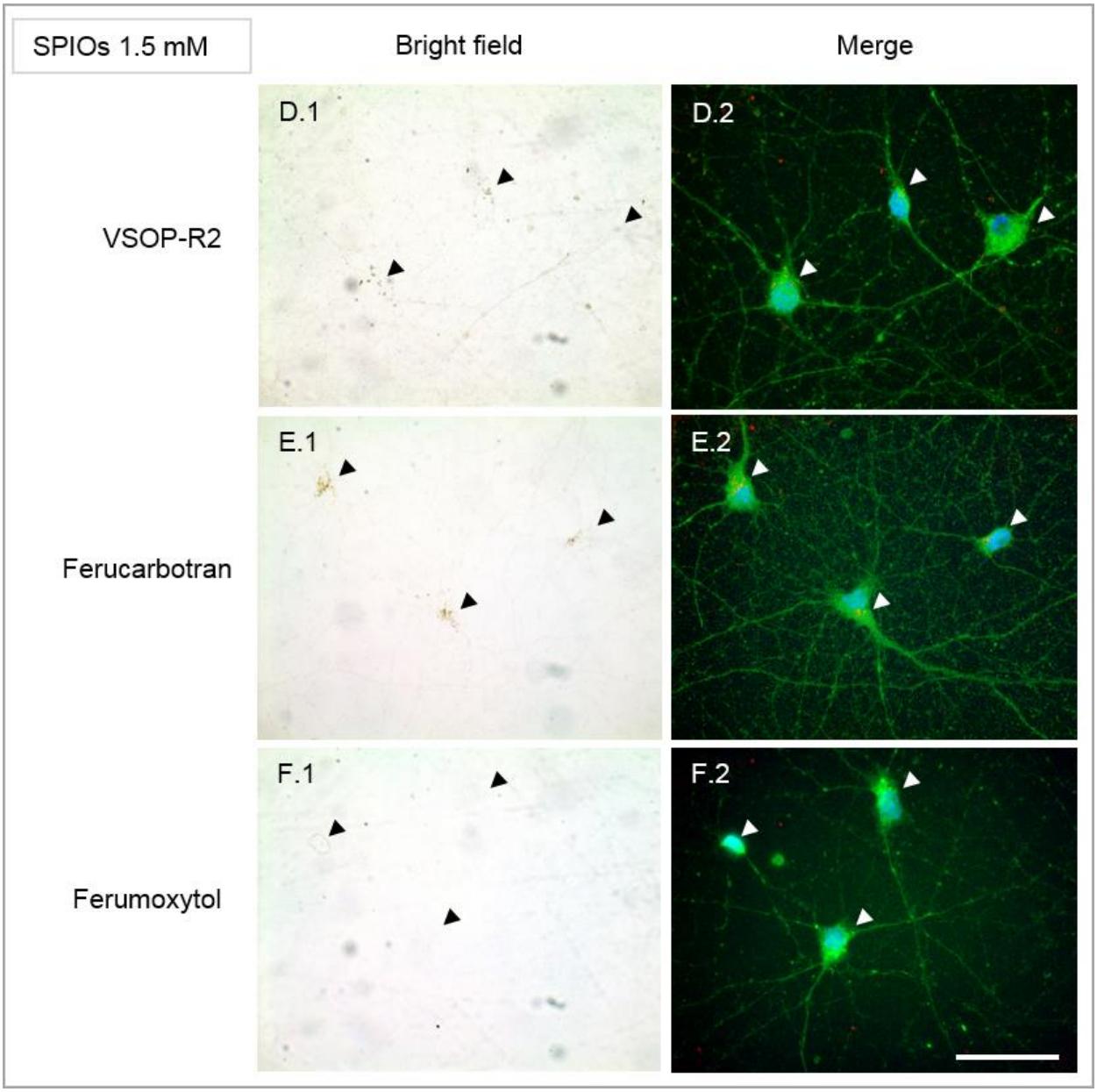
SPIOs 1.5 mM
Bright field
Merge
VSOP-R2
Ferucarbotran
Ferumoxytol
D.1
D.2
E.1
E.2
F.1
F.2

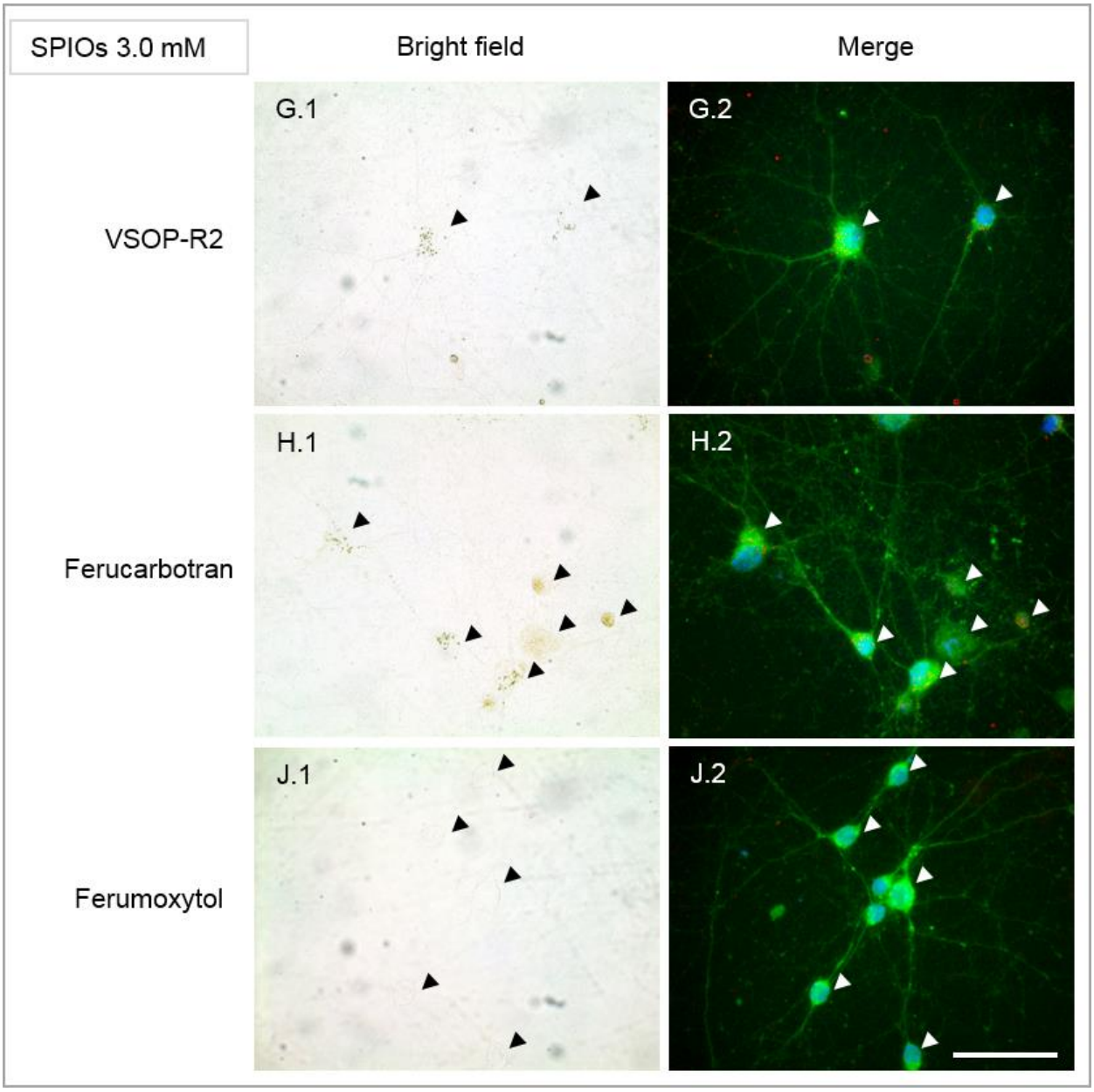
SPIOs 3.0 mM
Bright field
Merge
VSOP-R2
Ferucarbotran
Ferumoxytol
G.1
G.2
H.1
H.2
J.1
J.2

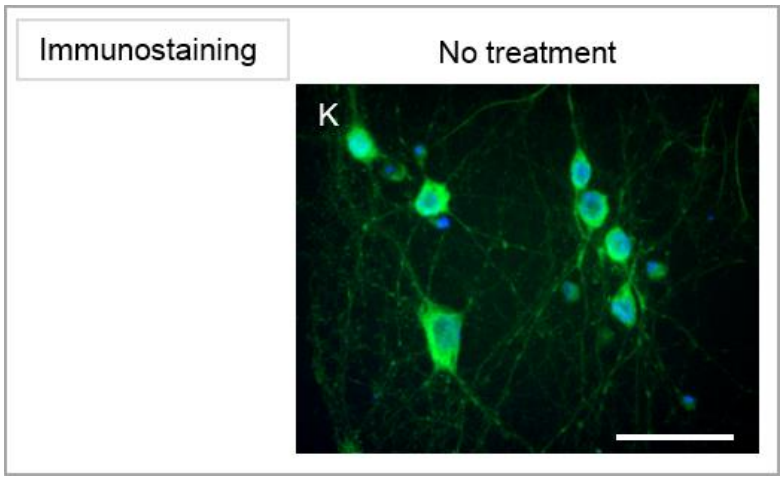

Figure 11: Morphology of primary neurons from monocultures following SPIO exposure show signs of neuronal degeneration. Primary neurons were incubated for 24 hours with (A, D, G) VSOP-R2, (B, E, H) ferucarbotran and (C, F, J) ferumoxytol in concentrations of (A, B, C) 0.5 mM, (D, E, F) 1.5 mM and (G, H, J) 3.0 mM, respectively. Neurons were immunocytochemically stained using SMI-32 primary antibody Alexa Fluor 488 and Hoechst 33258 nuclear counterstain. (A.1–J.1) In bright field microscopy, SPIOs are appear in brown colour but were hardly found. Arrow heads indicate the location of neurons in corresponding images. (A.2–J.2) Merged images of red pseudo-coloured SPIOs and immunostained neurons of corresponding image frames were created using Adobe Photoshop CS5 software. (K) Immunofluorescence image of neurons without treatment. Scale 40 µm

The representative fluorescent images of SPIO-exposed primary neurons were acquired to visually assess potential effects of SPIOs on neuronal morphology. To obtain conclusive data concerning the impact of SPIO exposure, I further explored the morphology of primary neurons, which is described in the following section.

3.2.2 Primary hippocampal neurons degenerate after SPIO exposure

In order to quantitatively determine the influence of SPIO exposure for 24 hours on the morphology of primary hippocampal neurons from monocultures, I applied Sholl analysis (Sholl 1953). This is a commonly used method that allows quantification of neuronal processes by counting the number of neurite crossings on concentric circles with a gradually increasing radius (Nakayama et al. 2000; Rosario et al. 2012). I quantified the number of neurite intersections of 750 primary neurons in total on 24 concentric circles with the innermost circle coinciding with the centre of the soma. An example of a primary neuron studied by means of Sholl analysis is shown in Figure 12. After manual counting of neurite intersections per circle, I graphically depicted the average number of neurite intersections from all neurons in distance of up to 500 µm from the soma (Figure 13A, C and E). For statistical analysis, I quantified the average number of neurite intersections per cell and compared values using GraphPad Prism 5 software (Figure 13B, D and F).

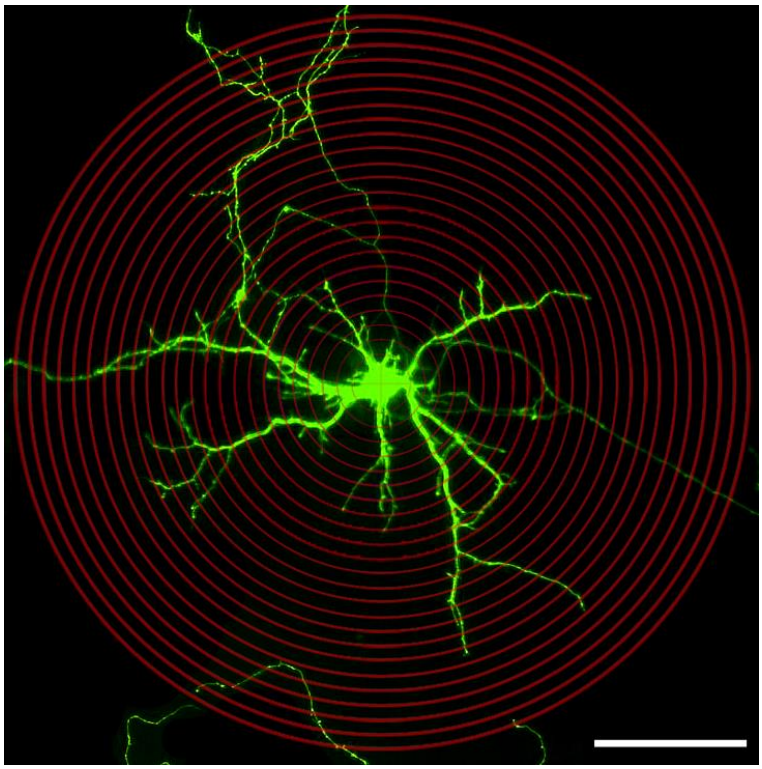

Figure 12: Immunofluorescence example image of an untreated primary neuron examined with Sholl analysis. In Sholl analysis, neurite intersections of eGFP-transfected- and Tuj1-positive neurons were manually counted using 24 20 µm-spaced concentric circles (red) with the innermost circle coinciding with the centre of the soma. Scale 100 µm

Table 5: Data and sample size of neurons from monocultures used in Sholl and degeneration analysis. For Sholl analysis, total numbers of neurons analyzed for each exposure condition are shown. For degeneration analysis, counted total numbers compared with numbers of degenerated neurons are shown, respectively. Numbers of quantified cells (n) for each exposure condition of three independently prepared neuronal cultures are shown in brackets, respectively. Ratios as percentage for both analyses are depicted in Figure 13 and Figure 15, respectively.

Number of neuronal cell cultures = 3	**Sholl analysis (number of analyzed neurons)**			**Degeneration analysis (number of total /degenerated neurons)**		
	0.5 mM	**1.5 mM**	**3.0 mM**	**0.5 mM**	**1.5 mM**	**3.0 mM**
VSOP-R1	n = 55	n = 67	n = 60	249 / 83 (n = 5)	163 / 63 (n = 5)	195 / 80 (n = 5)
VSOP-R2	n = 63	n = 61	n = 79	294 / 86 (n = 5)	210 / 74 (n = 5)	210 / 70 (n = 5)
Ferucarbotran	n = 52	n = 47	n = 50	221 / 85 (n = 5)	151 / 66 (n = 5)	211 / 88 (n = 5)
Ferumoxytol	n = 62	n = 50	n = 48	246 / 84 (n = 5)	233 / 89 (n = 5)	229 / 90 (n = 5)
Controls	n = 56			579 / 129 (n = 6)		

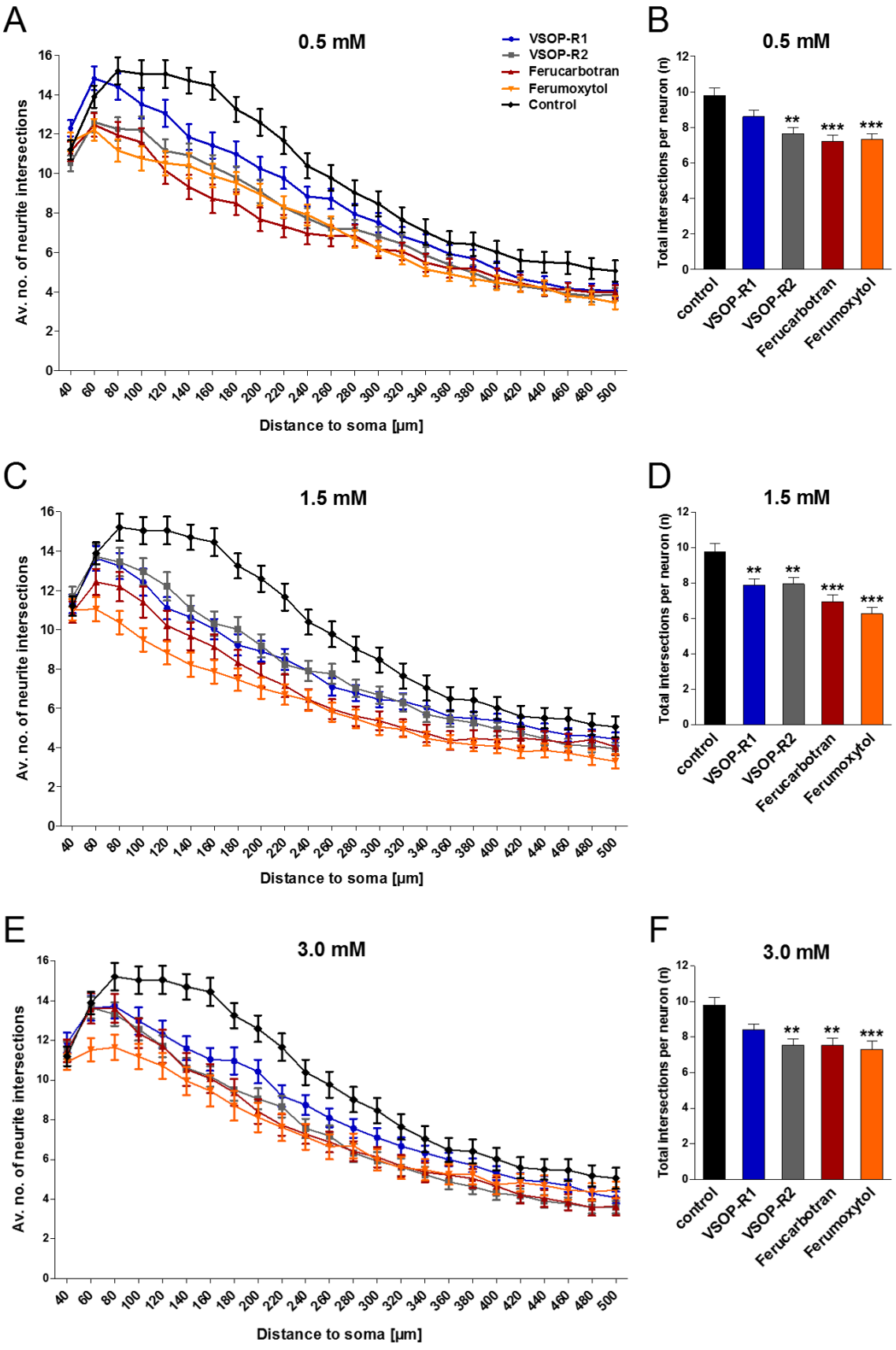

Figure 13: SPIO exposure leads to reduction in numbers of neurites of primary neurons from monocultures. (A, C, E) Average numbers of neurite intersections from 750 neurons in total were quantified by means of Sholl analysis and are depicted in increasing distance to the soma for each exposure condition. Untreated neurons are referred to as

control. Sholl analyses of primary neurons shows a downward shifted intersection curve that reflects reduced numbers of neurites after SPIO exposure for 24 hours (coloured lines) compared to untreated neurons (black line). (B, D, F) Quantification of average numbers of neurite intersections with concentric circles per neuron exposed to indicated SPIOs and concentrations, respectively. Significant reduction in average number of neurites were found for all concentrations of VSOP-R2, ferucarbotran and ferumoxytol and 1.5 mM VSOP-R1. Decreased average numbers of neurites after exposure to 0.5 mM and 3.0 mM of VSOP-R1 were found but were not significantly different. Kruskal–Wallis one-way ANOVA and Dunn's multiple comparison post hoc test, expressed as means ± SEM: ***p<0.0001; **p<0.01; *p<0.05.

Sholl analysis revealed reduced neurite complexity of primary neurons following exposure to all SPIOs of all concentrations (Figure 13A, C and E). The downward shifted intersection curve for neurons exposed to SPIOs for 24 hours reflects reduced numbers of neuronal processes after SPIO exposure (Figure 13A, C and E, coloured lines) compared to untreated neurons (Figure 13A, C and E, black lines, referred to as control). I found substantially reduced numbers of neurites, especially, in proximal extensions of nanoparticle exposed neurons (Figure 13, coloured lines) compared to numbers of neurite intersection of untreated neurons (Figure 13, black line). Statistically significant reduction of average neurite intersections were observed for neurons exposed to all SPIOs in all concentrations, except for 0.5 and 3.0 mM of VSOP-R1 compared to untreated neurons (Figure 13B, D and F). Consequently, SPIOs adversely affected neurite complexity during the differentiation process of primary neurons in monoculture during particle incubation for 24 hours, which was independent of the particle composition (Neubert et al. 2015).

Subsequently, I raised the question of whether SPIOs also cause neuronal degeneration or impair neuronal survival after exposure to neurons for 24 hours. Morphologically, neuronal degeneration is defined by fragmented neuronal processes, cell shrinkage, and somatic swelling (Adamec et al. 2001). To investigate this, I manually quantified total numbers and numbers of obviously degenerated primary neurons that were exposed to SPIOs in all concentrations or untreated using fluorescence microscopy. I only counted neurons fulfilling the morphological criteria of neuronal degeneration, which is displayed in the example image in Figure 14. In total, I manually counted 3191 total and 1087 degenerated neurons from monocultures of three independently prepared cell cultures (Table 5).

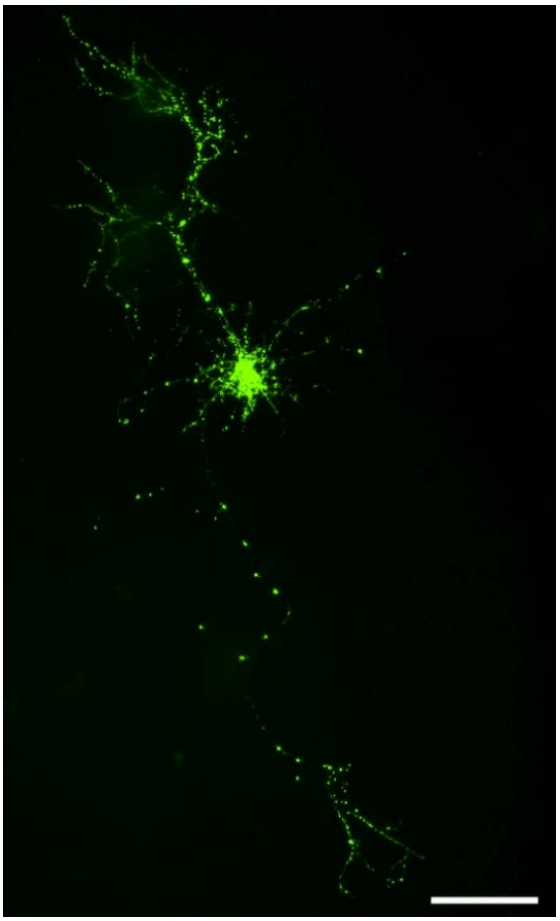

Figure 14: Representative image of a degenerated primary neuron incubated with 3.0 mM of VSOP-R1. To determine numbers of degenerated neurons, eGFP-transfected- and Tuj1-positive cells were manually counted using fluorescence microscopy. Only neurons that showed obvious sign of degeneration, including fragmentation of neuronal processes, cell shrinkage, and somatic swelling were counted (Adamec et al. 2001). Scale 100 µm

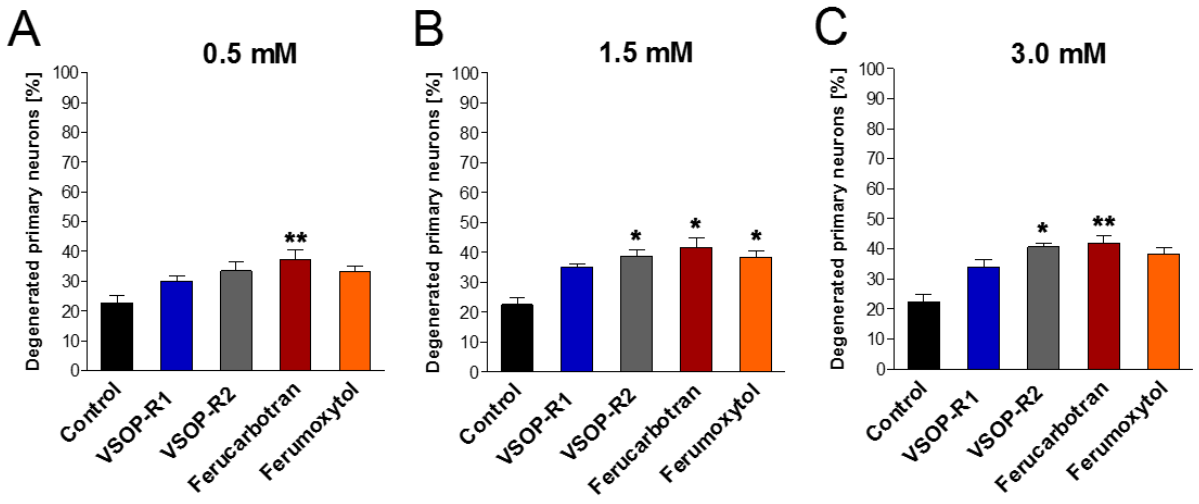

Figure 15: Neurons from monocultures degenerated after SPIO exposure. Numbers of degenerated neurons were manually counted in fluorescence microscopy following the exposure to (A) 0.5 mM, (B) 1.5 mM (C) or 3.0 mM of the respective SPIOs. All values were normalized to untreated neurons (control) and are displayed as percentage. All

concentrations of ferucarbotran led to significant increase in numbers of degenerated neurons compared to untreated neurons (control). Kruskal–Wallis one-way ANOVA and Dunn's multiple comparison post hoc test, expressed as means ± SEM: (A) **p ≤ 0.0174; (B) *p < 0.05; (C) *p < 0.05; **p ≤ 0.0029.

The quantification revealed significant increases in neuronal degeneration after exposing primary neurons to all concentrations of ferucarbotran (Figure 15A – C), to 1.5 mM (Figure 15B) and 3.0 mM of VSOP-R2 (Figure 15C), and to 1.5 mM of ferumoxytol (Figure 15B) compared to untreated neurons (Figure 15 A, B and C, referred to as control). Hence, the largest and carboxydextran-coated ferucarbotran had the most adverse effect on primary neurons. In addition, high concentrations of the citrate-coated VSOP-R2, which also has an anionic surface charge induced significantly increased neuronal degeneration.

Interestingly, and in contrast to the effect on the viability of primary microglia (Figure 5), ferucarbotran but not VSOP-R1 resulted in significantly increased numbers of degenerated cells. Consequently, ferucarbotran in all concentrations most strongly impaired the viability of primary neurons. Furthermore, while ferumoxytol did not cause immediate death of primary microglia (Figure 5), it induced a decrease in the number of neurites (Figure 9) and increased degeneration of primary neurons (Figure 15) (Neubert et al. 2015).

To further investigate the heterogeneous effects of SPIOs, I studied the influence of these nanoparticles in respective concentrations in a more complex cell-culture model using neuron-glia co-cultures.

3.2.3 Neurons in neuron–glia co-cultures do not substantially degenerate after SPIO exposure

In neuron-glia co-cultures, I analysed neuronal morphology and vitality under equivalent exposure conditions as described for neurons from monocultures. The aim was to examine whether glial cells in co-cultures help to maintain homeostatic balance and protect neurons from adverse SPIO effects. Due to their strong phagocytic activity, microglia were thought to contribute to neuroprotection. To verify that equal numbers of neurons and microglial cells were included in co-cultures, I performed qRT-PCR (Figure 12). The cell markers I applied to assess relative gene expression levels were neuron-specific class III β-tubulin (Tuj1) to determine neuronal origin, glial fibrillary acidic protein (GFAP) as a marker for astrocytes, and the ionized calcium-binding adaptor molecule 1 (Iba1) as a marker for microglial cells. The marker GAPDH as a ubiquitously expressed house-keeping gene was used for normalization. Subsequently, I performed Sholl analysis on neurons from neuron-glia co-culture to investigate neuronal morphology after SPIO exposure and quantified numbers of degenerated cells using fluorescence microscopy. In total, I manually counted 344 viable and 84 degenerated neurons from co-cultures (Table 6).

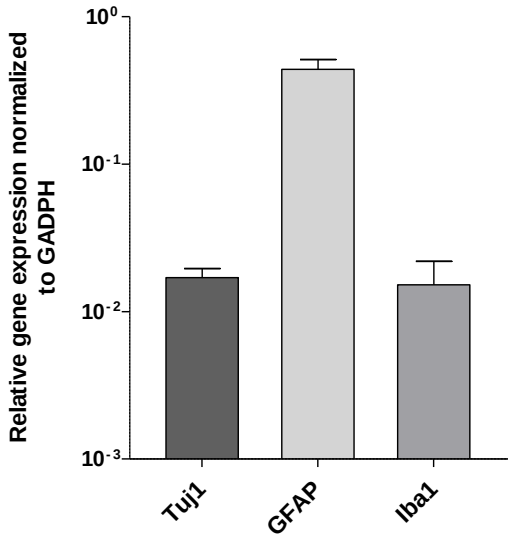

Figure 16: Quantitative real-time PCR of neuron-glia co-cultures. Relative gene expression levels of neurons (Tuj1), astrocytes (GFAP) and microglia (Iba1) in co-culture were determined at 10 DIV and normalized to GAPDH (logarithmic scaling). Microglia and neurons show corresponding expression levels.

The quantification by means of qRT-PCR revealed corresponding gene expression levels of Tuj1 and Iba1 in neuron-glia co-culture after 10 DIV (Figure 12). Compared to Tuj1 and Iba1, the relative expression levels of GFAP were shown to be approximately twice as high (Neubert et al. 2015).

Table 6: Data and sample size of neurons from neuron–glia co-cultures used in Sholl and degeneration analyses. For Sholl analysis, total numbers of neurons analyzed for each exposure condition are shown. For degeneration analysis, counted total numbers compared with numbers of degenerated neurons are shown, respectively. Numbers of quantified cells (n) for each exposure condition of four independently prepared neuronal cultures are shown in brackets, respectively. Ratios as percentage for both analyses are depicted in in Figure 17 and Figure 18, respectively.

Number of neuronal cell cultures = 4	**Sholl analysis (number of analyzed neurons)**			**Degeneration analysis (number of total /degenerated neurons)**		
	0.5 mM	**1.5 mM**	**3.0 mM**	**0.5 mM**	**1.5 mM**	**3.0 mM**
VSOP-R1	n = 15	n = 14	n = 21	22 / 3 (n = 8)	12 / 7 (n = 6)	22 / 7 (n = 7)
VSOP-R2	n = 13	n = 12	n = 12	17 / 3 (n = 5)	30 / 7 (n = 6)	27 / 5 (n = 7)
Ferucarbotran	n = 12	n = 11	n = 16	21 / 6 (n = 8)	19 / 5 (n = 5)	25 / 6 (n = 7)
Ferumoxytol	n = 28	n = 17	n = 29	38 / 9 (n = 8)	30 / 8 (n = 6)	42 / 8 (n = 8)
Controls	n = 23			39 / 10 (n = 7)		

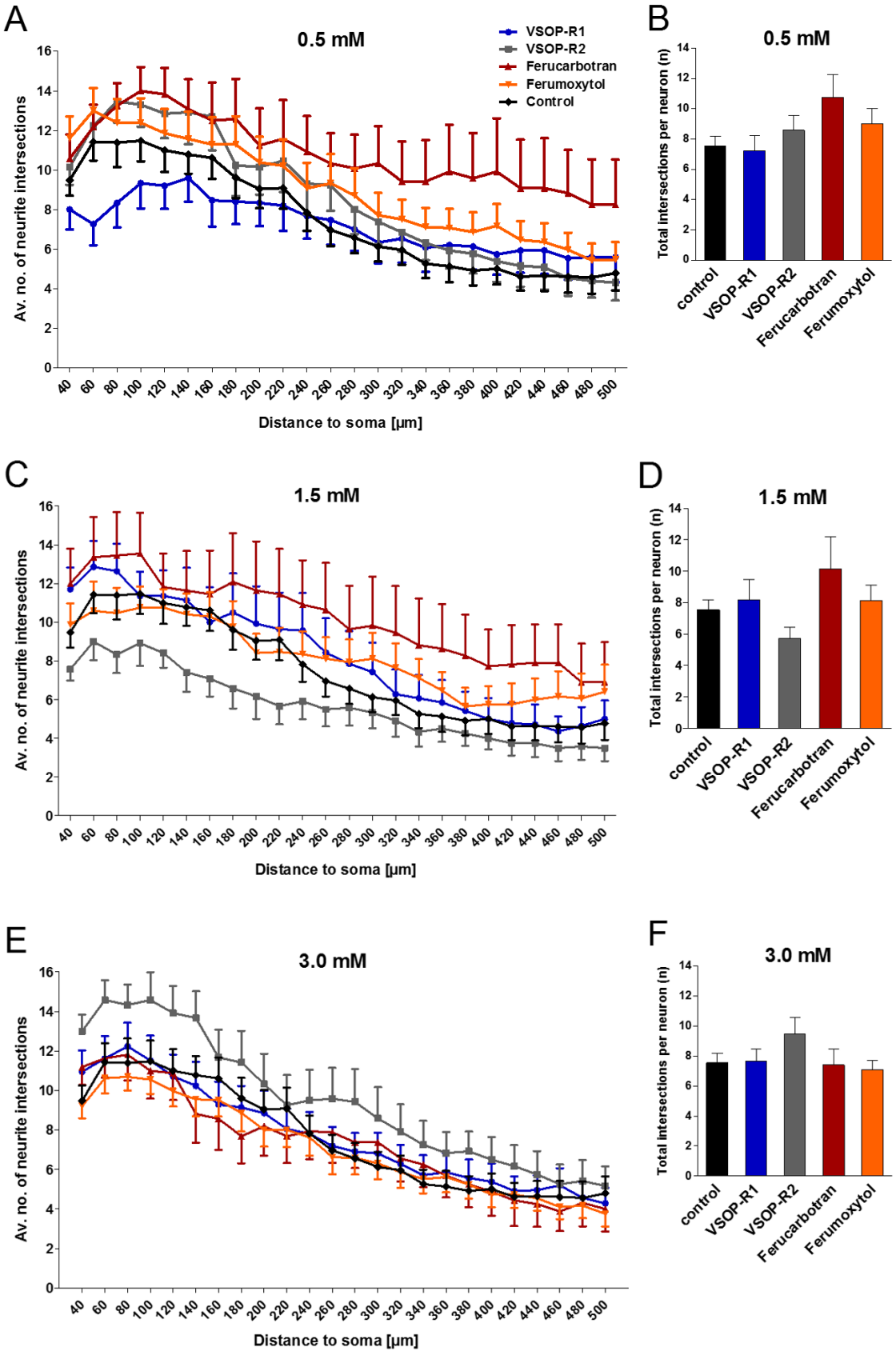

Figure 17: SPIOs exert contrary effects on neurites of neurons from neuron–glia co-cultures. Sholl profile of neurons form co-cultures (10 DIV) that were either untreated (control, black line) or incubated for 24 hours with concentrations of (A, B) 0.5 mM, (C, D) 1.5 mM) or (E, F) 3.0 mM of the indicated SPIOs. Untreated neurons are

referred to as control. (A, C, E) Average numbers of neurite intersections from 223 neurons in total were quantified by means of Sholl analysis and are depicted in increasing distance to the soma for each exposure condition. For clarity reasons, error bars are set to either below or above the intersection curves. Sholl analyses of neurons from co-cultures partially shows upwards shifted intersection curves that reflects increased numbers of neurites after SPIO exposure for 24 hours (coloured lines) compared to untreated neurons (black line). (B, D, F) Quantification of average numbers of total neurite intersections with concentric circles per neuron exposed to indicated SPIOs and concentrations, respectively. No significant differences compared to untreated neurons were found. Kruskal–Wallis one-way ANOVA and Dunn's multiple comparison post hoc test: (B) p = 0.3195; (D) p = 0.4032; (F) p = 0.4292.

Interestingly, Sholl analysis of primary neurons from co-cultures revealed contrary effects compared to neurons from monocultures, in both morphological alterations (Figure 17) and neuronal degeneration (Figure 18) using different SPIO concentrations (Neubert et al. 2015).

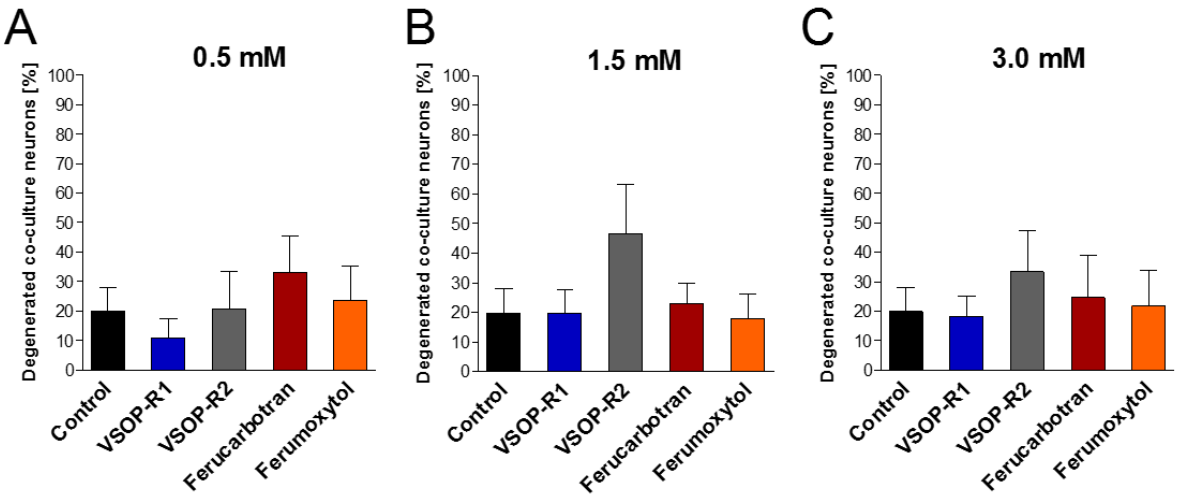

Figure 18: Neurons from neuron-glia co-cultures did not significantly degenerate after SPIO exposure. Numbers of degenerated neurons were manually counted in fluorescence microscopy following the exposure to (A) 0.5 mM, (B) 1.5 mM and (C) 3.0 mM of respective SPIOs. All values were normalized to untreated neurons (referred to as (control) and are displayed as percentage. Quantification of the percentage of degenerated neurons exposed to various particle concentrations did not show significant differences when compared to untreated neurons. However, numbers of degenerated neurons incubated with (B) 1.5 mM of VSOP-R2 were more than twice as high compared to controls. Kruskal–Wallis one-way ANOVA and Dunn's multiple comparison post hoc test: (A) p = 0.6719; (B) p = 0.6069; (C) p = 0.9260.

Using Sholl analysis, I predominantly found increased numbers of neurite intersections of SPIO-exposed neurons (Figure 17A, C, and E, coloured lines) compared to untreated neurons from neuron-glia co-cultures (Figure 17, C, and E, black lines). Co-cultured neurons incubated for 24 hours with iron concentrations of 0.5 mM of VSOP-R2, ferucarbotran and ferumoxytol but not VSOP-R1 showed increased numbers of neurite intersections (Figure 17A and B). Neurons exposed to 0.5 mM of VSOP-R1 (Figure 17A) showed slightly reduced numbers of neurites proximally to cell somata when compared to untreated neurons. Except for 3.0 mM of VSOP-R2 (Figure 17E and F), neurons exposed to SPIO concentrations of 3.0 mM

possessed similar numbers of neuronal processes (Figure 17E and F) in comparison to untreated neurons (Figure 17E and F). In contrast, exposure of neurons to for 3.0 mM of VSOP-R2 led to an increase in number of neurites (Figure 17E and F), whereas a concentration of 1.5 mM of this nanoparticle resulted in a reduction in neurite numbers (Figure 17C and D). In principle, I counted more neuronal processes with increasing SPIO concentrations, which is reflected by approximating intersection curves of particle-exposed compared to untreated neurons (Figure 17C-F). However, the numbers of neurons from neuron-glia co-cultures that I was able to use for Sholl analysis (Table 5) were much less compared to numbers of neurons from monocultures (Table 4) and variations in neurite morphology were high (Figure 17). Consequently, the average number of neurite intersections per exposure condition did not reveal significant differences compared to untreated control neurons (Figure 17B, D and F).

The data from the quantification of average numbers of neurite intersections using Sholl analysis (Figure 17B, D and F) were according to the results from degeneration analysis (Figure 18). The quantification of numbers of degenerated neurons revealed slightly increased numbers of degenerated neurons from co-cultures after exposure to concentrations of 0.5 mM of ferucarbotran (Figure 18A) and 3.0 mM of VSOP-R2 (Figure 18C) compared to controls (Figure 18A-C). Under these exposure conditions, however, neurons showed increased numbers of neurites (Figure 17B, D and F) with the exception of 1.5 mM VSOP-R2 (Figure 18B). Numbers of degenerated neurons incubated with 1.5 mM of VSOP-R2 were more than twice as high as numbers of degenerated controls (Figure 18B). This is in accordance with Figure 17B, D and F, which shows decreased numbers of neurites for neurons incubated with 1.5 mM of VSOP-R2. However, I did not find significant differences in numbers of degenerated neurons incubated with SPIOs in all concentrations compared to untreated cells (Figure 18A, B, and C).

These data show that neurons in neuron-glia co-culture do not substantially degenerate after SPIO exposure compared to neurons from monoculture (Neubert et al. 2015).

3.3 SPIOs do not significantly modulate cytokine and chemokine secretion of brain cells in culture

In neuron-glia co-cultures it became apparent that SPIO-mediated effects may be influenced by the interaction of the different cell types. Neurons specifically communicate with glial cells in a bidirectional manner via the release of signalling molecules and in turn, influence, the state of activation of microglia (Biber et al. 2007; Hanisch and Kettenmann 2007; Eyo and Wu 2013). Slight deviations in molecule secretion caused by impaired neuronal function or atrophy can either result in neurotoxic or neuroprotective microglial responses mediated through the release of pro- or anti-inflammatory cytokines and chemokines (von Zahn et al. 1997; Biber et al. 2007; Napoli and Neumann 2009; Walter and Neumann 2009). Therefore, I performed a screening for 40 different cytokines and chemokines in cell culture supernatants of microglia, astrocytes and neurons as well as neuron-glia co-cultures using the Proteome Profiler Mouse Array Kit, Panel A (ARY006; R&D Systems). As I found increased neurite branching of neurons from neuron-glia co-cultures, especially, after the exposure to SPIO concentrations of 0.5 mM for 24 hours, I used supernatants

of all cultures under these experimental conditions as well as of untreated cell cultures and performed measurements in triplicate, respectively. Before measuring the relative expression of cytokines and chemokines, I incubated the Array Kit nitrocellulose membranes with cell culture respective supernatants for chemiluminescence detection. I quantified the chemiluminescence signals of individual nitrocellulose membranes using ImageJ software. Subsequently, I averaged the quantified mean grey-value intensities of duplicate spots that represent one of the 40 different cytokines/chemokines and normalized these with averaged values of reference spots in corresponding images. Data were compared with GraphPad Prism 5 software.

The quantification of mean grey-value intensities of all measured cytokines and chemokines did not reveal significant differences, neither in comparison of VSOP-R1, VSOP-R2, ferucarbotran and ferumoxytol in respective cell cultures, nor in comparison between microglial, astrocyte and neuronal cultures. However, I observed exceptionally increased or decreased expression levels when comparing certain mean grey-value intensities of cytokines and chemokines that originate from supernatants of cell cultures exposed to different SPIO types. For instance, microglia exposed to 0.5 mM of VSOPs and ferumoxytol for 24 hours show strongly increased expression of the chemokine CCL4 compared to the same concentration of ferucarbotran and astrocyte and neuronal cultures.

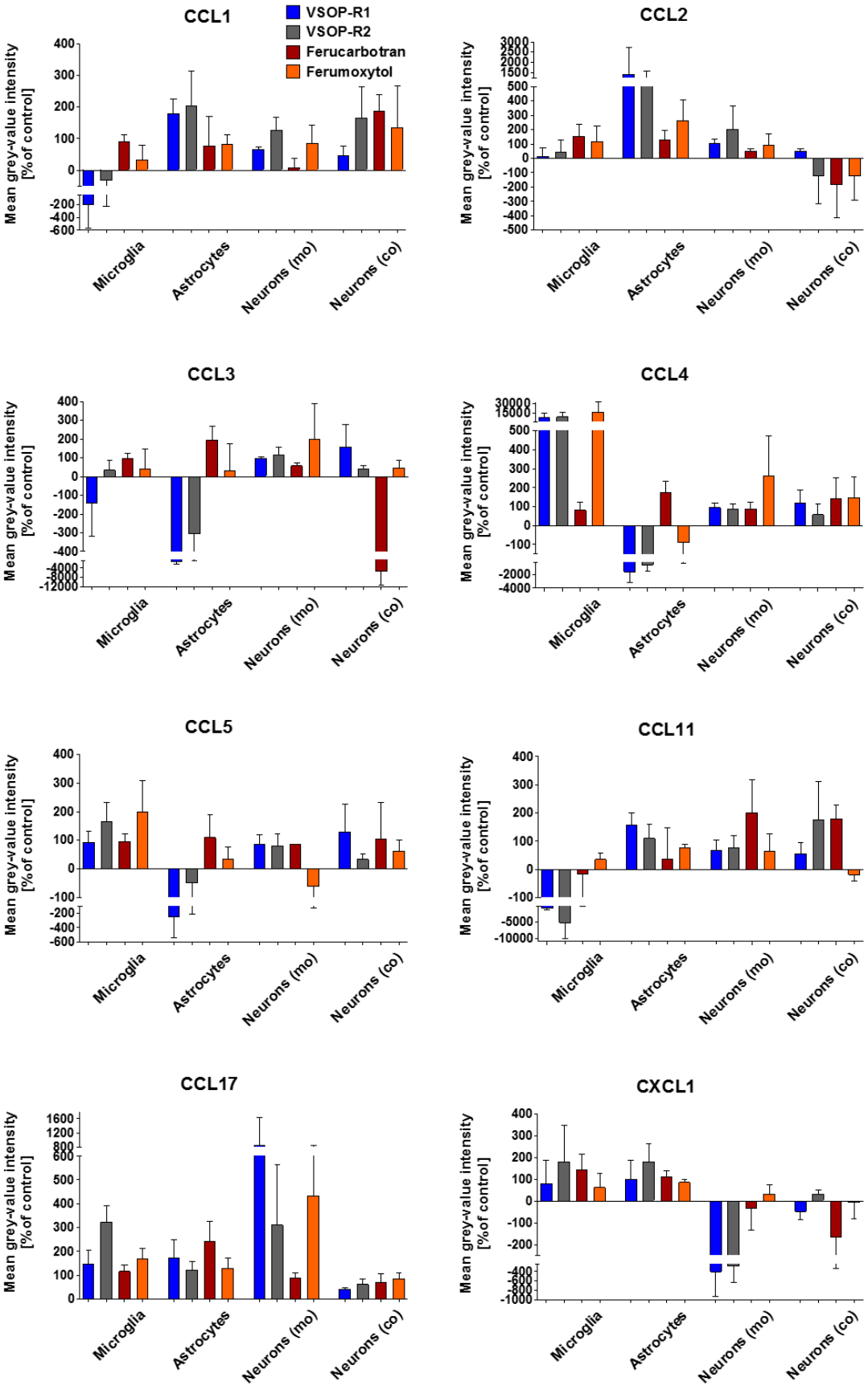
CCL1
VSOP-R1
VSOP-R2
Ferucarbotran
Ferumoxytol
CCL2
CCL3
CCL4
CCL5
CCL11
CCL17
CXCL1
Mean grey-value intensity [%of control]
Microglia
Astrocytes
Neurons (mo)
Neurons (co)

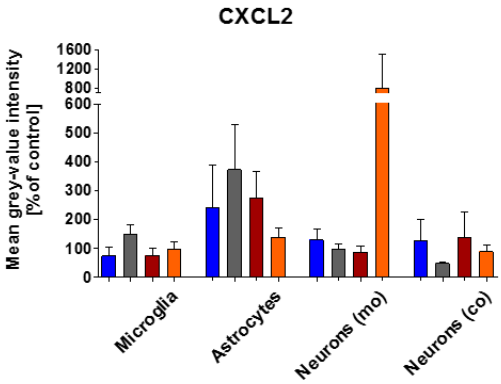
CXCL2
Mean grey-value intensity [% of control]
1600
1200
800
600
500
400
300
200
100
0
Microglia
Astrocytes
Neurons (mo)
Neurons (co)

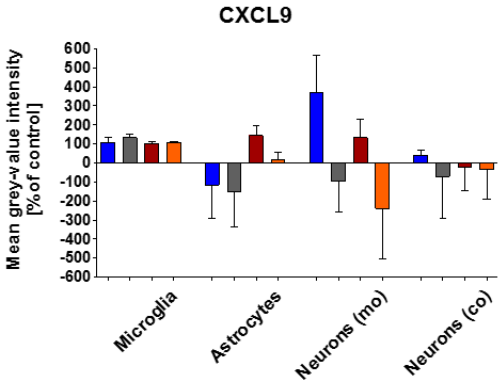
CXCL9
Mean grey-value intensity [% of control]
600
500
400
300
200
100
0
-100
-200
-300
-400
-500
-600
Microglia
Astrocytes
Neurons (mo)
Neurons (co)

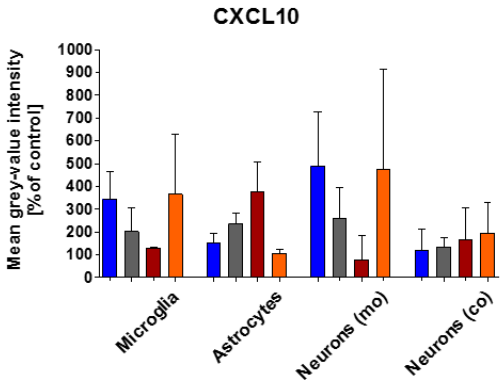
CXCL10
Mean grey-value intensity [% of control]
1000
900
800
700
600
500
400
300
200
100
0
Microglia
Astrocytes
Neurons (mo)
Neurons (co)

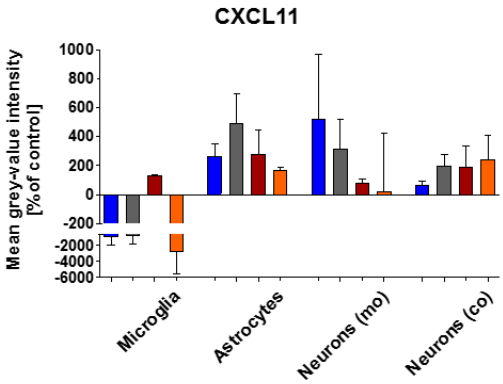
CXCL11
Mean grey-value intensity [% of control]
1000
800
600
400
200
0
-200
-2000
-4000
-6000
Microglia
Astrocytes
Neurons (mo)
Neurons (co)

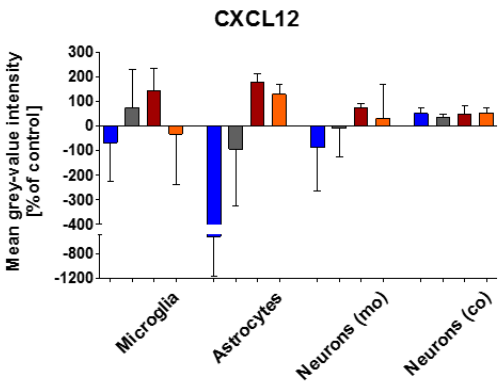
CXCL12
Mean grey-value intensity [% of control]
300
200
100
0
-100
-200
-300
-400
-800
-1200
Microglia
Astrocytes
Neurons (mo)
Neurons (co)

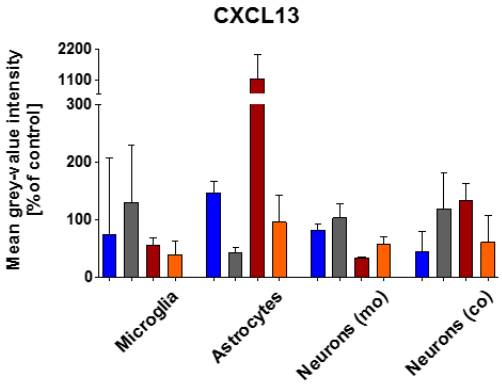
CXCL13
Mean grey-value intensity [% of control]
2200
1100
300
200
100
0
Microglia
Astrocytes
Neurons (mo)
Neurons (co)

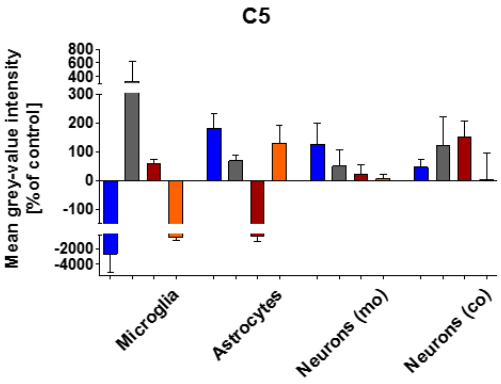
C5
Mean grey-value intensity [% of control]
800
600
400
300
200
100
0
-100
-2000
-4000
Microglia
Astrocytes
Neurons (mo)
Neurons (co)

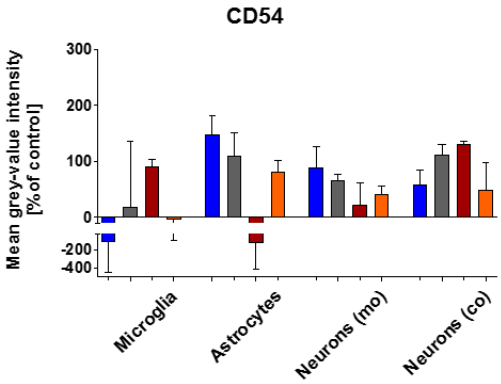
CD54
Mean grey-value intensity [% of control]
300
200
100
0
-200
-400
Microglia
Astrocytes
Neurons (mo)
Neurons (co)

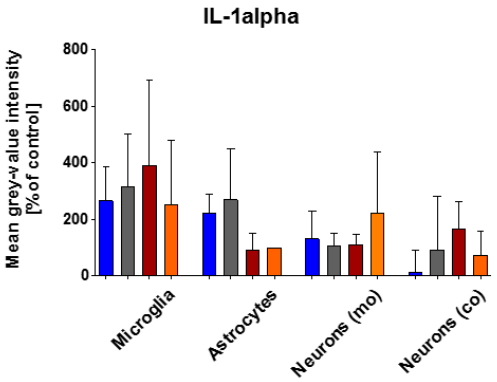
IL-1alpha
Mean grey-value intensity [% of control]
800
600
400
200
0
Microglia
Astrocytes
Neurons (mo)
Neurons (co)

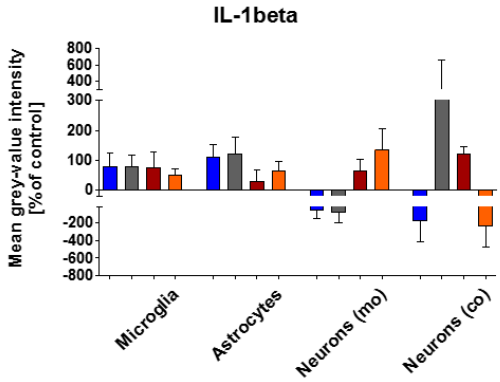
IL-1beta
Mean grey-value intensity [% of control]
800
600
400
300
200
100
0
-200
-400
-600
-800
Microglia
Astrocytes
Neurons (mo)
Neurons (co)

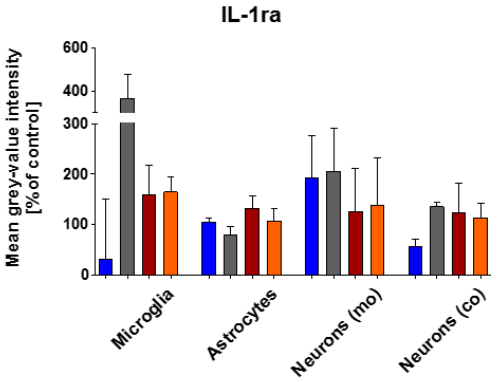
IL-1ra
Mean grey-value intensity [% of control]
600
400
300
200
100
0
Microglia
Astrocytes
Neurons (mo)
Neurons (co)

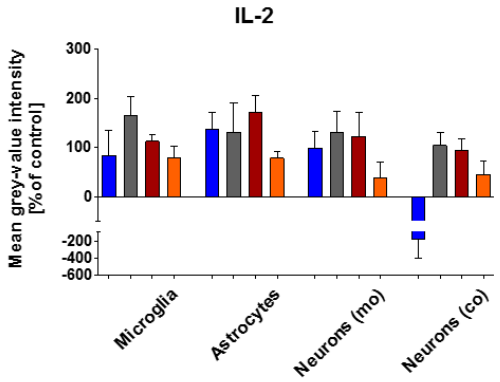
IL-2
Mean grey-value intensity [% of control]
300
200
100
0
-200
-400
-600
Microglia
Astrocytes
Neurons (mo)
Neurons (co)

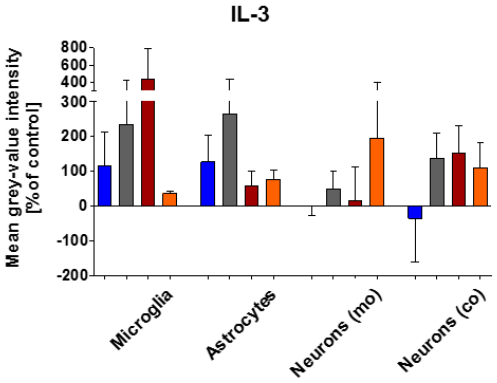
IL-3
Mean grey-value intensity [% of control]
800
600
400
300
200
100
0
-100
-200
Microglia
Astrocytes
Neurons (mo)
Neurons (co)

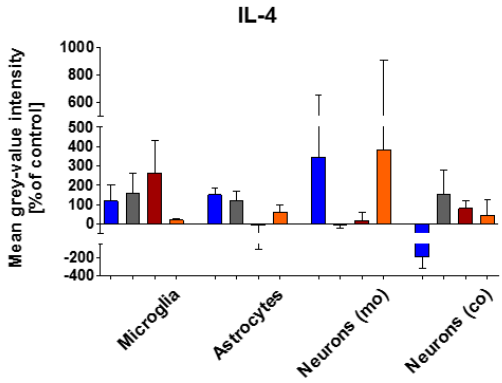
IL-4
Mean grey-value intensity [% of control]
1000
800
600
500
400
300
200
100
0
-200
-400
Microglia
Astrocytes
Neurons (mo)
Neurons (co)

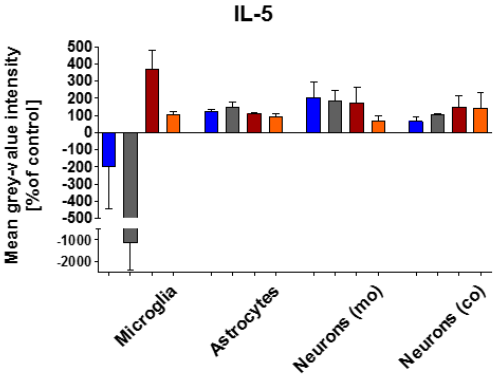
IL-5
Mean grey-value intensity [% of control]
500
400
300
200
100
0
-100
-200
-300
-400
-500
-1000
-2000
Microglia
Astrocytes
Neurons (mo)
Neurons (co)

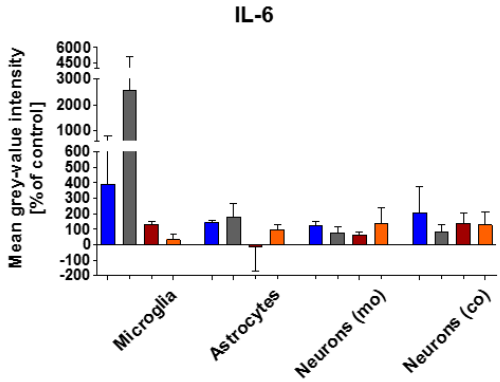
IL-6
Mean grey-value intensity [% of control]
6000
4500
3000
2000
1000
600
500
400
300
200
100
0
-100
-200
Microglia
Astrocytes
Neurons (mo)
Neurons (co)

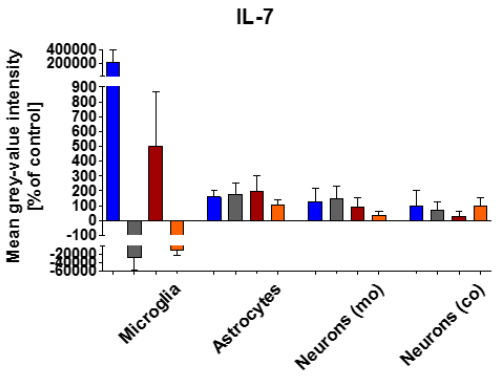
IL-7
Mean grey-value intensity [%of control]
Microglia
Astrocytes
Neurons (mo)
Neurons (co)

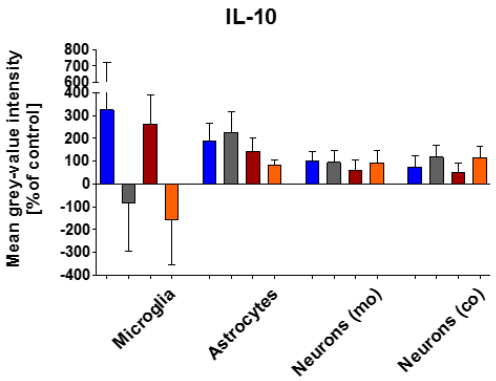
IL-10
Mean grey-value intensity [%of control]
Microglia
Astrocytes
Neurons (mo)
Neurons (co)

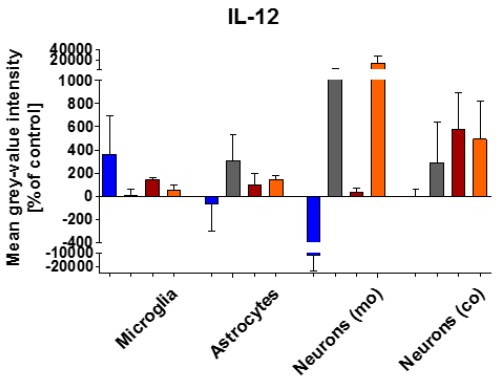
IL-12
Mean grey-value intensity [%of control]
Microglia
Astrocytes
Neurons (mo)
Neurons (co)

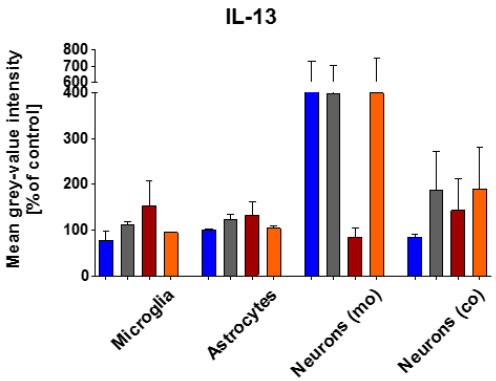
IL-13
Mean grey-value intensity [%of control]
Microglia
Astrocytes
Neurons (mo)
Neurons (co)

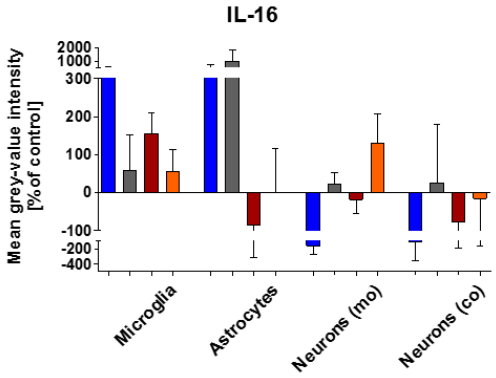
IL-16
Mean grey-value intensity [%of control]
Microglia
Astrocytes
Neurons (mo)
Neurons (co)

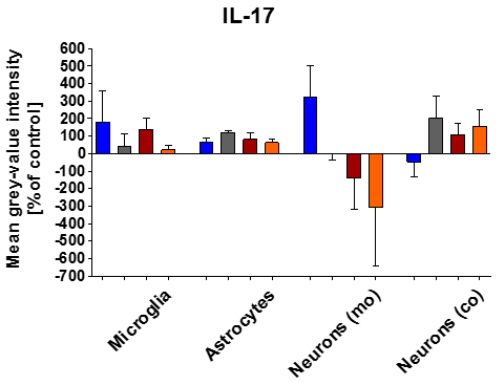
IL-17
Mean grey-value intensity [%of control]
Microglia
Astrocytes
Neurons (mo)
Neurons (co)

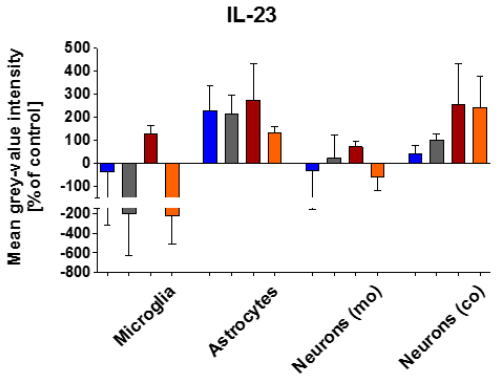
IL-23
Mean grey-value intensity [%of control]
Microglia
Astrocytes
Neurons (mo)
Neurons (co)

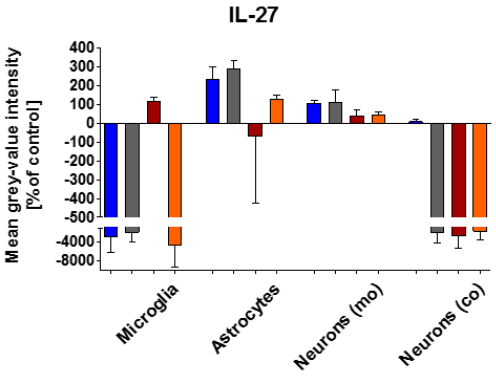
IL-27
Mean grey-value intensity [%of control]
Microglia
Astrocytes
Neurons (mo)
Neurons (co)

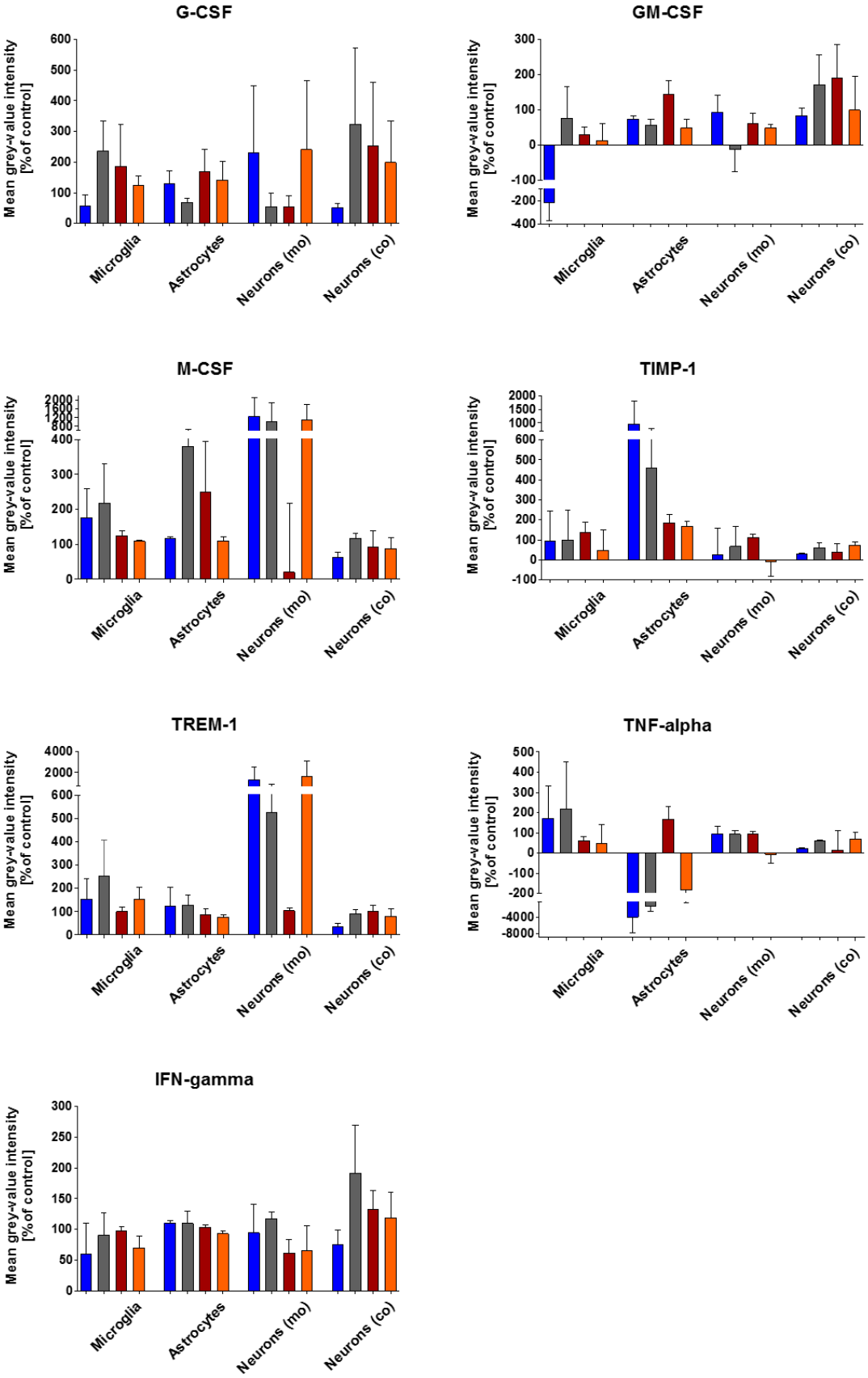

Figure 19: Cytokine and chemokine secretion profile of primary brain cells. The secretion of cytokines and chemokines in respective cell culture supernatants was analysed using the Proteome Profiler Mouse Array Kit Panel A (ARY006, R&D Systems), where capture antibodies for 40 different cytokines and chemokines are spotted in duplicate.

Quantification of detected cytokines/ chemokines via chemiluminescence was performed using ImageJ. Averaged mean grey-value intensities of duplicate spots were normalized to averaged values of reference spots and, subsequently, to averaged values of untreated controls, respectively. Mean grey-value intensities for each cytokine and chemokine are shown as percentage of controls. Although the cytokine and chemokine profile shows either strongly increased or decreased mean grey-value intensities, no significant differences of their secretion within respective cell cultures and in comparison between the four different cultures were found. Variation in measurements are presented as SEM.

4 Discussion

The aim of this thesis was to investigate the consequences of the clinically approved MRI contrast agents ferucarbotran and ferumoxytol in addition to two types of VSOPs that entered clinical phase II trials on murine primary brain cells. The capacity of SPIOs to penetrate the intact BBB depending on their composition, including size, surface coating and charge, which is further facilitated by an external magnetic field (Lockman et al. 2004; Kim et al. 2006; Wang et al. 2010; Kong et al. 2012; Hoff et al. 2013; Thomsen et al. 2013; Sun et al. 2014) elucidates the necessary requirement to test for potential cytotoxic effects associated with respective SPIO compositions. My work indicates that SPIO size, surface coating and charge have substantial influence on the cellular response of brain cells, which highlights the unique effect of SPIO compositions. The probability of brain cells to encounter SPIOs is tremendously increased when these particles are systemically administered for diagnosis under neuroinflammatory conditions with dysfunctional BBB (Weinstein et al. 2010; Gendelman et al. 2015; Silva Adaya et al. 2017). Here, different types of SPIOs have been reported to be transported into the brain, for instance, by leukocytes that phagocytosed particles (Petry et al. 2007; Weinstein et al. 2010; Weise and Stoll 2012; Krol et al. 2013). Nevertheless, even the guidelines of the International Conference for Harmonization for drug development, which also accounts for SPIO-based contrast agents merely assess the survival of animals or cells in culture in order to address potential toxicity (Safety Guidelines of the International Conference for Harmonization ; Neubert et al. 2015). Serious concerns about SPIO-induced neurotoxic effects have been raised (Oberdorster et al. 2009; Hu and Gao 2010; Cupaioli et al. 2014; Migliore et al. 2015; Jarockyte et al. 2016).

There are studies available in the literature that already investigated particle-cell interactions, cytotoxicity, and degradation of SPIOs of various composition (Pisanic et al. 2007; Hong et al. 2011; Kim et al. 2011; Soenen et al. 2011). However, first of all, most of the applied nanoparticles where specifically designed to explore various processes, like iron oxide metabolism and fate following cellular uptake by primary brain cells (C. et al. 2010; Geppert et al. 2011; Geppert et al. 2012; Hohnholt and Dringen 2013; Luther et al. 2013; Petters et al. 2014; Petters et al. 2016). When applying clinically relevant SPIOs, exposure-induced effects were predominantly assessed using immortalized cell lines (Cengelli et al. 2006; Soenen et al. 2010b; Soenen et al. 2011; Rosenberg et al. 2012), which only provide limited informative value. Immortalized cells show altered physiological properties, including proliferation, survival, differentiation and activated states compared to the corresponding primary cell types (Jenkins et al. 2013). They are more resistant to adverse stimuli and have been shown to take up SPIOs much stronger than, for instance, primary cerebellar neurons (Pinkernelle et al. 2012; Jenkins et al. 2013). Consequently, interpretation of results with regard to affected cellular morphology, cell viability and metabolism of SPIO-exposed immortalized cell lines should be treated with caution.

In order to study the impact of SPIO exposure on the viability of brain cells, the use of primary cell culture models cultivated under controlled conditions is a suitable approach. Assessing individual cells in culture has the advantage to observe early signs of adverse SPIO effects that can be reflected by morphological transformation of microglia from a ramified towards an amoeboid phenotype and cytoskeletal disruptions

of neurons (Valdiglesias et al. 2015). The neurotoxic potential of different types of nanoparticles has already been demonstrated using various approaches and is currently of major concern, not only in the field of biomedicine (Nel et al. 2006; Buzea et al. 2007; Hu and Gao 2010; Yang et al. 2010; Cupaioli et al. 2014; Migliore et al. 2015; Valdiglesias et al. 2015; Jarockyte et al. 2016). For instance, intranasal inhaled nanoparticles were found to be transported into the brain by olfactory nerves after being deposited in the olfactory bulb (Wang et al. 2011; Wu et al. 2013b). Consequently, high particle concentrations were found in the striatum and hippocampus, which are both regions affected in neurodegenerative diseases (Hu and Gao 2010; Migliore et al. 2015; Valdiglesias et al. 2015).

The question remains, however, which concentrations of the intravenously administered SPIOs eventually reach the brain parenchyma. Most available studies applied particle iron concentrations to cultured cells that are not comparable to SPIO doses that eventually reach the brain (Table 7 – 9). Therefore, iron concentration range of SPIOs used in this thesis were selected based on the following calculations. For VSOP injections in humans, it has been shown that a dose of 0.075 mM iron/kg (1.34 mg iron/kg) body weight leads to a plasma concentration of 90 mg/l iron or approximately 1.6 mM iron plasma concentration (Taupitz et al. 2004), which is according to the SPIO concentration used in this study (Neubert et al. 2015). With regard to the clinically applied bolus dose of 510 mg ferumoxytol, an amount of 8.5 mg iron/kg body weight for a person weighing 60 kg can be assumed (Lu et al. 2010; Pai et al. 2010; Toth et al. 2017). Hence, ferumoxytol administration could result in a plasma iron concentration of approximately 10.0 mM, which is three times higher than the highest iron concentration of 3.0 mM used in the presented experimental approach. Based on those results, the applied particle concentrations of 0.5 mM, 1.5 mM and 3.0 mM are within the range of clinical relevant doses. In addition, previous studies have demonstrated that 30 % of applied SPIOs (30 % of 1.6 mM: ~0.5 mM and 30% of 10.0 mM: ~3.0 mM) can penetrate the BBB (Kong et al. 2012; Dan et al. 2013; Hoff et al. 2013; Thomsen et al. 2013; Sun et al. 2014). Due to these calculations on the available data, brain cells were exposed with SPIOs of clinically relevant doses (Neubert et al. 2015).

4.1 Consequences of SPIO exposure on glial cells

Several reports have addressed the interaction, including uptake and metabolism of iron oxide nanoparticles with primary astrocytes (Au et al. 2007; Geppert et al. 2009; Ding et al. 2010; Geppert et al. 2011; Lamkowsky et al. 2011; Geppert et al. 2012; Hohnholt and Dringen 2013; Hohnholt et al. 2013; Sun et al. 2013; Schaub et al. 2014; Migliore et al. 2015; Petters et al. 2016). Due to their close proximity to the brain microvasculature, essential function in brain iron metabolism und metabolic support of neurons, the effect of SPIOs on astrocytes have been extensively investigated. As neuron-glial co-cultures used in my investigations are composed of astrocytes, SPIO-induced effects will be described in the following.

4.1.1 Effects of SPIOs on primary astrocytes

Due to their major role in iron metabolism of the brain, astrocytes are capable of buffering iron overload as a consequence of SPIO exposure and protect neurons from iron-mediated toxicity and oxidative stress

(Tiffany-Castiglion and Qian 2001; Dringen et al. 2007; Macco et al. 2013; Pelizzoni et al. 2013; Liu et al. 2017). So far, previous studies investigated the effects on astrocyte physiology using various SPIO types (Table 7). The applied SPIOs were found to be internalized by clathrin-mediated endocytosis and macropinocytosis following their attachment to the cell membrane (Hohnholt and Dringen 2013; Petters et al. 2016). Here, the surface charge of SPIOs decisively influenced their uptake, whereas positively charged particles were taken up superior to negatively charged SPIOs (Hohnholt and Dringen 2013; Sun et al. 2013). Following uptake, SPIOs were localized into lysosomes, where the acidic pH and reducing compounds facilitated particle degradation and liberation of iron ions (Levy et al. 2010; Hohnholt et al. 2013). SPIO-derived iron ions are thought to be stored in ferritin after their transport into the cytosol by the divalent metal transporter 1 (DMT1) (Hohnholt and Dringen 2013; Petters et al. 2016).

The uptake of DMSA- and dextran-coated iron oxide nanoparticles by astrocytes *in vitro* was shown to depend on particle concentration, exposure time and temperature (Ding et al. 2010; Geppert et al. 2011; Lamkowsky et al. 2012). However, incubation with these types of SPIOs did not impair cell viability (Table 7). Instead, astrocytes appeared to be resistant against iron induced toxicity, putatively due to the storage of particle-derived excess iron in ferritin (Geppert et al. 2009; Geppert et al. 2012). However, a slow liberation of iron ions from accumulated DMSA-coated particles induced the generation of reactive oxygen species (ROS) and, hence, delayed decrease in cell viability (Geppert et al. 2012). SPIOs coated with different materials, such as aminosilane and starch were found to induce cytotoxicity depend on the applied concentration (Au et al. 2007; Sun et al. 2013). In addition, SPIO uptake significantly increased when cells were exposed to a magnet (Lamkowsky et al. 2012; Sun et al. 2013; Schaub et al. 2014). These results emphasize the importance to investigate SPIO-induced effects with regard to particle size and surface properties and respective experimental condition.

Table 7: Studies on the effects of SPIOs on primary astrocytes *in vitro*.

SPIO characteristics	Exposure condition	Effects on primary astrocytes	Reference
Fe_3O_4 or ɣ-Fe_2O_3 (exact composition not disclosed)	10 µg/ml for 6 h	Membrane integrity not affected Significantly impaired viability	(Au et al. 2007)
Dextran-coated Fe_3O_4 **2 – 6 nm**	32, 64 and 128 µg/ml for 24 h	No influence on proliferation No cytotoxicity	(Ding et al. 2010)
DMSA coated ɣ-Fe_2O_3 **Anionic charge** **60 nm**	500 and 1000 µM for up to 6 h	No acute cell death within 6 h No changes in viability Time- and concentration-dependent SPIO accumulation	(Geppert et al. 2011)
DMSA coated ɣ-Fe_2O_3 **Anionic charge** **60 nm**	0.25, 1 and 4 mM for 4 h	No changes in viability after 4 h but after 7 days post incubation No alteration in cell metabolism Dose-dependent increases in iron content and slight increase in ROS	(Geppert et al. 2012)
DMSA coated ɣ-Fe_2O_3 **Anionic charge** **60 nm**	1 and 4 mM for 4 h at 4 °C or 37°C	No changes in viability External magnetic field-induced acceleration of particle uptake in time, temperature and concentration dependency	(Lamkowsky et al. 2012)
Aminosilane (AmS)-coated (cationic charge) and **Carboxyl-AmS-coated Fe_3O_4 (anionic charge)** **27 nm**	0.1 – 224 µg/mL for 24 h	Cytotoxicity above 100 µg/ml SPIO concentration, especially of COOH-AmS- Fe_3O_4 in the presence of a magnetic field Strong SPIO uptake	(Sun et al. 2013)
AmS-coated (50 and 100 nm) and **Starch- (50 nm) coated SPIOs**	0.25, 1.25 and 2.5 mg/ml for 24 or 72 h	Altered viability in presence of alternating magnetic field induced cell death	(Schaub et al. 2014)
Fluorescent DMSA-coated ɣ-Fe_2O_3 **Anionic charge** **42 – 49 nm**	0.1, 0.3, 1.0 and 3.0 mM for 6 h and 0.3 mM for 24 h	No influence on viability Slight increase in ROS	(Petters et al. 2016)

4.1.2 Effects of SPIOs on microglial cells

Apart from this thesis that includes already published results (Neubert et al. 2015), only a few number of studies investigated the effects of SPIOs of primary microglial cells (Xue et al. 2012; Luther et al. 2013; Wu et al. 2013a; Petters et al. 2016). An overview of the previous studies is given in Table 8. None of the applied SPIOs have been investigated to this extend concerning their influence on the morphology and viability of primary microglia. Most available studies using different model systems have demonstrated that microglia are capable of engulfing various types nanoparticles (Fleige et al. 2001; Tysiak et al. 2009; Pickard and Chari 2010; Wang et al. 2011; Pinkernelle et al. 2012; Luther et al. 2013; Millward et al. 2013). Furthermore, several reports have shown that microglia become activated upon nanoparticle exposure, which was, in some cases, accompanied by the release pro-inflammatory and potentially neurotoxic mediators, such as NO, TNF-α and ROS (Table 8) (Wang et al. 2011; Xue et al. 2012; Wu et al. 2013a; Cupaioli et al. 2014). For instance, intranasal exposure of maghemite nanoparticles caused microglial activation and generation of ROS and NO, leading to pathological tissue alterations of the olfactory bulb, hippocampus and striatum in mice (Wang et al. 2011). Although the subsequent effects of peripherally applied nanoparticles are not directly comparable to effects of systemically injected SPIOs, these results indicate that particle-induced microglial activation might have detrimental impact (Minghetti et al. 2005; Kierdorf and Prinz 2013; Sierra et al. 2013). However, results of previous studies were conflicting concerning microglial activation (Pickard and Chari 2010; Luther et al. 2013) and activation-induced secretion of pro-inflammatory mediators TNF-α, IL-1β, IL-6, ROS and NO (Table 8) (Cengelli et al. 2006; Wang et al. 2011; Xue et al. 2012; Ye et al. 2013). Two studies reported a decrease in viability of primary microglia following the exposure to anionic DMSA-coated SPIOs (Luther et al. 2013; Petters et al. 2016). These data demonstrate that microglial reactions following SPIO exposure strongly depend on nanoparticle size, surface coating and charge and are further influenced by the applied cell culture model. Consequently, understanding the reaction of primary microglia to clinically applied SPIOs and estimating a potential induction of neurodegeneration by activated microglia remained to be explored.

Table 8: Studies on the effects of SPIOs on microglial cells *in vitro*.

Microglial cells	SPIO characteristics	Exposure condition	Effects on microglial cells	Reference
Murine microglial N9 and N11 cells	Dextran-coated Endorem® (80 – 150 nm) & Sinerem® (15 – 30 nm) with neutral charge PVA-SPIOs (neutral) Amino-PVA-SPIOs (anionic) Carboxy-PVA-SPIOs (cationic) Thiol-PVA-SPIOs (cationic) 30 nm	0.4, 1.8 and 3.5 mM for 2 – 35 h	No cytotoxicity or NO production Low and slow uptake of dextran-coated SPIOs increasing over time Time- and concentration-dependent uptake of amino-PVA-SPIOs	(Cengelli et al. 2006)
Murine microglial Bv-2 cells	α-Fe_2O_3 (143 nm), ɣ-Fe_2O_3 (644 nm)	0.02, 0.2 and 2 mmol/L for 2 – 12 h	No significant cytotoxicity, Viability recovered after 12 h No significant increase in IL-1β, IL-6 and TNF-α Increase ROS and NO production	(Wang et al. 2011)
Murine microglial Bv-2 cells	Dextran-coated ferumoxide (Feridex®) Anionic charge 80 –150 nm	11.2, 22.4 and 56 µg iron for 6 h	No influence on viability Dose-dependent increase in iron concentration	(Rosenberg et al. 2012)
Primary microglia (rat)	Fe_3O_4 (exact composition not disclosed) 45 nm	0.25 and 0.5 mg/ml for 24 h	No increase in NO production Mild increase in IL-1β, IL-6 and TNF-α release independent from the dose	(Xue et al. 2012)
Primary microglia (mice)	Carboxydextran-coated ferucarbotran (Resovist®) Anionic charge 45 – 60 nm	1, 10 and 50 µg/ml for 30 min, stimulated with 100 ng/ml LPS for 24 h	No influence on viability and morphology LPS + SPIO attenuated IL-1β but not TNF-α production	(Wu et al. 2013a)

Microglial cells	SPIO characteristics	Exposure condition	Effects on microglial cells	Reference
Primary microglia (rat)	Fluorescent DMSA-coated ɣ-Fe_2O_3 Anionic charge 60 – 70 nm	150, 450 and 1500 µM for 3 and 6 h	Time-, concentration- and temperature-dependent SPIO uptake Severely affected cell viability at high concentrations and prolonged exposure	(Luther et al. 2013)
Primary microglia (rat)	Fluorescent DMSA-coated ɣ-Fe_2O_3 Anionic charge 42 – 49 nm	0.1, 0.3, 1.0 and 3.0 mM for 6 h and 0.3 mM for 24 h	Severe concentration-dependent increase in iron content, ROS and cytotoxicity	(Petters et al. 2016)

In this thesis, I showed that microglia undergo morphological transformation indicative for microglial activation after exposure to clinically relevant SPIOs (Neubert et al. 2015), which has not been demonstrated for these nanoparticles and applied iron concentrations before. The activation process of microglia involves morphological transformation from a resting, meaning constantly surveilling towards an executive state, which is accompanied by a gradual de-ramification of the highly motile processes, expanded soma and overall enlargement of the cell body, resulting in an amoeboid-shaped phenotype (Town et al. 2005; Hanisch and Kettenmann 2007; Walker et al. 2014). Activated microglia also become highly phagocytic (Fleige et al. 2001; Wang et al. 2011; Walker et al. 2014), which accounts for the increased accumulation of VSOPs and ferucarbotran but not ferumoxytol. These characteristic morphological and functional criteria of microglia can be observed for the *in vitro* just as for the *in vivo* phenotype and are considered as reliable indicators for their activation (Napoli and Neumann 2009; Ransohoff and Perry 2009; Walker et al. 2014). In Prussian blue staining (Figure 2), I already observed clear indications for microglial activation upon accumulation of VSOPs and ferucarbotran with increasing iron concentrations and prolonged exposure time, which I confirmed with immunocytochemical staining (Figure 4) (Neubert et al. 2015). These observations were also confirmed in immunocytochemical staining for the exposure of microglia to carboxymethyldextran-coated ferumoxytol of neutral surface charge but were by far not as distinct as for the negatively charged VSOPs and ferucarbotran. However, my results are not in line with previous reports concerning SPIO-induced microglial activation (Pickard and Chari 2010; Luther et al. 2013). This is due to the fact that SPIOs of various composition were applied, leading to divergent observations with regard to cellular effects and cytotoxicity (Karlsson et al. 2009; Hong et al. 2011; Horie et al. 2012; Saito et al. 2012; Hirsch et al. 2013). Upon exposure, microglia effectively and avidly accumulated SPIOs of negative surface charge, whereby cellular accumulation of VSOPs appeared to be much faster and quantitatively superior (Neubert et al. 2015).

The accumulation and subsequent internalization of nanoparticles has been shown to depend on their physicochemical properties, including size, surface coating and charge (Wilhelm et al. 2003; Zhang et al.

2009; Verma and Stellacci 2010; Horie et al. 2012; Saito et al. 2012; Schweiger et al. 2012; Hirsch et al. 2013; Horie et al. 2013; Petters et al. 2014). Especially, the surface charge has been shown to influences particle-cell interactions and subsequent uptake (Wilhelm et al. 2003; Schweiger et al. 2012). Cell membranes constitute selectively permeable barriers, consisting of a phospholipid bilayer with embedded proteins as well as transport channels that exhibit large negatively charged domains. Positively charged SPIOs have been shown to electrostatically interact with the negatively charged glycocalyx forming clusters at the plasma membrane that are, subsequently, internalized by clathrin-mediated or adsorptive endocytosis (Wilhelm et al. 2003; Zhang et al. 2009; Verma and Stellacci 2010; Schweiger et al. 2012; Sun et al. 2013; Petters et al. 2014). Thus, adsorption of cationic particles is likely independent on the cell type (Wilhelm et al. 2003; Valdiglesias et al. 2015). In contrast, anionic particles are repelled by electrostatic repulsion at the plasma membrane, however, have been shown to be strongly internalized by different cell types (Mailander et al. 2008; Verma and Stellacci 2010; Andreas et al. 2012; Schweiger et al. 2012). I confirmed these findings for primary microglia, showing that both SPIOs of anionic surface charge, namely citrate-coated VSOPs and carboxydextran-coated ferucarbotran were efficiently accumulated (Neubert et al. 2015). In the case of ferucarbotran, the negatively charged carboxyl groups have been shown to enhance particle internalization by macrophages at iron concentrations of 1.5 mM (Wilhelm et al. 2003; Mailander et al. 2008; Andreas et al. 2012). In the course of my experiments, additional studies demonstrated that other types of negatively charged nanoparticles, such as DMSA-coated SPIOs were strongly taken up by primary microglia (Pinkernelle et al. 2012; Luther et al. 2013; Petters et al. 2016). The internalization mechanism of anionic SPIOs has been postulated to occur through nonspecific interaction with cationic domains of the extracellular membrane (Wilhelm et al. 2003; Verma and Stellacci 2010; Andreas et al. 2012). After attaching and clustering at the plasma membrane, SPIOs are internalized into cells, including microglia via endocytic mechanisms and are, subsequently, transported into lysosomal compartments (Fleige et al. 2001; Tysiak et al. 2009; Verma and Stellacci 2010; Andreas et al. 2012; Pinkernelle et al. 2012; Luther et al. 2013; Wu et al. 2013a). Cellular accumulation of ferucarbotran via clathrin receptor-mediated endocytosis has already been described previously for macrophages (Lunov et al. 2010; Soenen et al. 2010a; Yang et al. 2011a). Therefore, it seems likely that this uptake mechanism also applies for primary microglia. After internalization by macrophages, carboxydextran-coated particles were found to be located in early endosomes that migrate toward lysosomal vesicles, where the acidic environment facilitates the degradation of the carboxydextran coat and iron oxide cores (Arbab et al. 2005; Lunov et al. 2010; Andreas et al. 2012; Schweiger et al. 2012; Wu et al. 2013a). A similar uptake and degradation mechanism has been described for citrate-coated, negatively charged VSOPs (Wilhelm et al. 2003; Soenen et al. 2010a; Andreas et al. 2012). As the facilitated accumulation of VSOPs and ferucarbotran resulted in a concentration- and exposure time-dependent consistent decrease in microglial viability over 24 hours (Figure 9), it can be assumed that iron liberated from iron oxide cores plays a decisive role (Luther et al. 2013; Petters et al. 2016). Using anionic DMSA-coated SPIOs, it has been demonstrated that particles internalized via the lysosomal pathway were rapidly degraded. This lead to the release of ferrous iron, which was, subsequently, transported into the cytosol, where it may stimulate the synthesis of the iron storage protein ferritin (Petters et al. 2014; Petters et al. 2016). Especially high iron concentration of 3.0 mM resulted in ROS production and compromised microglial viability. The elevated ROS generation

appeared to be caused by excess iron, catalyzed by ferritin. When using lower concentrations, ROS production was not induced and immediate toxic effects were not observed (Levy et al. 2010; Petters et al. 2014). Furthermore, formation of intracellular iron deposits can impair mitochondrial function (Mairuae et al. 2011; Andersen et al. 2013; Urrutia et al. 2014), which could also account for the decreased microglia viability with increasing SPIO concentration.

In my experiments, I observed a rapid and quantitatively superior VSOP accumulation by microglia compared to polymer-coated ferucarbotran and ferumoxytol, which might partially be due to their small size below 10 nm and resulting higher surface-to-volume ratio. Investigations applying VSOPs as target specific contrast agents found that these particles were attached to extracellular membrane glycosaminoglycans (GAGs) prior to internalization (Ludwig et al. 2013; Wagner et al. 2013; Berndt et al. 2017). As GAGs are negatively charged, it is assumed that their high chelating capacity replaces the citrate coating of VSOPs (Wagner et al. 2013).

In contrast, my investigations showed that ferumoxytol exposure did not lead to decreased microglial viability over a time span of 24 hours of exposure (Figure 9) (Neubert et al. 2015). As cultured primary microglia do not further proliferate after being adherent (Floden and Combs 2007), this effect cannot have been due to an enhanced microglial proliferation that would eliminate dead cells and explain the differences in the statistics (Figure 9). Due to the coating material, ferumoxytol exhibits a neutral surface charge, which potentially diminishes the interaction with extracellular membrane components. Ferumoxytol has been designed for the treatment of human CKD (Kowalczyk et al. 2011) and, therefore, exhibits a tendency to avidly release free iron ions. This is due to the poor affinity of the coating material toward the iron oxide cores, so that the coating is reversibly adsorbed (Lin et al. 2008b; Balakrishnan et al. 2009; Kowalczyk et al. 2011). Consequently, ferumoxytol rapidly degraded after it was added to cell cultures, which induced the release of free iron ions and deposition of extracellular iron. Cytotoxicity induced by nanoparticles has been strongly associated with the release of free metal ions and decreased mitochondrial activity accompanied by increased levels of ROS (Wang et al. 2011; Geppert et al. 2012; Horie et al. 2012; Hohnholt and Dringen 2013; Cupaioli et al. 2014; Petters et al. 2016). The potential generation of free oxygen radicals might subsequently adversely affect microglial survival in the long term (Mairuae et al. 2011; Andersen et al. 2013). The exposure to ferumoxytol in high doses might diminish microglial particle accumulation over an extended period of time because elevated iron levels strongly impair the endocytic activity of microglia by affecting mitochondrial function (Mairuae et al. 2011; Urrutia et al. 2014). This could explain increased cell survival within the relatively short incubation of 24 hours with ferumoxytol (Neubert et al. 2015). Whether this actually applies needs to be investigated by using much longer exposure times of several days or weeks.

These results suggest that SPIO-induced activation of microglia may lead to a defensive response, which could also result in chronic microglial activation accompanied with a sustained of neurotoxic signalling molecules (Minghetti et al. 2005; Walter and Neumann 2009; Lull and Block 2010; Andersen et al. 2013; Cupaioli et al. 2014; Zhang et al. 2014). This could eventually lead to neurodegeneration and has been implicated in the onset and progression of various pathological processes within the CNS.

4.2 Consequences of SPIO exposure on neurons

Research data on SPIOs interactions with neurons has shown both negative (Block et al. 2004; Pisanic et al. 2007; Rivet et al. 2012; Xue et al. 2012) and positive impact (Silva 2010; Kim et al. 2011; Neubert and Brauer 2015). This is likely due the fact that SPIOs of various composition were applied on different cell culture models, which is presented as an overview in Table 9. Several studies provide evidence that nanoparticles can induce neurotoxicity dependent on their size, surface coating and charge (Kim et al. 2006; Karlsson et al. 2009; Hu and Gao 2010; Yang et al. 2010; Hong et al. 2011; Horie et al. 2012; Liu et al. 2013; Wu et al. 2013b; Migliore et al. 2015; Valdiglesias et al. 2015; Jarockyte et al. 2016), which I confirmed in this study (Neubert et al. 2015).

Here, I show that the morphology and viability of primary hippocampal neurons in monocultures is severely affected by clinically relevant SPIOs of different composition (Neubert et al. 2015). Ferucarbotran and two types of VSOPs, both possess a negative surface charge, were continually accumulated by primary neurons as shown with Prussian blue staining (Figure 10 A and B). These SPIOs were especially localized around the neuronal cell body but were also distributed along neurites. This intense accumulation of ferucarbotran and VSOPs around the somata of primary neurons appeared to adversely affect neuronal morphology as shown with Sholl analysis (Figure 13, A, C and E). Although immunocytochemistry did not evidently reveal reduced number of neuronal processes (Figure 11), Sholl analysis clearly showed reduced numbers of neurites, especially proximal to neuronal somata, of neurons exposed to SPIOs (Figure 13). The preferential binding of carboxydextran- and citrate-coated SPIOs onto neuronal somata is most likely due to the high affinity of the anionic surface charge towards positively charged domains of the extracellular membrane (Wilhelm et al. 2003; Soenen et al. 2010a; Andreas et al. 2012; Ludwig et al. 2013). Moreover, I suggest that membrane-associated particles at the somata were internalized, which might explain the significantly increased numbers of degenerated neurons indicating a loss in viability of neurons exposed to all iron concentrations of ferucarbotran and high iron concentrations of VSOP-R2 (Figure 15). This is in line with other reports that demonstrated neurotoxic effects of SPIOs after internalization and intracellular iron accumulation (Kim et al. 2006; Rivet et al. 2012; Xue et al. 2012; Wu et al. 2013b; Yarjanli et al. 2017). Interestingly, ferumoxytol-exposed neurons revealed significantly decreased number of proximal neurites independent of the particle concentration (Figure 13), although ferumoxytol was not detectable with Prussian blue staining (Figure 10 C). Compared to negatively charged SPIOs, the neutral surface charge of ferumoxytol prevents electrostatic interactions with the cell membrane and subsequent internalization by neurons. The poor affinity of the carboxymethyl-dextran coating towards iron oxide induces rapid particle degradation and the release of free iron ions (Lin et al. 2008b; Balakrishnan et al. 2009; Kowalczyk et al. 2011). Consequently, extracellular iron depositions might be responsible for adverse effect of ferumoxytol on neuronal morphology and viability. I observed elevated numbers of degenerated neurons that were incubated with ferumoxytol, especially in iron concentrations of 1.5 mM compared to control neurons (Figure 15). Therefore, the release of free iron ions from extracellular iron deposits and the subsequent generation of highly toxic oxygen radicals might cause neurodegeneration (Valdiglesias et al. 2015), as hippocampal neurons are highly sensitive to oxidative damage (Yang et al. 2010). Early signs for

neurodegenerative processes might, therefore, be reflected by impaired neuronal morphology and increasing numbers of degenerated cells (Neubert et al. 2015).

These results emphasizes the importance of evaluating SPIO–cell interactions individually according to the physicochemical properties of SPIOs as well as the culture condition. In addition, the exact mechanisms behind the observed adverse effects of the applied SPIOs on neuronal morphology remain to be explored, whereby existing studies using neuronal cell lines could give indications.

Previous to and during my investigations, only a few number of studies performed their tests using primary neurons to investigate SPIO-mediated effects (Rivet et al. 2012; Sun et al. 2013; Petters and Dringen 2015; Petters et al. 2016). Most approaches used immortalized pheochromocytoma (PC12) cells derived from rat adrenal medulla as a model to evaluate neuronal particle uptake and neurotoxicity (Table 9) (Pisanic et al. 2007; Kim et al. 2011; Soenen et al. 2011; Pinkernelle et al. 2012; Xue et al. 2012; Wu et al. 2013b). PC12 cells possess a neuronal phenotype and mimic properties of dopaminergic neurons, including dopamine production. Therefore, this cell line is a popular model for nanoparticle cytotoxicity studies (Pisanic et al. 2007; Kim et al. 2011; Pinkernelle et al. 2012; Xue et al. 2012). In growing PC12 cells (2 DIV), it has been shown that treatment with increasing iron concentrations of up to 1.5 mM of anionic DMSA-coated SPIOs resulted in cytoskeletal alterations, such as reduced microtubules protrusions, reduced formation of actin microfilaments as well as loss of organized actin within the cells (Pisanic et al. 2007; Migliore et al. 2015). Consequently, DMSA-coated SPIOs caused a concentration-dependent decrease in viability of PC12 cells after 24 hours of exposure, which also adversely affected the extension of neurites in response to NGF (Table 9) (Pisanic et al. 2007). In contrast, exposure of PC12 cells to PEG-phospholipid-coated SPIOs and NGF, synergistically, lead to an increase in neurite outgrowth with increasing SPIO-concentrations (Kim et al. 2011). However, prolonged exposure to high iron concentrations of PEG-phospholipid-coated SPIOs was shown to cause neurotoxicity and damage neuronal morphology (Kim et al. 2011). Comparable results were obtained by exposing PC12 cells and neural c17.2 progenitor cells to high iron concentrations of dextran-coated ferumoxide of neutral surface charge as well as anionic carboxydextran-coated ferucarbotran and citrate-coated VSOP-C200, which were, however, complexed with a transfection agent (Soenen et al. 2010b; Soenen et al. 2011). All SPIOs adversely affected the morphology and neurite formation, which correlated with the amount of particle uptake and, subsequently, induced cytotoxic effects (Table 9). However, the concentration-dependent toxicity was transiently reduced until it disappeared when culturing cells for additional 8 days following SPIO exposure (Soenen et al. 2010b). This effect is likely due to SPIO dilution by further cell divisions of the immortalized cell lines (Soenen et al. 2010b) and would not apply to post-mitotic primary neurons, which emphasizes the relevance using primary cells as model system. Additionally, the impact of SPIOs on the morphology and viability of primary neurons in co-culture with glial cells allows for more profound insights into particle-mediated effects.

Table 9: Studies on the effects of SPIOs neuronal cells *in vitro*.

Neuronal cell line	SPIO characteristics	Exposure condition	Effects on neuronal cells	Reference
PC12 cells	DMSA-coated Fe_2O_3 anionic charge 5 – 12 nm	0.15, 15 and 1.5 mM for 24 h	Concentration-dependent decreases in viability and neurite formation, morphological changes	(Pisanic et al. 2007)
Neural c17.2 progenitor cells (mice)	Dextran-coated ferumoxide (Endorem®, neutral charge, 80 – 150 nm) Carboxydextran-coated ferucarbotran (Resovist®, anionic charge, 62 nm) Citrate-coated VSOP (VSOP-C200, anionic charge, 8.6 nm)	500 and 1000 µg/ml + transfection agent Lipofectamine 2000 (5 µl/ml) for 4 and 24 h	Highest amounts of intracellular iron after ferucarbotran, least after VSOP incubation for 24 h Cytoskeletal alterations after ferucarbotran and ferumoxide incubation with 1000µg/ml for 24 h, reduced proliferation Toxic effects after VSOP incubation with 500 µg/ml for 24 h	(Soenen et al. 2010b)
PC12 cells	PEG-phospholipid-coated Fe_3O_4 11 nm	5, 10, 20, and 40 µg/ml + NGF (100 ng/ml) for 1, 3, and 5 days	Slight effects on viability at the highest concentration after 3 or 5 days Increase in neurite outgrowth with increasing SPIO concentration Neurotoxicity at high concentration and prolonged exposure	(Kim et al. 2011)
Neural c17.2 progenitor cells (mice) **PC12 cells**	Dextran-coated ferumoxide (Endorem®, neutral charge, 80 – 150 nm) Carboxydextran-coated ferucarbotran (Resovist®, anionic charge, 62 nm) Citrate-coated VSOP (VSOP-C200, anionic charge, 8.6 nm)	200 and 400 µg/ml of Endorem®, 150 and 300 µg/ml of Resovist®, 200 and 600 µg/ml of VSOP-C200 + transfection agent Lipofectamine 2000 (5 µl/ml) for 4 and 24 h	c17.2 cells: no effect on viability, but cytotoxicity through ROS production and decreased proliferative capacity at high concentrations PC12 cells: Internalized SPIOs faster than c17.2 cells, adverse effect of all SPIOs on neurite formation	(Soenen et al. 2011)

Neuronal cell line	SPIO characteristics	Exposure condition	Effects on neuronal cells	Reference
Primary cortical neurons (chick)	Amine-coated (45.3 nm), Dextran- coated (24.7 nm) and PEA-coated (47.5 nm) Fe_3O_4	1, 5, and 10 % of stock particle solution 39.3 mg/ml (Amine-Fe_3O_4), 53.1 mg/ml (Dextran- Fe_3O_4), 60.5 mg/ml (PEA-Fe_3O_4) for 24 h	PEA- Fe_3O_4 induced toxic effects Amine- Fe_3O_4 significantly decreased metabolic activity in concentration-dependency Dextran- Fe_3O_4 partially altered viability at highest concentrations	(Rivet et al. 2012)
PC12 cells **Primary cerebellar neurons (mixed cultures)**	Fluorescent polymer-coated SPIOs Anionic charge 190 nm	10, 50 and 100 µg/ml for 24 h	Significant increase in SPIO uptake by PC12 cells compared to neurons from mixed cultures	(Pinkernelle et al. 2012)
PC12 cells	Fe_3O_4 45 nm	0.25 and 0.50 mg/ml for 24 and 48 h	Cytotoxicity through soluble factors from SPIO-treated microglia	(Xue et al. 2012)
Primary cortical neurons (mice)	AmS-coated (cationic charge) and Carboxyl-AmS-coated Fe_3O_4 (anionic charge) 27 nm	0.1 – 224 µg/mL for 24 h	Cytotoxicity above 100 µg/ml SPIO concentration, especially AmS-Fe_3O_4, moderate SPIO uptake	(Sun et al. 2013)

Neuronal cell line	SPIO characteristics	Exposure condition	Effects on neuronal cells	Reference
PC12 cells	Uncoated Fe_3O_4 30 nm	25, 50, 100 and 200 µg/mL for 6 or 24 h	Dose-dependent toxicity, increased ROS, reduced GSH, induced apoptosis	(Wu et al. 2013b)
Primary cerebellar granule cells (rat)	DMSA-coated ɣ-Fe_2O_3 Anionic charge 80 – 120 nm	0, 0.5, 1.0, 1.5 and 2 mM for 1, 2, 4 and 6 h	Delayed toxicity in time and concentration dependency, no altered morphology or viability	(Petters and Dringen 2015)
Primary cerebellar granule cells (rat)	Fluorescent DMSA coated ɣ-Fe_2O_3 Anionic charge 42 – 49 nm	0.1, 0.3, 1.0 and 3.0 mM for 6 h and 0.3 mM for 24 h	No influence on viability, slight increase in ROS	(Petters et al. 2016)

In contrast to primary neurons from monocultures, SPIO exposure did not cause coherent reduction of neurites of neurons from neuron-glia co-cultures. Neurite branching of hippocampal neurons cultured with glial cells partially increased in a particle type- and dose-dependent manner (Figure 17). Here, iron concentrations below 3.0 mM of ferucarbotran (Figure 17A and C) and 3.0 mM of VSOP-R2 (Figure 17E) caused increasing numbers of neurites compared to untreated neurons, whereas 1.5 mM of VSOP-R2 induced a slight reduction in neurite numbers (Figure 17C). The contrary effects of ferucarbotran and VSOP-R2 on the morphology of co-culture neurons might be associated with the particle size. VSOPs, as the smallest particles of approximately 8 nm, might be rapidly taken up by activated microglial cells, which could be further promoted by the anionic surface charge (Soenen et al. 2010b). Since neuron-glia co-cultures contained equal amounts of primary neurons and microglia (Figure 16), preferential SPIO uptake by microglial cells, which has been shown for other nanoparticle types in mixed cultures (Pickard and Chari 2010; Pinkernelle et al. 2012) can be assumed. Consequently, neurons are exposed to a less extent to SPIOs, even when challenged by high iron concentrations. However, the long-term consequences of SPIO-accumulation by microglia remains to be elucidated.

However, in this context it is important to consider that activated microglia, which can also be caused by SPIOs, can also induce neurotoxicity through the release of pro-inflammatory mediators (Minghetti et al. 2005; Pais et al. 2008; Lull and Block 2010; Wang et al. 2011; Kierdorf and Prinz 2013). Activated microglia not only promote neuronal damage by producing a wide range of cytotoxic factors, such as TNFα, NO, or ROS, but also support neuronal survival by releasing trophic and anti-inflammatory factors (Biber et al. 2007; Lull and Block 2010; Smith et al. 2012; Kierdorf and Prinz 2013; Ye et al. 2013). Nonetheless, iron accumulations in neurons and microglia are promoted by inflammatory cytokines, like TNFα and IL-6, which are caused by mitochondrial dysfunction (Mairuae et al. 2011; Urrutia et al. 2014). As these conditions can,

consequently, weaken the phagocytic activity of activated microglia, intracellular iron accumulations might have detrimental effects in the long term.

In contrast, it could be suggested that the applied SPIOs may exert a stimulatory effect on neurite branching of co-culture neurons in a concentration- and particle type-dependent manner (Neubert et al. 2015), which has been shown for PC12 cells (Kim et al. 2011). However, astrocytes in neuron-glia co-cultures might also contribute to protection of neurons from detrimental SPIO interactions. First of all, co-culturing neurons with astrocytes make them less vulnerable to adverse stimuli (Schmalenbach and Muller 1993; Park et al. 2001; Liu et al. 2017). This can be explained by the metabolic support of neurons by astrocytes. In addition, astrocytes are well known for their neuroprotective potential against iron-mediated oxidative stress and their release of neurotrophic mediators and growth-promoting glycoproteins (Schmalenbach and Muller 1993; Dringen et al. 2007; Jones et al. 2012; Liu et al. 2017). Astrocytes their major role in iron metabolism (Dringen et al. 2007; Pelizzoni et al. 2013; Liu et al. 2017) and have been shown efficiently accumulate anionic nanoparticles through clathrin-mediated endocytosis without the induction of cytotoxicity, even at high particle concentrations (Geppert et al. 2009; Hohnholt and Dringen 2013). Furthermore, astrocytes are capable of storing particle-derived excess iron in the intracellular storage protein ferritin (Geppert et al. 2009; Geppert et al. 2012), which could attenuate adverse impact of SPIOs on neuronal morphology, thereby protecting neurons from oxidative stress.

The variety of different processes that account for SPIO-induced effects on brain cells highlight the complexity of the involved mechanisms. My investigations demonstrate that the unique properties SPIOs differentially affect the morphology and viability of primary brain cells, which is closely associated with particle size, surface coating, charge, iron concentration and exposure time. Furthermore, the model system plays a decisively role. These results show the difficulty to reliably predict the consequences of nanoparticle exposure on brain cells and the subsequent influences on cell physiology in the long term. In turn, particle–cell interactions as well as measurement-influencing parameters should accurately be validated for individual SPIOs in advance. Additionally, long-term effects of other diagnostically and therapeutically applied SPIOs on cellular metabolism and functionality should be thoroughly investigated, because adverse effects cannot be estimated across different SPIO types.

4.3 Cytokine and chemokine secretion by brain cells in culture

CNS function might strongly be disturbed by tremendous secretion of microglia-derived cytokines and chemokines (Hanisch 2002; Hanisch and Kettenmann 2007; Napoli and Neumann 2009; Ransohoff and Perry 2009; Kettenmann et al. 2011; Smith et al. 2012) , which was partially mentioned in the previous sections. Due to the complexity of neuron-glia communication involving a wide array of signal molecules, which were not found to be significantly and profoundly influenced by SPIO exposure (Figure 19), this topic will not be further discussed. Moreover, a subsequent study that was performed in by a member of our research group using murine organotypic hippocampal slice cultures showed that VSOP treatment with the same iron concentrations used in the presented study did not affect cytokine homeostasis (Pohland et al. 2017).

4.4 Clinical significance of obtained results

The off-label application of ferumoxytol for MRI imaging of CNS pathologies could have serious consequences on brain functionality considering that ferumoxytol has been found in areas of dysfunctional BBB, which may be fundamentally related to neuroinflammation (Weinstein et al. 2010; Schieda 2013; McConnell et al. 2016; Toth et al. 2017). The consequences of ferumoxytol extravasation from the cerebrovasculature and subsequent accumulation within the brain parenchyma cannot be estimated (McConnell et al. 2016). Moreover, differences in ferumoxytol clearance among patients have been reported (Hasan et al. 2012). Special caution has to be exercised when using ferumoxytol in pregnant woman because potential iron deposits could dramatically influence brain development of neonates and young infants (Thompson et al. 2012; Ruangwattanapaisarn et al. 2015; Lai et al. 2017). Therefore, the results obtained in this thesis contribute to re-evaluate ferumoxytol administration.

In addition, previous studies using models that mimic the BBB clearly demonstrated that SPIOs are capable of crossing the intact BBB depending on their composition, including size, surface coating and charge (Lockman et al. 2004; Kong et al. 2012; Dan et al. 2013; Thomsen et al. 2013; Sun et al. 2014). Moreover, the applied magnetic field when using SPIOs as contrast agents in MRI accelerates BBB penetration (Kong et al. 2012; Hoff et al. 2013; Thomsen et al. 2013; Sun et al. 2014).The probability of brain cells to encounter SPIOs is tremendously increased when these particles are systemically administered for diagnosis under neuroinflammatory conditions with dysfunctional BBB, such as traumatic brain injury, multiple sclerosis or Alzheimer's disease (Weinstein et al. 2010). Here, different types of SPIOs have been reported to be transported into the brain, for instance, by leukocytes that phagocytosed particles (Petry et al. 2007; Tysiak et al. 2009; Weinstein et al. 2010; Weise and Stoll 2012; Krol et al. 2013; Millward et al. 2013). Therefore, previously reports have raised serious concerns about SPIO-induced neurotoxicity (Oberdorster et al. 2009; Hu and Gao 2010; Cupaioli et al. 2014; Jarockyte et al. 2016), however, did not apply clinically approved SPIOs in relevant doses. I showed that primary microglia effectively and rapidly accumulate SPIOs. Consequently, I observed clear indications of microglial activation upon particle accumulation based on morphological observation. Although the long term fate of SPIOs entering the brain remains to be explored, they can potentially induce chronic microglial activation, which has been shown to cause neurodegeneration (Minghetti et al. 2005; Walter and Neumann 2009; Lull and Block 2010; Andersen et al. 2013; Cupaioli et al. 2014; Zhang et al. 2014). In addition, excess iron and iron deposition within the brain have been associated with the onset and progression of neurodegenerative diseases, including Friedreich's ataxia, Parkinson's disease, Alzheimer's disease and multiple sclerosis (Andersen et al. 2013; Hare et al. 2013; Rouault 2013; Urrutia et al. 2014). Under neuropathological conditions, activated microglia have been found to either cause BBB breakdown or become activated as a consequence of BBB dysfunction (Fleige et al. 2001; da Fonseca et al. 2014). In fact, increased SPIO accumulation by microglia have been found in tumorous and inflammatory CNS lesions (Tysiak et al. 2009; Weinstein et al. 2010; Ittrich et al. 2013; Iv et al. 2015). Hence, the administration SPIOs that target the brain requires particular caution.

4.5 Methodological limitations

4.5.1 Cell cultures

In general, investigations using cultured primary brain cells limit the informative value concerning cell-cell interactions between different cell types, their selective responses and also vulnerability towards adverse stimuli. The *in vitro* model is lacking the complexity of structure and function within the three dimensional organization of the brain *in vivo*. Thus, SPIO-mediated effects are of higher biological significance when studied in slice culture models, where some the brain architecture is partially preserved. Ultimately, observations have to be verified in animal models to produce conclusive results.

A fact that potentially limits the relevance of the obtained results concerns investigations using microglial cell cultures. Cultivated microglial cells isolated from early postnatal brains have been shown to change their phenotype from an ovoid to a strongly ramified morphology after several days in culture (Caldeira et al. 2014). In my experiments, microglia were treated with SPIOs 24 hours after isolation from mixed glial cultures, which could have potentially biased the results concerning microglial activation. However, I predominantly observed strongly ramified morphologies of microglia that have not been exposed to particles and kept under same environmental conditions. It has also been reported that microglia kept for 10 DIV in culture show reduced phagocytic capacity compared to microglia cultivated for only 2 DIV (Caldeira et al. 2014).

4.5.2 Technical limitations

My data show that SPIO accumulation was elevated with increasing particle concentration and incubation time in a non-proportional manner (Figure 9, grey bars). Prussian blue staining was used in order to quantify microglial SPIO accumulation because it allowed to correlate staining intensities with values of previously performed PI measurements. Despite characteristic morphological features indicating microglial activation associated with SPIO-type dependent accumulation were clearly depicted, the applied techniques have limitations in their informative value. From a technical perspective, iron quantification by measuring the Prussian blue staining intensity using greyscale provides only an assessable spectrum of zero to 255 shades of grey. Consequently, the iron quantification cannot exceed the maximum darkness intensity, which might have restricted the amount of identifiable SPIOs. Therefore, the presented approach to quantify cell-associated SPIOs might not show proportional increases with increasing particle concentration. Another option to quantify cellular iron content of cultured cells is a colorimetric ferrozine-based assay (Riemer et al. 2004). However, cell lysates are used for iron quantification, which excludes the possibility to perform PI measurements prior Prussian blue staining of the same cell cultures. In addition, quantifying the iron content in an aliquot could bias the measured amount of iron per cell because potential SPIO aggregations would also be included, resulting in calculations with higher iron amounts per cell (Mailander et al. 2008). From a physiological perspective, the phagocytic capacity of microglia limits the amount of possibly accumulated and incorporated particles (Sierra et al. 2013). Due to the time-dependent saturation

of SPIO uptake by microglia, a prolonged incubation for up to 24 hours does not lead to proportional increases in detectable iron.

Another limitation concern the applied staining methods. The combination of Prussian blue staining to detect microglial SPIO accumulation with immunocytochemical staining to visualize microglial morphology of the same cells is not possible. This is due to the absorption of fluorescent light in the range of 365 to 490 nm by Prussian blue or ferric ferrocyanide, which is within the emission spectrum of FITC (530 ± 50 nm) and Hoechst 33258 (similar to 4',6-diamidino-2-phenylindole, DAPI ≥ 470 nm) (Frank et al. 2007). Hence, Prussian blue would reduce immunofluorescence of microglia morphology and limit their visualization following SPIO exposure. An alternative approach would be to perform immunocytochemistry prior Prussian blue staining, which requires removing the glass cover slips from microscopic slides after they have been imaged leading to mechanical damage of microglia.

In this study, commonly applied cytotoxicity measurements, such as 3-(4,5-dimethylthiazol-2-yl)-2,5-diphenyltetrazolium bromide (also known as MTT) assay to investigate mitochondrial function, or lactate dehydrogenase (LDH) release assay to assess cell membrane integrity were not performed because the accuracy and reliability with these methods for assessing cytotoxicity is restricted (Liu et al. 2013). It has been frequently demonstrated that SPIOs can physicochemically interfere with the measurement or interact with assay components, thereby biasing the results (Kroll et al. 2009; Holder et al. 2012; Kroll et al. 2012; Liu et al. 2013). In general, protocols to assess nanoparticle-mediated toxicity should be more uniform and produce reliable data.

4.5.3 Additional considerations

The efficiency of cellular SPIO internalization and metabolism is critically influenced by surface coating and respective surface charge (Safi et al. 2011; Saito et al. 2012; Schweiger et al. 2012; Petters and Dringen 2015). Especially, the surface charge of SPIOs determines interactions with cell membrane domains of opposite charge or extracellular GAGs (Wilhelm et al. 2003; Ludwig et al. 2013; Berndt et al. 2017). Importantly, surface charge not only affects nanoparticle binding to cells but also interactions with cell culture medium components, such as serum proteins. The protein adsorption leads to the formation of a protein corona around particles, which increases the effective hydrodynamic diameter and also affects the particle agglomeration (Verma and Stellacci 2010; Safi et al. 2011; Horie et al. 2012; Schweiger et al. 2012; Hirsch et al. 2013; Horie et al. 2013; Sakulkhu et al. 2014). The nanoparticle-protein complex could decisively influence the cellular response, as it has been shown for anionic DMSA-coated SPIOs (Petters and Dringen 2015). In the presence of 10 % FCS, particle uptake by primary neurons occurred much slower than in the absence of serum in the cell culture media. These investigations concerning SPIO composition-dependent interactions with serum components were, however, not performed in this study but should certainly be included and further characterized in perspective approaches.

4.6 Future perspectives

SPIOs used as multifunctional tools could offer revolutionary approaches for the treatment of neurodegenerative diseases (Shubayev et al. 2009; Silva 2010; Gendelman et al. 2015; Neubert and Brauer 2015; Saraiva et al. 2016; Silva Adaya et al. 2017). As SPIOs can be directed by an external magnetic field, they can potentially serve as diagnostic marker and delivery vehicle for therapeutic agents, simultaneously (Shubayev et al. 2009; Rumenapp et al. 2012; Ittrich et al. 2013; Wu et al. 2015a). Novel therapeutic strategies for CNS injuries are exploring the utility of SPIOs to promote neuronal regeneration on the molecular level (Neubert and Brauer 2015; Papastefanaki et al. 2015; Polak and Shefi 2015). For instance, it has been shown that iron ions from certain nanoparticles enhance neuronal differentiation and survival of PC12 cells, thereby promoting neurite outgrowth in a dose-dependent manner (Kim et al. 2011).

The restricted regeneration and growth potential of neurons within the adult CNS (Pernet and Schwab 2014) lead to the concept of modulating extracellular cues and receptors as well as influencing cytoskeletal dynamics of neurons involved in axonal and dendritic growth by utilizing SPIOs (Neubert and Brauer 2015). In CNS injury and glial scar formation, the distal tip of the axonal growth cone communicates with the intra- and extracellular environment at the growth cone, which regulates molecular mechanisms for axon guidance (O'Donnell et al. 2009). Therefore, targeting the growth cone with SPIOs and, subsequently, remote guide the particle labelled axon using a magnetic force can potentially promote neurite outgrowth (Pita-Thomas et al. 2015). The experimental approach applied SPIOs that were functionalized with Cholera Toxin B and anti-Thy1 antibody, which bind to growth cone membranes of primary retinal ganglion cells (RGCs). The application of a local magnetic field force induced axon elongation of the SPIO-labelled growth cone (Pita-Thomas et al. 2015). This controlled mechanism for directional axonal outgrowth can be further investigated to achieve target specificity of axon guidance during regeneration processes in the adult brain. Another strategy to promote neurite outgrowth explores SPIO functionalization with antibodies that activate neurotrophin receptors (Steketee et al. 2011). The internalization of both the receptor and SPIOs under the influence of a magnetic force induced neurite elongation to the same extend as BDNF that is critically involved in neuroregeneration (Steketee et al. 2011; Neubert and Brauer 2015).

Another interesting approach to promote neuronal regeneration involves the utilization of extracellular vesicles (EVs), which have been shown to be critically involved in neuron-glia communication (Neubert and Glumm 2016). These vesicles, derived through either budding of the plasma membrane or ectocytosis of multivesicular bodies, have been shown to be secreted by neurons, microglia and astrocytes (Kalani et al. 2014). Hence, EVs carry functionally active cargos, such as genetic material, proteins and lipids and can be differentiated by their membrane composition, which contains information about their cell of origin. This membrane composition also determines the fate of the EV and can decisively influence the response of its recipient (Kalani et al. 2014). The encapsulation of SPIOs in membranes of EVs has created a novel concept for therapeutic interventions on the molecular level. SPIO-labelled EVs could be loaded with neurotrophic factors and guided by an external magnetic field for targeted delivery (Neubert and Glumm 2016). This approach of using biological entities could be further applied in cancer treatment by loading EVs with chemotherapeutic agents together with SPIOs and magnetically remote guided them to the tumour.

However, several aspects still require intensive investigation before its clinical translation, including specific cargo release and SPIO biocompatibility as well as long term fate of iron particles (Neubert and Glumm 2016).

Although great progress in nanotechnology has been made, information about SPIO-induced toxicity is still incomplete and unexpected adverse side effects are only detected after they occurred. Studies dealing with nanotoxicology and biocompatibility hardly include cumulative and nanoparticle-associated effects on cell function, which could result in irreversible damage following internalization, especially after entering the CNS. SPIOs must meet several requirements in order to be safely applied in living organisms for basic research purposes or in humans as contrast agents in clinical practice. To assess potential risks of nanoparticle exposure and to determine the pharmacokinetic and pharmacodynamic consequences, detailed information about the SPIO type-dependent release, translocation, elimination and metabolism is required. For their successful utilization, it is absolutely essential to understand the biological activity of SPIOs. First of all, it is of high importance to use adequate model systems and experimental approaches to evaluate the effects of SPIO. This includes the precise SPIO localization within cells and their compartments, for instance, by using electron microscopy and strategies to determine their fate and degradation. Prospective studies should certainly focus on initial test series using primary cells to estimate the kind of cellular influence, and proceed with cytotoxicity measurements on more complex experimental models, like slice cultures. Subsequently, cell functionality following SPIO administration within living organisms has to be explored thoroughly. Reliable data should be generated that can serve as representative of consequences on the human brain. This requires standardized protocols and strategies for cytotoxicity assessment. So far, cytotoxicity measurements were performed using a many different primary cells and cell lines as well as a wide variety of different types of SPIOs that exhibit their own specific surface chemistry and size. Variations in cell exposure protocols investigating particle-cell interactions and internalization hamper the predictability about the safe profile of SPIOs used as contrast agents in MRI. Although various SPIO coating materials have been tested to avoid particle-mediated cytotoxicity, the need for standardized procedures still persists.

References

2004. Citrate-coated (184(th) variant) very small superparamagnetic iron oxide particles. Molecular Imaging and Contrast Agent Database (MICAD). Bethesda (MD).

Abbott NJ. 2002. Astrocyte-endothelial interactions and blood-brain barrier permeability. J Anat 200(6):629-638.

Abbott NJ, Patabendige AA, Dolman DE, Yusof SR, Begley DJ. 2010. Structure and function of the blood-brain barrier. Neurobiol Dis 37(1):13-25.

Adamec E, Yang F, Cole GM, Nixon RA. 2001. Multiple-label immunocytochemistry for the evaluation of nature of cell death in experimental models of neurodegeneration. Brain Res Brain Res Protoc 7(3):193-202.

Ajami B, Bennett JL, Krieger C, Tetzlaff W, Rossi FM. 2007. Local self-renewal can sustain CNS microglia maintenance and function throughout adult life. Nat Neurosci 10(12):1538-1543.

Ali A, Zafar H, Zia M, Ul Haq I, Phull AR, Ali JS, Hussain A. 2016. Synthesis, characterization, applications, and challenges of iron oxide nanoparticles. Nanotechnol Sci Appl 9:49-67.

Anand KS, Dhikav V. 2012. Hippocampus in health and disease: An overview. Ann Indian Acad Neurol 15(4):239-246.

Andersen HH, Johnsen KB, Moos T. 2013. Iron deposits in the chronically inflamed central nervous system and contributes to neurodegeneration. Cell Mol Life Sci.

Andreas K, Georgieva R, Ladwig M, Mueller S, Notter M, Sittinger M, Ringe J. 2012. Highly efficient magnetic stem cell labeling with citrate-coated superparamagnetic iron oxide nanoparticles for MRI tracking. Biomaterials 33(18):4515-4525.

Anselmo AC, Mitragotri S. 2016. Nanoparticles in the clinic. Bioeng Transl Med 1(1):10-29.

Araya T, Kasahara K, Nishikawa S, Kimura H, Sone T, Nagae H, Ikehata Y, Nagano I, Fujimura M. 2013. Antitumor effects of inductive hyperthermia using magnetic ferucarbotran nanoparticles on human lung cancer xenografts in nude mice. Onco Targets Ther 6:237-242.

Arbab AS, Wilson LB, Ashari P, Jordan EK, Lewis BK, Frank JA. 2005. A model of lysosomal metabolism of dextran coated superparamagnetic iron oxide (SPIO) nanoparticles: implications for cellular magnetic resonance imaging. NMR Biomed 18(6):383-389.

Au C, Mutkus L, Dobson A, Riffle J, Lalli J, Aschner M. 2007. Effects of nanoparticles on the adhesion and cell viability on astrocytes. Biol Trace Elem Res 120(1-3):248-256.

Balakrishnan VS, Rao M, Kausz AT, Brenner L, Pereira BJ, Frigo TB, Lewis JM. 2009. Physicochemical properties of ferumoxytol, a new intravenous iron preparation. Eur J Clin Invest 39(6):489-496.

Barbu E, Molnar E, Tsibouklis J, Gorecki DC. 2009. The potential for nanoparticle-based drug delivery to the brain: overcoming the blood-brain barrier. Expert Opin Drug Deliv 6(6):553-565.

Barnes AP, Polleux F. 2009. Establishment of axon-dendrite polarity in developing neurons. Annu Rev Neurosci 32:347-381.

Beaudoin GM, 3rd, Lee SH, Singh D, Yuan Y, Ng YG, Reichardt LF, Arikkath J. 2012. Culturing pyramidal neurons from the early postnatal mouse hippocampus and cortex. Nat Protoc 7(9):1741-1754.

Berndt D, Millward JM, Schnorr J, Taupitz M, Stangl V, Paul F, Wagner S, Wuerfel JT, Sack I, Ludwig A, Infante-Duarte C. 2017. Inflammation-induced brain endothelial activation leads to uptake of electrostatically stabilized iron oxide nanoparticles via sulfated glycosaminoglycans. Nanomedicine 13(4):1411-1421.

Biber K, Neumann H, Inoue K, Boddeke HW. 2007. Neuronal 'On' and 'Off' signals control microglia. Trends Neurosci 30(11):596-602.

Biffi E, Regalia G, Menegon A, Ferrigno G, Pedrocchi A. 2013. The influence of neuronal density and maturation on network activity of hippocampal cell cultures: a methodological study. PLoS One 8(12):e83899.

Block ML, Wu X, Pei Z, Li G, Wang T, Qin L, Wilson B, Yang J, Hong JS, Veronesi B. 2004. Nanometer size diesel exhaust particles are selectively toxic to dopaminergic neurons: the role of microglia, phagocytosis, and NADPH oxidase. FASEB J 18(13):1618-1620.

Block ML, Zecca L, Hong JS. 2007. Microglia-mediated neurotoxicity: uncovering the molecular mechanisms. Nat Rev Neurosci 8(1):57-69.

Bradke F, Dotti CG. 2000. Establishment of neuronal polarity: lessons from cultured hippocampal neurons. Curr Opin Neurobiol 10(5):574-581.

Burkhart A, Skjorringe T, Johnsen KB, Siupka P, Thomsen LB, Nielsen MS, Thomsen LL, Moos T. 2016. Expression of Iron-Related Proteins at the Neurovascular Unit Supports Reduction and Reoxidation of Iron for Transport Through the Blood-Brain Barrier. Mol Neurobiol 53(10):7237-7253.

Buzea C, Pacheco, II, Robbie K. 2007. Nanomaterials and nanoparticles: sources and toxicity. Biointerphases 2(4):MR17-71.

C. HM, Mark G, Sylvia N, Janek vB, Ingo G, Ralf D. 2010. Advanced Biomaterials Accumulation of Citrate-Coated Magnetic Iron Oxide Nanoparticles by Cultured Brain Astrocytes. Advanced Engineering Materials 12(12):B690-B694.

Caldeira C, Oliveira AF, Cunha C, Vaz AR, Falcao AS, Fernandes A, Brites D. 2014. Microglia change from a reactive to an age-like phenotype with the time in culture. Front Cell Neurosci 8:152.

Cameron DG, Bensley EH, Wood P, Grayston V. 1951. Treatment of iron deficiency anaemia with saccharated iron oxide given by the intravenous route. Can Med Assoc J 64(1):27-30.

Cartwright L, Poulsen MS, Nielsen HM, Pojana G, Knudsen LE, Saunders M, Rytting E. 2012. In vitro placental model optimization for nanoparticle transport studies. Int J Nanomedicine 7:497-510.

Casano AM, Peri F. 2015. Microglia: multitasking specialists of the brain. Dev Cell 32(4):469-477.

Cengelli F, Maysinger D, Tschudi-Monnet F, Montet X, Corot C, Petri-Fink A, Hofmann H, Juillerat-Jeanneret L. 2006. Interaction of functionalized superparamagnetic iron oxide nanoparticles with brain structures. J Pharmacol Exp Ther 318(1):108-116.

Chatterjee DK, Diagaradjane P, Krishnan S. 2011. Nanoparticle-mediated hyperthermia in cancer therapy. Ther Deliv 2(8):1001-1014.

Chen R, Ling D, Zhao L, Wang S, Liu Y, Bai R, Baik S, Zhao Y, Chen C, Hyeon T. 2015. Parallel Comparative Studies on Mouse Toxicity of Oxide Nanoparticle- and Gadolinium-Based T1 MRI Contrast Agents. ACS Nano 9(12):12425-12435.

Contado C. 2015. Nanomaterials in consumer products: a challenging analytical problem. Front Chem 3:48.

Craig AM, Banker G. 1994. Neuronal polarity. Annu Rev Neurosci 17:267-310.

Cupaioli FA, Zucca FA, Boraschi D, Zecca L. 2014. Engineered nanoparticles. How brain friendly is this new guest? Prog Neurobiol 119-120:20-38.

da Fonseca AC, Matias D, Garcia C, Amaral R, Geraldo LH, Freitas C, Lima FR. 2014. The impact of microglial activation on blood-brain barrier in brain diseases. Front Cell Neurosci 8:362.

Dan M, Cochran DB, Yokel RA, Dziubla TD. 2013. Binding, transcytosis and biodistribution of anti-PECAM-1 iron oxide nanoparticles for brain-targeted delivery. PLoS One 8(11):e81051.

Davalos D, Grutzendler J, Yang G, Kim JV, Zuo Y, Jung S, Littman DR, Dustin ML, Gan WB. 2005. ATP mediates rapid microglial response to local brain injury in vivo. Nat Neurosci 8(6):752-758.

de Vellis J, Cole R. 2012. Preparation of mixed glial cultures from postnatal rat brain. Methods Mol Biol 814:49-59.

Deierborg T. 2013. Preparation of primary microglia cultures from postnatal mouse and rat brains. Methods Mol Biol 1041:25-31.

Del Rio MR, DeFelipe J. 1994. A study of SMI 32-stained pyramidal cells, parvalbumin-immunoreactive chandelier cells, and presumptive thalamocortical axons in the human temporal neocortex. J Comp Neurol 342(3):389-408.

Di Marco M, Sadun C, Port M, Guilbert I, Couvreur P, Dubernet C. 2007. Physicochemical characterization of ultrasmall superparamagnetic iron oxide particles (USPIO) for biomedical application as MRI contrast agents. Int J Nanomedicine 2(4):609-622.

Ding J, Tao K, Li J, Song S, Sun K. 2010. Cell-specific cytotoxicity of dextran-stabilized magnetite nanoparticles. Colloids Surf B Biointerfaces 79(1):184-190.

Dotti CG, Sullivan CA, Banker GA. 1988. The establishment of polarity by hippocampal neurons in culture. J Neurosci 8(4):1454-1468.

Dringen R, Bishop GM, Koeppe M, Dang TN, Robinson SR. 2007. The pivotal role of astrocytes in the metabolism of iron in the brain. Neurochem Res 32(11):1884-1890.

Eyo UB, Wu LJ. 2013. Bidirectional microglia-neuron communication in the healthy brain. Neural Plast 2013:456857.

Feng X, Xia Q, Yuan L, Yang X, Wang K. 2010. Impaired mitochondrial function and oxidative stress in rat cortical neurons: implications for gadolinium-induced neurotoxicity. Neurotoxicology 31(4):391-398.

Figge L, Appler F, Chen HH, Sosnovik DE, Schnorr J, Seitz O, Taupitz M, Hamm B, Schellenberger E. 2014. Direct coupling of annexin A5 to VSOP yields small, protein-covered nanoprobes for MR imaging of apoptosis. Contrast Media Mol Imaging 9(4):291-299.

Fleige G, Nolte C, Synowitz M, Seeberger F, Kettenmann H, Zimmer C. 2001. Magnetic labeling of activated microglia in experimental gliomas. Neoplasia 3(6):489-499.

Fletcher TL, Banker GA. 1989. The establishment of polarity by hippocampal neurons: the relationship between the stage of a cell's development in situ and its subsequent development in culture. Dev Biol 136(2):446-454.

Floden AM, Combs CK. 2007. Microglia repetitively isolated from in vitro mixed glial cultures retain their initial phenotype. J Neurosci Methods 164(2):218-224.

Frank JA, Kalish H, Jordan EK, Anderson SA, Pawelczyk E, Arbab AS. 2007. Color transformation and fluorescence of Prussian blue-positive cells: implications for histologic verification of cells labeled with superparamagnetic iron oxide nanoparticles. Mol Imaging 6(3):212-218.

Gendelman HE, Anantharam V, Bronich T, Ghaisas S, Jin H, Kanthasamy AG, Liu X, McMillan J, Mosley RL, Narasimhan B, Mallapragada SK. 2015. Nanoneuromedicines for degenerative, inflammatory, and infectious nervous system diseases. Nanomedicine 11(3):751-767.

Geppert M, Hohnholt M, Gaetjen L, Grunwald I, Baumer M, Dringen R. 2009. Accumulation of iron oxide nanoparticles by cultured brain astrocytes. J Biomed Nanotechnol 5(3):285-293.

Geppert M, Hohnholt MC, Nurnberger S, Dringen R. 2012. Ferritin up-regulation and transient ROS production in cultured brain astrocytes after loading with iron oxide nanoparticles. Acta Biomater 8(10):3832-3839.

Geppert M, Hohnholt MC, Thiel K, Nurnberger S, Grunwald I, Rezwan K, Dringen R. 2011. Uptake of dimercaptosuccinate-coated magnetic iron oxide nanoparticles by cultured brain astrocytes. Nanotechnology 22(14):145101.

Ginhoux F, Greter M, Leboeuf M, Nandi S, See P, Gokhan S, Mehler MF, Conway SJ, Ng LG, Stanley ER, Samokhvalov IM, Merad M. 2010. Fate mapping analysis reveals that adult microglia derive from primitive macrophages. Science 330(6005):841-845.

Goldmann T, Wieghofer P, Jordao MJ, Prutek F, Hagemeyer N, Frenzel K, Amann L, Staszewski O, Kierdorf K, Krueger M, Locatelli G, Hochgerner H, Zeiser R, Epelman S, Geissmann F, Priller J, Rossi FM, Bechmann I, Kerschensteiner M, Linnarsson S, Jung S, Prinz M. 2016. Origin, fate and dynamics of macrophages at central nervous system interfaces. Nat Immunol 17(7):797-805.

Gomez Perdiguero E, Klapproth K, Schulz C, Busch K, Azzoni E, Crozet L, Garner H, Trouillet C, de Bruijn MF, Geissmann F, Rodewald HR. 2015. Tissue-resident macrophages originate from yolk-sac-derived erythro-myeloid progenitors. Nature 518(7540):547-551.

Gonzalez-Perez O, Lopez-Virgen V, Quinones-Hinojosa A. 2015. Astrocytes: Everything but the glue. Neuroimmunol Neuroinflamm 2(2):115-117.

Gordon J, Amini S, White MK. 2013. General overview of neuronal cell culture. Methods Mol Biol 1078:1-8.

Gulani V, Calamante F, Shellock FG, Kanal E, Reeder SB, International Society for Magnetic Resonance in M. 2017. Gadolinium deposition in the brain: summary of evidence and recommendations. Lancet Neurol 16(7):564-570.

Gupta AK, Gupta M. 2005. Synthesis and surface engineering of iron oxide nanoparticles for biomedical applications. Biomaterials 26(18):3995-4021.

Hanisch UK. 2002. Microglia as a source and target of cytokines. Glia 40(2):140-155.

Hanisch UK, Kettenmann H. 2007. Microglia: active sensor and versatile effector cells in the normal and pathologic brain. Nat Neurosci 10(11):1387-1394.

Hansson E, Ronnback L, Persson LI, Lowenthal A, Noppe M, Alling C, Karlsson B. 1984. Cellular composition of primary cultures from cerebral cortex, striatum, hippocampus, brainstem and cerebellum. Brain Res 300(1):9-18.

Hare D, Ayton S, Bush A, Lei P. 2013. A delicate balance: Iron metabolism and diseases of the brain. Front Aging Neurosci 5:34.

Hasan DM, Amans M, Tihan T, Hess C, Guo Y, Cha S, Su H, Martin AJ, Lawton MT, Neuwelt EA, Saloner DA, Young WL. 2012. Ferumoxytol-enhanced MRI to Image Inflammation within Human Brain Arteriovenous Malformations: A Pilot Investigation. Transl Stroke Res 3(Suppl 1):166-173.

Hendrick RE, Haacke EM. 1993. Basic physics of MR contrast agents and maximization of image contrast. J Magn Reson Imaging 3(1):137-148.

Herculano-Houzel S. 2014. The glia/neuron ratio: how it varies uniformly across brain structures and species and what that means for brain physiology and evolution. Glia 62(9):1377-1391.

High WA, Ayers RA, Chandler J, Zito G, Cowper SE. 2007. Gadolinium is detectable within the tissue of patients with nephrogenic systemic fibrosis. J Am Acad Dermatol 56(1):21-26.

Hirsch V, Kinnear C, Moniatte M, Rothen-Rutishauser B, Clift MJ, Fink A. 2013. Surface charge of polymer coated SPIONs influences the serum protein adsorption, colloidal stability and subsequent cell interaction in vitro. Nanoscale 5(9):3723-3732.

Hoff D, Sheikh L, Bhattacharya S, Nayar S, Webster TJ. 2013. Comparison study of ferrofluid and powder iron oxide nanoparticle permeability across the blood-brain barrier. Int J Nanomedicine 8:703-710.

Hohnholt MC, Dringen R. 2013. Uptake and metabolism of iron and iron oxide nanoparticles in brain astrocytes. Biochem Soc Trans 41(6):1588-1592.

Hohnholt MC, Geppert M, Luther EM, Petters C, Bulcke F, Dringen R. 2013. Handling of iron oxide and silver nanoparticles by astrocytes. Neurochem Res 38(2):227-239.

Holder AL, Goth-Goldstein R, Lucas D, Koshland CP. 2012. Particle-induced artifacts in the MTT and LDH viability assays. Chem Res Toxicol 25(9):1885-1892.

Hong SC, Lee JH, Lee J, Kim HY, Park JY, Cho J, Lee J, Han DW. 2011. Subtle cytotoxicity and genotoxicity differences in superparamagnetic iron oxide nanoparticles coated with various functional groups. Int J Nanomedicine 6:3219-3231.

Horie M, Fujita K, Kato H, Endoh S, Nishio K, Komaba LK, Nakamura A, Miyauchi A, Kinugasa S, Hagihara Y, Niki E, Yoshida Y, Iwahashi H. 2012. Association of the physical and chemical

properties and the cytotoxicity of metal oxide nanoparticles: metal ion release, adsorption ability and specific surface area. Metallomics 4(4):350-360.

Horie M, Kato H, Iwahashi H. 2013. Cellular effects of manufactured nanoparticles: effect of adsorption ability of nanoparticles. Arch Toxicol 87(5):771-781.

Hu YL, Gao JQ. 2010. Potential neurotoxicity of nanoparticles. Int J Pharm 394(1-2):115-121.

Ichikawa M, Muramoto K, Kobayashi K, Kawahara M, Kuroda Y. 1993. Formation and maturation of synapses in primary cultures of rat cerebral cortical cells: an electron microscopic study. Neurosci Res 16(2):95-103.

Ittrich H, Peldschus K, Raabe N, Kaul M, Adam G. 2013. Superparamagnetic iron oxide nanoparticles in biomedicine: applications and developments in diagnostics and therapy. Rofo 185(12):1149-1166.

Iv M, Telischak N, Feng D, Holdsworth SJ, Yeom KW, Daldrup-Link HE. 2015. Clinical applications of iron oxide nanoparticles for magnetic resonance imaging of brain tumors. Nanomedicine (Lond) 10(6):993-1018.

Jakel S, Dimou L. 2017. Glial Cells and Their Function in the Adult Brain: A Journey through the History of Their Ablation. Front Cell Neurosci 11:24.

Jarockyte G, Daugelaite E, Stasys M, Statkute U, Poderys V, Tseng TC, Hsu SH, Karabanovas V, Rotomskis R. 2016. Accumulation and Toxicity of Superparamagnetic Iron Oxide Nanoparticles in Cells and Experimental Animals. Int J Mol Sci 17(8).

Jenkins SI, Pickard MR, Furness DN, Yiu HH, Chari DM. 2013. Differences in magnetic particle uptake by CNS neuroglial subclasses: implications for neural tissue engineering. Nanomedicine (Lond) 8(6):951-968.

Jones EV, Cook D, Murai KK. 2012. A neuron-astrocyte co-culture system to investigate astrocyte-secreted factors in mouse neuronal development. Methods Mol Biol 814:341-352.

Jozefczuk J, Adjaye J. 2011. Quantitative real-time PCR-based analysis of gene expression. Methods Enzymol 500:99-109.

Kaech S, Banker G. 2006. Culturing hippocampal neurons. Nat Protoc 1(5):2406-2415.

Kalani A, Tyagi A, Tyagi N. 2014. Exosomes: mediators of neurodegeneration, neuroprotection and therapeutics. Mol Neurobiol 49(1):590-600.

Kanda T, Oba H, Toyoda K, Kitajima K, Furui S. 2016. Brain gadolinium deposition after administration of gadolinium-based contrast agents. Jpn J Radiol 34(1):3-9.

Karlsson HL, Gustafsson J, Cronholm P, Moller L. 2009. Size-dependent toxicity of metal oxide particles--a comparison between nano- and micrometer size. Toxicol Lett 188(2):112-118.

Katsumoto A, Lu H, Miranda AS, Ransohoff RM. 2014. Ontogeny and functions of central nervous system macrophages. J Immunol 193(6):2615-2621.

Keaney J, Campbell M. 2015. The dynamic blood-brain barrier. FEBS J 282(21):4067-4079.

Kessler R. 2011. Engineered nanoparticles in consumer products: understanding a new ingredient. Environ Health Perspect 119(3):a120-125.

Kettenmann H, Hanisch UK, Noda M, Verkhratsky A. 2011. Physiology of microglia. Physiol Rev 91(2):461-553.

Kettenmann H, Verkhratsky A. 2008. Neuroglia: the 150 years after. Trends Neurosci 31(12):653-659.

Kierdorf K, Prinz M. 2013. Factors regulating microglia activation. Front Cell Neurosci 7:44.

Kim JA, Lee N, Kim BH, Rhee WJ, Yoon S, Hyeon T, Park TH. 2011. Enhancement of neurite outgrowth in PC12 cells by iron oxide nanoparticles. Biomaterials 32(11):2871-2877.

Kim JS, Yoon TJ, Yu KN, Kim BG, Park SJ, Kim HW, Lee KH, Park SB, Lee JK, Cho MH. 2006. Toxicity and tissue distribution of magnetic nanoparticles in mice. Toxicol Sci 89(1):338-347.

Kong SD, Lee J, Ramachandran S, Eliceiri BP, Shubayev VI, Lal R, Jin S. 2012. Magnetic targeting of nanoparticles across the intact blood-brain barrier. J Control Release 164(1):49-57.

Korzhevskii DE, Kirik OV. 2016. Brain Microglia and Microglial Markers. Neuroscience and Behavioral Physiology 46(3):284-290.

Kowalczyk M, Banach M, Rysz J. 2011. Ferumoxytol: a new era of iron deficiency anemia treatment for patients with chronic kidney disease. J Nephrol 24(6):717-722.

Krol S, Macrez R, Docagne F, Defer G, Laurent S, Rahman M, Hajipour MJ, Kehoe PG, Mahmoudi M. 2013. Therapeutic benefits from nanoparticles: the potential significance of nanoscience in diseases with compromise to the blood brain barrier. Chem Rev 113(3):1877-1903.

Kroll A, Pillukat MH, Hahn D, Schnekenburger J. 2009. Current in vitro methods in nanoparticle risk assessment: limitations and challenges. Eur J Pharm Biopharm 72(2):370-377.

Kroll A, Pillukat MH, Hahn D, Schnekenburger J. 2012. Interference of engineered nanoparticles with in vitro toxicity assays. Arch Toxicol 86(7):1123-1136.

Ladeby R, Wirenfeldt M, Garcia-Ovejero D, Fenger C, Dissing-Olesen L, Dalmau I, Finsen B. 2005. Microglial cell population dynamics in the injured adult central nervous system. Brain Res Brain Res Rev 48(2):196-206.

Lai LM, Cheng JY, Alley MT, Zhang T, Lustig M, Vasanawala SS. 2017. Feasibility of ferumoxytol-enhanced neonatal and young infant cardiac MRI without general anesthesia. J Magn Reson Imaging 45(5):1407-1418.

Lamkowsky MC, Geppert M, Schmidt MM, Dringen R. 2011. Magnetic field-induced acceleration of the accumulation of magnetic iron oxide nanoparticles by cultured brain astrocytes. J Biomed Mater Res A.

Lamkowsky MC, Geppert M, Schmidt MM, Dringen R. 2012. Magnetic field-induced acceleration of the accumulation of magnetic iron oxide nanoparticles by cultured brain astrocytes. J Biomed Mater Res A 100(2):323-334.

Laurent S, Forge D, Port M, Roch A, Robic C, Vander Elst L, Muller RN. 2008. Magnetic iron oxide nanoparticles: synthesis, stabilization, vectorization, physicochemical characterizations, and biological applications. Chem Rev 108(6):2064-2110.

Laux P, Tentschert J, Riebeling C, Braeuning A, Creutzenberg O, Epp A, Fessard V, Haas KH, Haase A, Hund-Rinke K, Jakubowski N, Kearns P, Lampen A, Rauscher H, Schoonjans R, Stormer A, Thielmann A, Muhle U, Luch A. 2018. Nanomaterials: certain aspects of application, risk assessment and risk communication. Arch Toxicol 92(1):121-141.

Levesque S, Taetzsch T, Lull ME, Kodavanti U, Stadler K, Wagner A, Johnson JA, Duke L, Kodavanti P, Surace MJ, Block ML. 2011. Diesel exhaust activates and primes microglia: air pollution, neuroinflammation, and regulation of dopaminergic neurotoxicity. Environ Health Perspect 119(8):1149-1155.

Levy M, Lagarde F, Maraloiu VA, Blanchin MG, Gendron F, Wilhelm C, Gazeau F. 2010. Degradability of superparamagnetic nanoparticles in a model of intracellular environment: follow-up of magnetic, structural and chemical properties. Nanotechnology 21(39):395103.

Lieu PT, Heiskala M, Peterson PA, Yang Y. 2001. The roles of iron in health and disease. Mol Aspects Med 22(1-2):1-87.

Lin MM, Kim DK, El Haj AJ, Dobson J. 2008a. Development of superparamagnetic iron oxide nanoparticles (SPIONS) for translation to clinical applications. IEEE Trans Nanobioscience 7(4):298-305.

Lin MM, Kim do K, El Haj AJ, Dobson J. 2008b. Development of superparamagnetic iron oxide nanoparticles (SPIONS) for translation to clinical applications. IEEE Trans Nanobioscience 7(4):298-305.

Liu B, Teschemacher AG, Kasparov S. 2017. Neuroprotective potential of astroglia. J Neurosci Res 95(11):2126-2139.

Liu G, Gao J, Ai H, Chen X. 2013. Applications and potential toxicity of magnetic iron oxide nanoparticles. Small 9(9-10):1533-1545.

Lockman PR, Koziara JM, Mumper RJ, Allen DD. 2004. Nanoparticle surface charges alter blood-brain barrier integrity and permeability. J Drug Target 12(9-10):635-641.

Lu M, Cohen MH, Rieves D, Pazdur R. 2010. FDA report: Ferumoxytol for intravenous iron therapy in adult patients with chronic kidney disease. Am J Hematol 85(5):315-319.

Ludwig A, Poller WC, Westphal K, Minkwitz S, Lattig-Tunnemann G, Metzkow S, Stangl K, Baumann G, Taupitz M, Wagner S, Schnorr J, Stangl V. 2013. Rapid binding of electrostatically stabilized iron oxide nanoparticles to THP-1 monocytic cells via interaction with glycosaminoglycans. Basic Res Cardiol 108(2):328.

Lull ME, Block ML. 2010. Microglial activation and chronic neurodegeneration. Neurotherapeutics 7(4):354-365.

Lunov O, Syrovets T, Rocker C, Tron K, Nienhaus GU, Rasche V, Mailander V, Landfester K, Simmet T. 2010. Lysosomal degradation of the carboxydextran shell of coated superparamagnetic iron oxide nanoparticles and the fate of professional phagocytes. Biomaterials 31(34):9015-9022.

Luther EM, Petters C, Bulcke F, Kaltz A, Thiel K, Bickmeyer U, Dringen R. 2013. Endocytotic uptake of iron oxide nanoparticles by cultured brain microglial cells. Acta Biomater 9(9):8454-8465.

Macco R, Pelizzoni I, Consonni A, Vitali I, Giacalone G, Martinelli Boneschi F, Codazzi F, Grohovaz F, Zacchetti D. 2013. Astrocytes acquire resistance to iron-dependent oxidative stress upon proinflammatory activation. J Neuroinflammation 10:130.

Mailander V, Lorenz MR, Holzapfel V, Musyanovych A, Fuchs K, Wiesneth M, Walther P, Landfester K, Schrezenmeier H. 2008. Carboxylated superparamagnetic iron oxide particles label cells intracellularly without transfection agents. Mol Imaging Biol 10(3):138-146.

Mairuae N, Connor JR, Cheepsunthorn P. 2011. Increased cellular iron levels affect matrix metalloproteinase expression and phagocytosis in activated microglia. Neurosci Lett 500(1):36-40.

Mao X, Xu J, Cui H. 2016. Functional nanoparticles for magnetic resonance imaging. Wiley Interdiscip Rev Nanomed Nanobiotechnol 8(6):814-841.

McConnell HL, Schwartz DL, Richardson BE, Woltjer RL, Muldoon LL, Neuwelt EA. 2016. Ferumoxytol nanoparticle uptake in brain during acute neuroinflammation is cell-specific. Nanomedicine 12(6):1535-1542.

Migliore L, Uboldi C, Di Bucchianico S, Coppede F. 2015. Nanomaterials and neurodegeneration. Environ Mol Mutagen 56(2):149-170.

Millward JM, Ariza de Schellenberger A, Berndt D, Hanke-Vela L, Schellenberger E, Waiczies S, Taupitz M, Kobayashi Y, Wagner S, Infante-Duarte C. 2017. Application of Europium-Doped Very Small Iron Oxide Nanoparticles to Visualize Neuroinflammation with MRI and Fluorescence Microscopy. Neuroscience.

Millward JM, Schnorr J, Taupitz M, Wagner S, Wuerfel JT, Infante-Duarte C. 2013. Iron oxide magnetic nanoparticles highlight early involvement of the choroid plexus in central nervous system inflammation. ASN Neuro 5(1):e00110.

Minghetti L, Ajmone-Cat MA, De Berardinis MA, De Simone R. 2005. Microglial activation in chronic neurodegenerative diseases: roles of apoptotic neurons and chronic stimulation. Brain Res Brain Res Rev 48(2):251-256.

Muller EK, Grafe C, Wiekhorst F, Bergemann C, Weidner A, Dutz S, Clement JH. 2018. Magnetic Nanoparticles Interact and Pass an In Vitro Co-Culture Blood-Placenta Barrier Model. Nanomaterials (Basel) 8(2).

Nakayama AY, Harms MB, Luo L. 2000. Small GTPases Rac and Rho in the maintenance of dendritic spines and branches in hippocampal pyramidal neurons. J Neurosci 20(14):5329-5338.

Napoli I, Neumann H. 2009. Microglial clearance function in health and disease. Neuroscience 158(3):1030-1038.

Nel A, Xia T, Madler L, Li N. 2006. Toxic potential of materials at the nanolevel. Science 311(5761):622-627.

Neubert J, Brauer AU. 2015. Superparamagnetic iron oxide nanoparticles: promote neuronal regenerative capacity? Neural Regen Res 10(10):1568-1569.

Neubert J, Glumm J. 2016. Promoting neuronal regeneration using extracellular vesicles loaded with superparamagnetic iron oxide nanoparticles. Neural Regen Res 11(1):61-63.

Neubert J, Wagner S, Kiwit J, Brauer AU, Glumm J. 2015. New findings about iron oxide nanoparticles and their different effects on murine primary brain cells. Int J Nanomedicine 10:2033-2049.

Neuwelt EA, Hamilton BE, Varallyay CG, Rooney WR, Edelman RD, Jacobs PM, Watnick SG. 2009. Ultrasmall superparamagnetic iron oxides (USPIOs): a future alternative magnetic resonance (MR) contrast agent for patients at risk for nephrogenic systemic fibrosis (NSF)? Kidney Int 75(5):465-474.

Ni M, Aschner M. 2010. Neonatal rat primary microglia: isolation, culturing, and selected applications. Curr Protoc Toxicol Chapter 12:Unit 12 17.

Nimmerjahn A, Kirchhoff F, Helmchen F. 2005. Resting microglial cells are highly dynamic surveillants of brain parenchyma in vivo. Science 308(5726):1314-1318.

O'Donnell M, Chance RK, Bashaw GJ. 2009. Axon growth and guidance: receptor regulation and signal transduction. Annu Rev Neurosci 32:383-412.

Oberdorster G, Elder A, Rinderknecht A. 2009. Nanoparticles and the brain: cause for concern? J Nanosci Nanotechnol 9(8):4996-5007.

Oberdorster G, Maynard A, Donaldson K, Castranova V, Fitzpatrick J, Ausman K, Carter J, Karn B, Kreyling W, Lai D, Olin S, Monteiro-Riviere N, Warheit D, Yang H, Group IRFRSINTSW. 2005. Principles for characterizing the potential human health effects from exposure to nanomaterials: elements of a screening strategy. Part Fibre Toxicol 2:8.

Oberheim NA, Goldman SA, Nedergaard M. 2012. Heterogeneity of astrocytic form and function. Methods Mol Biol 814:23-45.

Pai AB, Nielsen JC, Kausz A, Miller P, Owen JS. 2010. Plasma pharmacokinetics of two consecutive doses of ferumoxytol in healthy subjects. Clin Pharmacol Ther 88(2):237-242.

Pais TF, Figueiredo C, Peixoto R, Braz MH, Chatterjee S. 2008. Necrotic neurons enhance microglial neurotoxicity through induction of glutaminase by a MyD88-dependent pathway. J Neuroinflammation 5:43.

Paolicelli RC, Bolasco G, Pagani F, Maggi L, Scianni M, Panzanelli P, Giustetto M, Ferreira TA, Guiducci E, Dumas L, Ragozzino D, Gross CT. 2011. Synaptic pruning by microglia is necessary for normal brain development. Science 333(6048):1456-1458.

Papastefanaki F, Jakovcevski I, Poulia N, Djogo N, Schulz F, Martinovic T, Ciric D, Loers G, Vossmeyer T, Weller H, Schachner M, Matsas R. 2015. Intraspinal Delivery of Polyethylene Glycol-coated Gold Nanoparticles Promotes Functional Recovery After Spinal Cord Injury. Mol Ther 23(6):993-1002.

Park LC, Zhang H, Gibson GE. 2001. Co-culture with astrocytes or microglia protects metabolically impaired neurons. Mech Ageing Dev 123(1):21-27.

Parkhurst CN, Yang G, Ninan I, Savas JN, Yates JR, 3rd, Lafaille JJ, Hempstead BL, Littman DR, Gan WB. 2013. Microglia promote learning-dependent synapse formation through brain-derived neurotrophic factor. Cell 155(7):1596-1609.

Pasquini L, Napolitano A, Visconti E, Longo D, Romano A, Toma P, Espagnet MCR. 2018. Gadolinium-Based Contrast Agent-Related Toxicities. CNS Drugs 32(3):229-240.

Pekny M, Pekna M, Messing A, Steinhauser C, Lee JM, Parpura V, Hol EM, Sofroniew MV, Verkhratsky A. 2016. Astrocytes: a central element in neurological diseases. Acta Neuropathol 131(3):323-345.

Pelizzoni I, Zacchetti D, Campanella A, Grohovaz F, Codazzi F. 2013. Iron uptake in quiescent and inflammation-activated astrocytes: a potentially neuroprotective control of iron burden. Biochim Biophys Acta 1832(8):1326-1333.

Perl DP, Good PF. 1992. Comparative techniques for determining cellular iron distribution in brain tissues. Ann Neurol 32 Suppl:S76-81.

Pernet V, Schwab ME. 2014. Lost in the jungle: new hurdles for optic nerve axon regeneration. Trends Neurosci 37(7):381-387.

Peters DG, Connor JR. 2014. Introduction to cells comprising the nervous system. Adv Neurobiol 9:33-45.

Petry KG, Boiziau C, Dousset V, Brochet B. 2007. Magnetic resonance imaging of human brain macrophage infiltration. Neurotherapeutics 4(3):434-442.

Petters C, Dringen R. 2015. Accumulation of iron oxide nanoparticles by cultured primary neurons. Neurochem Int 81:1-9.

Petters C, Irrsack E, Koch M, Dringen R. 2014. Uptake and metabolism of iron oxide nanoparticles in brain cells. Neurochem Res 39(9):1648-1660.

Petters C, Thiel K, Dringen R. 2016. Lysosomal iron liberation is responsible for the vulnerability of brain microglial cells to iron oxide nanoparticles: comparison with neurons and astrocytes. Nanotoxicology 10(3):332-342.

Pettitt ME, Lead JR. 2013. Minimum physicochemical characterisation requirements for nanomaterial regulation. Environ Int 52:41-50.

Pickard MR, Chari DM. 2010. Robust uptake of magnetic nanoparticles (MNPs) by central nervous system (CNS) microglia: implications for particle uptake in mixed neural cell populations. Int J Mol Sci 11(3):967-981.

Pierre VC, Allen MJ, Caravan P. 2014. Contrast agents for MRI: 30+ years and where are we going? J Biol Inorg Chem 19(2):127-131.

Pinkernelle J, Calatayud P, Goya GF, Fansa H, Keilhoff G. 2012. Magnetic nanoparticles in primary neural cell cultures are mainly taken up by microglia. BMC Neurosci 13:32.

Pisanic TR, 2nd, Blackwell JD, Shubayev VI, Finones RR, Jin S. 2007. Nanotoxicity of iron oxide nanoparticle internalization in growing neurons. Biomaterials 28(16):2572-2581.

Pita-Thomas W, Steketee MB, Moysidis SN, Thakor K, Hampton B, Goldberg JL. 2015. Promoting filopodial elongation in neurons by membrane-bound magnetic nanoparticles. Nanomedicine 11(3):559-567.

Pohland M, Glumm R, Wiekhorst F, Kiwit J, Glumm J. 2017. Biocompatibility of very small superparamagnetic iron oxide nanoparticles in murine organotypic hippocampal slice cultures and the role of microglia. Int J Nanomedicine 12:1577-1591.

Polak P, Shefi O. 2015. Nanometric agents in the service of neuroscience: Manipulation of neuronal growth and activity using nanoparticles. Nanomedicine 11(6):1467-1479.

Poller WC, Lowa N, Wiekhorst F, Taupitz M, Wagner S, Moller K, Baumann G, Stangl V, Trahms L, Ludwig A. 2016a. Magnetic Particle Spectroscopy Reveals Dynamic Changes in the Magnetic Behavior of Very Small Superparamagnetic Iron Oxide Nanoparticles During Cellular Uptake and Enables Determination of Cell-Labeling Efficacy. J Biomed Nanotechnol 12(2):337-346.

Poller WC, Ramberger E, Boehm-Sturm P, Mueller S, Möller K, Löwa N, Wiekhorst F, Wagner S, Taupitz M, Schellenberger E, Baumann G, Stangl K, Stangl V, Ludwig A. 2016b. Uptake of citrate-coated iron oxide nanoparticles into atherosclerotic lesions in mice occurs via accelerated transcytosis through plaque endothelial cells. Nano Research 9(11):3437-3452.

Prince MR, Zhang HL, Chabra SG, Jacobs P, Wang Y. 2003. A pilot investigation of new superparamagnetic iron oxide (ferumoxytol) as a contrast agent for cardiovascular MRI. J Xray Sci Technol 11(4):231-240.

Prinz M, Priller J, Sisodia SS, Ransohoff RM. 2011. Heterogeneity of CNS myeloid cells and their roles in neurodegeneration. Nat Neurosci 14(10):1227-1235.

Ragnaill MN, Brown M, Ye D, Bramini M, Callanan S, Lynch I, Dawson KA. 2011. Internal benchmarking of a human blood-brain barrier cell model for screening of nanoparticle uptake and transcytosis. Eur J Pharm Biopharm 77(3):360-367.

Ransohoff RM, Perry VH. 2009. Microglial physiology: unique stimuli, specialized responses. Annu Rev Immunol 27:119-145.

Reimer P, Balzer T. 2003. Ferucarbotran (Resovist): a new clinically approved RES-specific contrast agent for contrast-enhanced MRI of the liver: properties, clinical development, and applications. Eur Radiol 13(6):1266-1276.

Riemer J, Hoepken HH, Czerwinska H, Robinson SR, Dringen R. 2004. Colorimetric ferrozine-based assay for the quantitation of iron in cultured cells. Anal Biochem 331(2):370-375.

Rivet CJ, Yuan Y, Borca-Tasciuc DA, Gilbert RJ. 2012. Altering iron oxide nanoparticle surface properties induce cortical neuron cytotoxicity. Chem Res Toxicol 25(1):153-161.

Rock RB, Gekker G, Hu S, Sheng WS, Cheeran M, Lokensgard JR, Peterson PK. 2004. Role of microglia in central nervous system infections. Clin Microbiol Rev 17(4):942-964, table of contents.

Roohi F, Lohrke J, Ide A, Schutz G, Dassler K. 2012. Studying the effect of particle size and coating type on the blood kinetics of superparamagnetic iron oxide nanoparticles. Int J Nanomedicine 7:4447-4458.

Rosario M, Schuster S, Juttner R, Parthasarathy S, Tarabykin V, Birchmeier W. 2012. Neocortical dendritic complexity is controlled during development by NOMA-GAP-dependent inhibition of Cdc42 and activation of cofilin. Genes Dev 26(15):1743-1757.

Rosenberg JT, Sachi-Kocher A, Davidson MW, Grant SC. 2012. Intracellular SPIO labeling of microglia: high field considerations and limitations for MR microscopy. Contrast Media Mol Imaging 7(2):121-129.

Rouault TA. 2013. Iron metabolism in the CNS: implications for neurodegenerative diseases. Nat Rev Neurosci 14(8):551-564.

Ruangwattanapaisarn N, Hsiao A, Vasanawala SS. 2015. Ferumoxytol as an off-label contrast agent in body 3T MR angiography: a pilot study in children. Pediatr Radiol 45(6):831-839.

Rumenapp C, Gleich B, Haase A. 2012. Magnetic nanoparticles in magnetic resonance imaging and diagnostics. Pharm Res 29(5):1165-1179.

Sadrzadeh SM, Saffari Y. 2004. Iron and brain disorders. Am J Clin Pathol 121 Suppl:S64-70.

Safety Guidelines of the International Conference for Harmonization. ICH harmonisation for better health.

Safi M, Courtois J, Seigneuret M, Conjeaud H, Berret JF. 2011. The effects of aggregation and protein corona on the cellular internalization of iron oxide nanoparticles. Biomaterials 32(35):9353-9363.

Saito S, Tsugeno M, Koto D, Mori Y, Yoshioka Y, Nohara S, Murase K. 2012. Impact of surface coating and particle size on the uptake of small and ultrasmall superparamagnetic iron oxide nanoparticles by macrophages. Int J Nanomedicine 7:5415-5421.

Sakulkhu U, Mahmoudi M, Maurizi L, Salaklang J, Hofmann H. 2014. Protein corona composition of superparamagnetic iron oxide nanoparticles with various physico-chemical properties and coatings. Sci Rep 4:5020.

Salata O. 2004. Applications of nanoparticles in biology and medicine. J Nanobiotechnology 2(1):3.

Salter MW, Stevens B. 2017. Microglia emerge as central players in brain disease. Nat Med 23(9):1018-1027.

Saraiva C, Praca C, Ferreira R, Santos T, Ferreira L, Bernardino L. 2016. Nanoparticle-mediated brain drug delivery: Overcoming blood-brain barrier to treat neurodegenerative diseases. J Control Release 235:34-47.

Saura J, Tusell JM, Serratosa J. 2003. High-yield isolation of murine microglia by mild trypsinization. Glia 44(3):183-189.

Scalettar BA. 2006. How neurosecretory vesicles release their cargo. Neuroscientist 12(2):164-176.

Schaub NJ, Rende D, Yuan Y, Gilbert RJ, Borca-Tasciuc DA. 2014. Reduced astrocyte viability at physiological temperatures from magnetically activated iron oxide nanoparticles. Chem Res Toxicol 27(12):2023-2035.

Schieda N. 2013. Parenteral ferumoxytol interaction with magnetic resonance imaging: a case report, review of the literature and advisory warning. Insights Imaging 4(4):509-512.

Schmalenbach C, Muller HW. 1993. Astroglia-neuron interactions that promote long-term neuronal survival. J Chem Neuroanat 6(4):229-237.

Schweiger C, Hartmann R, Zhang F, Parak WJ, Kissel TH, Rivera Gil P. 2012. Quantification of the internalization patterns of superparamagnetic iron oxide nanoparticles with opposite charge. J Nanobiotechnology 10:28.

Serlin Y, Shelef I, Knyazer B, Friedman A. 2015. Anatomy and physiology of the blood-brain barrier. Semin Cell Dev Biol 38:2-6.

Shokrollahi H. 2013. Contrast agents for MRI. Mater Sci Eng C Mater Biol Appl 33(8):4485-4497.

Sholl DA. 1953. Dendritic organization in the neurons of the visual and motor cortices of the cat. J Anat 87(4):387-406.

Shubayev VI, Pisanic TR, 2nd, Jin S. 2009. Magnetic nanoparticles for theragnostics. Adv Drug Deliv Rev 61(6):467-477.

Sierra A, Abiega O, Shahraz A, Neumann H. 2013. Janus-faced microglia: beneficial and detrimental consequences of microglial phagocytosis. Front Cell Neurosci 7:6.

Silva Adaya D, Aguirre-Cruz L, Guevara J, Ortiz-Islas E. 2017. Nanobiomaterials' applications in neurodegenerative diseases. J Biomater Appl 31(7):953-984.

Silva GA. 2010. Nanotechnology applications and approaches for neuroregeneration and drug delivery to the central nervous system. Ann N Y Acad Sci 1199:221-230.

Small SA, Schobel SA, Buxton RB, Witter MP, Barnes CA. 2011. A pathophysiological framework of hippocampal dysfunction in ageing and disease. Nat Rev Neurosci 12(10):585-601.

Smith JA, Das A, Ray SK, Banik NL. 2012. Role of pro-inflammatory cytokines released from microglia in neurodegenerative diseases. Brain Res Bull 87(1):10-20.

Soenen SJ, Himmelreich U, Nuytten N, De Cuyper M. 2011. Cytotoxic effects of iron oxide nanoparticles and implications for safety in cell labelling. Biomaterials 32(1):195-205.

Soenen SJ, Himmelreich U, Nuytten N, Pisanic TR, 2nd, Ferrari A, De Cuyper M. 2010a. Intracellular nanoparticle coating stability determines nanoparticle diagnostics efficacy and cell functionality. Small 6(19):2136-2145.

Soenen SJ, Nuytten N, De Meyer SF, De Smedt SC, De Cuyper M. 2010b. High intracellular iron oxide nanoparticle concentrations affect cellular cytoskeleton and focal adhesion kinase-mediated signaling. Small 6(7):832-842.

Sofroniew MV. 2014. Astrogliosis. Cold Spring Harb Perspect Biol 7(2):a020420.

Sofroniew MV, Vinters HV. 2010. Astrocytes: biology and pathology. Acta Neuropathol 119(1):7-35.

Sousa C, Biber K, Michelucci A. 2017. Cellular and Molecular Characterization of Microglia: A Unique Immune Cell Population. Front Immunol 8:198.

Spinowitz BS, Kausz AT, Baptista J, Noble SD, Sothinathan R, Bernardo MV, Brenner L, Pereira BJ. 2008. Ferumoxytol for treating iron deficiency anemia in CKD. J Am Soc Nephrol 19(8):1599-1605.

Steketee MB, Moysidis SN, Jin XL, Weinstein JE, Pita-Thomas W, Raju HB, Iqbal S, Goldberg JL. 2011. Nanoparticle-mediated signaling endosome localization regulates growth cone motility and neurite growth. Proc Natl Acad Sci U S A 108(47):19042-19047.

Stroh A, Zimmer C, Werner N, Gertz K, Weir K, Kronenberg G, Steinbrink J, Mueller S, Sieland K, Dirnagl U, Nickenig G, Endres M. 2006. Tracking of systemically administered mononuclear cells in the ischemic brain by high-field magnetic resonance imaging. Neuroimage 33(3):886-897.

Sun Z, Worden M, Wroczynskyj Y, Yathindranath V, van Lierop J, Hegmann T, Miller DW. 2014. Magnetic field enhanced convective diffusion of iron oxide nanoparticles in an osmotically disrupted cell culture model of the blood-brain barrier. Int J Nanomedicine 9:3013-3026.

Sun Z, Yathindranath V, Worden M, Thliveris JA, Chu S, Parkinson FE, Hegmann T, Miller DW. 2013. Characterization of cellular uptake and toxicity of aminosilane-coated iron oxide nanoparticles with different charges in central nervous system-relevant cell culture models. Int J Nanomedicine 8:961-970.

Takano K, Nakamura Y, Yoneda Y. 2003. Microglial cell death induced by a low concentration of polyamines. Neuroscience 120(4):961-967.

Tamashiro TT, Dalgard CL, Byrnes KR. 2012. Primary microglia isolation from mixed glial cell cultures of neonatal rat brain tissue. J Vis Exp(66):e3814.

Taupitz M, Schmitz S, Hamm B. 2003. [Superparamagnetic iron oxide particles: current state and future development]. Rofo 175(6):752-765.

Taupitz M, Schnorr J, Abramjuk C, Wagner S, Pilgrimm H, Hunigen H, Hamm B. 2000. New generation of monomer-stabilized very small superparamagnetic iron oxide particles (VSOP) as contrast medium for MR angiography: preclinical results in rats and rabbits. J Magn Reson Imaging 12(6):905-911.

Taupitz M, Wagner S, Schnorr J, Kravec I, Pilgrimm H, Bergmann-Fritsch H, Hamm B. 2004. Phase I clinical evaluation of citrate-coated monocrystalline very small superparamagnetic iron oxide particles as a new contrast medium for magnetic resonance imaging. Invest Radiol 39(7):394-405.

Tay TL, Savage JC, Hui CW, Bisht K, Tremblay ME. 2017. Microglia across the lifespan: from origin to function in brain development, plasticity and cognition. J Physiol 595(6):1929-1945.

Thompson EM, Guillaume DJ, Dosa E, Li X, Nazemi KJ, Gahramanov S, Hamilton BE, Neuwelt EA. 2012. Dual contrast perfusion MRI in a single imaging session for assessment of pediatric brain tumors. J Neurooncol 109(1):105-114.

Thomsen LB, Linemann T, Pondman KM, Lichota J, Kim KS, Pieters RJ, Visser GM, Moos T. 2013. Uptake and transport of superparamagnetic iron oxide nanoparticles through human brain capillary endothelial cells. ACS Chem Neurosci 4(10):1352-1360.

Tiffany-Castiglion E, Qian Y. 2001. Astroglia as metal depots: molecular mechanisms for metal accumulation, storage and release. Neurotoxicology 22(5):577-592.

Toth GB, Varallyay CG, Horvath A, Bashir MR, Choyke PL, Daldrup-Link HE, Dosa E, Finn JP, Gahramanov S, Harisinghani M, Macdougall I, Neuwelt A, Vasanawala SS, Ambady P, Barajas R, Cetas JS, Ciporen J, DeLoughery TJ, Doolittle ND, Fu R, Grinstead J, Guimaraes AR, Hamilton BE, Li X, McConnell HL, Muldoon LL, Nesbit G, Netto JP, Petterson D, Rooney WD, Schwartz D, Szidonya L, Neuwelt EA. 2017. Current and potential imaging applications of ferumoxytol for magnetic resonance imaging. Kidney Int 92(1):47-66.

Town T, Nikolic V, Tan J. 2005. The microglial "activation" continuum: from innate to adaptive responses. J Neuroinflammation 2:24.

Tysiak E, Asbach P, Aktas O, Waiczies H, Smyth M, Schnorr J, Taupitz M, Wuerfel J. 2009. Beyond blood brain barrier breakdown - in vivo detection of occult neuroinflammatory foci by magnetic nanoparticles in high field MRI. J Neuroinflammation 6:20.

Urrutia PJ, Mena NP, Nunez MT. 2014. The interplay between iron accumulation, mitochondrial dysfunction, and inflammation during the execution step of neurodegenerative disorders. Front Pharmacol 5:38.

Valdiglesias V, Kilic G, Costa C, Fernandez-Bertolez N, Pasaro E, Teixeira JP, Laffon B. 2015. Effects of iron oxide nanoparticles: cytotoxicity, genotoxicity, developmental toxicity, and neurotoxicity. Environ Mol Mutagen 56(2):125-148.

Vasanawala SS, Nguyen KL, Hope MD, Bridges MD, Hope TA, Reeder SB, Bashir MR. 2016. Safety and technique of ferumoxytol administration for MRI. Magn Reson Med 75(5):2107-2111.

Verma A, Stellacci F. 2010. Effect of surface properties on nanoparticle-cell interactions. Small 6(1):12-21.

von Bartheld CS, Bahney J, Herculano-Houzel S. 2016. The search for true numbers of neurons and glial cells in the human brain: A review of 150 years of cell counting. J Comp Neurol 524(18):3865-3895.

von Zahn J, Moller T, Kettenmann H, Nolte C. 1997. Microglial phagocytosis is modulated by pro- and anti-inflammatory cytokines. Neuroreport 8(18):3851-3856.

Wadghiri YZ, Li J, Wang J, Hoang DM, Sun Y, Xu H, Tsui W, Li Y, Boutajangout A, Wang A, de Leon M, Wisniewski T. 2013. Detection of amyloid plaques targeted by bifunctional USPIO in Alzheimer's disease transgenic mice using magnetic resonance microimaging. PLoS One 8(2):e57097.

Wagner M, Wagner S, Schnorr J, Schellenberger E, Kivelitz D, Krug L, Dewey M, Laule M, Hamm B, Taupitz M. 2011. Coronary MR angiography using citrate-coated very small superparamagnetic iron oxide particles as blood-pool contrast agent: initial experience in humans. J Magn Reson Imaging 34(4):816-823.

Wagner S, Schnorr J, Ludwig A, Stangl V, Ebert M, Hamm B, Taupitz M. 2013. Contrast-enhanced MR imaging of atherosclerosis using citrate-coated superparamagnetic iron oxide nanoparticles: calcifying microvesicles as imaging target for plaque characterization. Int J Nanomedicine 8:767-779.

Wahajuddin, Arora S. 2012. Superparamagnetic iron oxide nanoparticles: magnetic nanoplatforms as drug carriers. Int J Nanomedicine 7:3445-3471.

Walker FR, Beynon SB, Jones KA, Zhao Z, Kongsui R, Cairns M, Nilsson M. 2014. Dynamic structural remodelling of microglia in health and disease: a review of the models, the signals and the mechanisms. Brain Behav Immun 37:1-14.

Walter L, Neumann H. 2009. Role of microglia in neuronal degeneration and regeneration. Semin Immunopathol 31(4):513-525.

Wang J, Chen Y, Chen B, Ding J, Xia G, Gao C, Cheng J, Jin N, Zhou Y, Li X, Tang M, Wang XM. 2010. Pharmacokinetic parameters and tissue distribution of magnetic Fe(3)O(4) nanoparticles in mice. Int J Nanomedicine 5:861-866.

Wang Y, Wang B, Zhu MT, Li M, Wang HJ, Wang M, Ouyang H, Chai ZF, Feng WY, Zhao YL. 2011. Microglial activation, recruitment and phagocytosis as linked phenomena in ferric oxide nanoparticle exposure. Toxicol Lett 205(1):26-37.

Wang YX. 2011. Superparamagnetic iron oxide based MRI contrast agents: Current status of clinical application. Quant Imaging Med Surg 1(1):35-40.

Wang YX, Hussain SM, Krestin GP. 2001. Superparamagnetic iron oxide contrast agents: physicochemical characteristics and applications in MR imaging. Eur Radiol 11(11):2319-2331.

Wei H, Bruns OT, Kaul MG, Hansen EC, Barch M, Wisniowska A, Chen O, Chen Y, Li N, Okada S, Cordero JM, Heine M, Farrar CT, Montana DM, Adam G, Ittrich H, Jasanoff A, Nielsen P, Bawendi MG. 2017. Exceedingly small iron oxide nanoparticles as positive MRI contrast agents. Proc Natl Acad Sci U S A 114(9):2325-2330.

Weinstein JS, Varallyay CG, Dosa E, Gahramanov S, Hamilton B, Rooney WD, Muldoon LL, Neuwelt EA. 2010. Superparamagnetic iron oxide nanoparticles: diagnostic magnetic resonance imaging and potential therapeutic applications in neurooncology and central nervous system inflammatory pathologies, a review. J Cereb Blood Flow Metab 30(1):15-35.

Weise G, Stoll G. 2012. Magnetic resonance imaging of blood brain/nerve barrier dysfunction and leukocyte infiltration: closely related or discordant? Front Neurol 3:178.

Wilhelm C, Billotey C, Roger J, Pons JN, Bacri JC, Gazeau F. 2003. Intracellular uptake of anionic superparamagnetic nanoparticles as a function of their surface coating. Biomaterials 24(6):1001-1011.

Wu HY, Chung MC, Wang CC, Huang CH, Liang HJ, Jan TR. 2013a. Iron oxide nanoparticles suppress the production of IL-1beta via the secretory lysosomal pathway in murine microglial cells. Part Fibre Toxicol 10:46.

Wu J, Ding T, Sun J. 2013b. Neurotoxic potential of iron oxide nanoparticles in the rat brain striatum and hippocampus. Neurotoxicology 34:243-253.

Wu W, Wu Z, Yu T, Jiang C, Kim WS. 2015a. Recent progress on magnetic iron oxide nanoparticles: synthesis, surface functional strategies and biomedical applications. Sci Technol Adv Mater 16(2):023501.

Wu Y, Dissing-Olesen L, MacVicar BA, Stevens B. 2015b. Microglia: Dynamic Mediators of Synapse Development and Plasticity. Trends Immunol 36(10):605-613.

Wuerfel E, Smyth M, Millward JM, Schellenberger E, Glumm J, Prozorovski T, Aktas O, Schulze-Topphoff U, Schnorr J, Wagner S, Taupitz M, Infante-Duarte C, Wuerfel J. 2011. Electrostatically Stabilized Magnetic Nanoparticles - An Optimized Protocol to Label Murine T Cells for in vivo MRI. Front Neurol 2:72.

Xue Y, Wu J, Sun J. 2012. Four types of inorganic nanoparticles stimulate the inflammatory reaction in brain microglia and damage neurons in vitro. Toxicol Lett 214(2):91-98.

Yang CY, Tai MF, Lin CP, Lu CW, Wang JL, Hsiao JK, Liu HM. 2011a. Mechanism of cellular uptake and impact of ferucarbotran on macrophage physiology. PLoS One 6(9):e25524.

Yang J, Wadghiri YZ, Hoang DM, Tsui W, Sun Y, Chung E, Li Y, Wang A, de Leon M, Wisniewski T. 2011b. Detection of amyloid plaques targeted by USPIO-Abeta1-42 in Alzheimer's disease transgenic mice using magnetic resonance microimaging. Neuroimage 55(4):1600-1609.

Yang Z, Liu ZW, Allaker RP, Reip P, Oxford J, Ahmad Z, Ren G. 2010. A review of nanoparticle functionality and toxicity on the central nervous system. J R Soc Interface 7 Suppl 4:S411-422.

Yarjanli Z, Ghaedi K, Esmaeili A, Rahgozar S, Zarrabi A. 2017. Iron oxide nanoparticles may damage to the neural tissue through iron accumulation, oxidative stress, and protein aggregation. BMC Neurosci 18(1):51.

Ye L, Huang Y, Zhao L, Li Y, Sun L, Zhou Y, Qian G, Zheng JC. 2013. IL-1beta and TNF-alpha induce neurotoxicity through glutamate production: a potential role for neuronal glutaminase. J Neurochem 125(6):897-908.

Zhang D, Fa HB, Zhou JT, Li S, Diao XW, Yin W. 2015. The detection of beta-amyloid plaques in an Alzheimer's disease rat model with DDNP-SPIO. Clin Radiol 70(1):74-80.

Zhang S, Li J, Lykotrafitis G, Bao G, Suresh S. 2009. Size-Dependent Endocytosis of Nanoparticles. Adv Mater 21:419-424.

Zhang W, Yan ZF, Gao JH, Sun L, Huang XY, Liu Z, Yu SY, Cao CJ, Zuo LJ, Chen ZJ, Hu Y, Wang F, Hong JS, Wang XM. 2014. Role and mechanism of microglial activation in iron-induced selective and progressive dopaminergic neurodegeneration. Mol Neurobiol 49(3):1153-1165.

Zielasek J, Hartung HP. 1996. Molecular mechanisms of microglial activation. Adv Neuroimmunol 6(2):191-122.

Curriculum vitae

For reasons of data protection,

the curriculum vitae is not included in the online version

For reasons of data protection,

the curriculum vitae is not included in the online version

For reasons of data protection,

the curriculum vitae is not included in the online version

Publications

Neubert J, Glumm J. Promoting neuronal regeneration using extracellular vesicles loaded with superparamagnetic iron oxide nanoparticles. *Neural Regen Res*. 2016 11(1):61-3.

Neubert J, Bräuer AU. Superparamagnetic iron oxide nanoparticles: promote neuronal regenerative capacity? *Neural Regen Res*. 2015 10(10):1568-9.

Neubert J, Wagner S, Kiwit J, Braeuer AU, Glumm J. New findings about iron oxide nanoparticles and their different effects on murine primary brain cells. *Int J Nanomedicine.* 2015; 10:2033-49

Eidesstattliche Versicherung

Hiermit versichere ich, Jenni Neubert, dass ich diese Doktorarbeit mit dem Titel „*Effects of clinically relevant superparamagnetic iron oxide nanoparticles on murine primary brain cells*“ selbständig und ohne fremde Hilfe verfasst, und keine anderen als die angegebenen Hilfsmittel verwendet habe. In der Arbeit sind die dem Wortlaut oder dem Sinne nach anderen Werken entnommen wurden unter Angabe der Quelle kenntlich gemacht.

Durchgeführt wurde der experimentelle Teil dieser Arbeit unter der Betreuung durch Dr. med. Jana Glumm von April 2014 bis April 2018 am Institut für Zell- und Neurobiologie der Charité – Universitätsmedizin Berlin, Deutschland.

Acknowledgement

First of all, I would like to thank my family for the constant supports in any of my decisions. Thank you so much! Without you, I would not be where I am now.

I'm also very grateful for the constant support by my very good friend Dr. Tim Wanger, who always finds the right, smart words to encourage and inspire me. I appreciate our friendship a lot.

Many thanks also to my very good friend Dr. Philipp Bethge. Thank you for your scientific advice and everything beyond.

I would like to thank my supervisor Dr. med. Jana Glumm. Thank you for offering me the position in your research group to experience this wonderful working atmosphere. I also appreciate that you gave me the freedom to work independently and that you always tried to ensure my financial support.

I would also like to thank Prof. Dr. Ursula Koch for agreeing to be a reviewer of this thesis.

A big thank you to Prof. Dr. Anja Bräuer. Thank you for the productive collaboration, the scientific support and the evening talks. Your support helped me a lot to move forward with my research.

I would like to thank PD. Dr. Ulf Strauß for helping me out with all different kinds of statistics during my time at the Institute of Cell and Neurobiology, and providing very good coffee. Your scientific advice helped me a lot.

I also very appreciated the collaboration with Dr. Susanne Wagner and Prof Dr. Matthias Taupitz during the time of the clinical research group KFO213. I always enjoyed the group meetings, which also gave me lots of motivation for my research.

Moreover, I would like to thank all the people that created such a nice working environment at the Charité. Many thanks to my colleague Martin Poland, who introduced me to the institute and brightened up long working days. Also, I thank Julia König, Rike Dannenberg and Monika Dulsinki for their amazing technical support and Stephen Horan for taking your time proofreading some parts of my thesis.